Analysis of blood oxygenation and cerebral blood volume responses in functional magnetic resonance imaging of an alert primate

Alexandre Hutton

Department of Biomedical Engineering
McGill University
Montreal, Canada
August 2015

A thesis submitted to McGill University in partial fulfillment of the requirements of the degree of Master of Biomedical Engineering

Table of Contents

Table of Figures

Table of Tables

1 Abstract

The blood-oxygen level-dependent (BOLD) signal in functional magnetic resonance imaging (fMRI) is an indirect measure of local neuronal activity. While the mechanisms underlying the positive BOLD response (PBR) are fairly well-understood, the mechanisms for the negative BOLD response (NBR) are not. Further, there have been inconsistencies between non-human primate (NHP) and human studies with regard to the sign of the cerebral blood volume response associated with NBR. There have also been inconsistencies between primate and human subjects in the magnitude of the NBR to different types of stimuli, namely flickering and rotating checkerboards. Specifically, rotating checkers stimuli, which have been commonly used and elicited NBRs in the visual cortex of primates, elicited only a diminished NBR in the human visual cortex.

The purpose of this study is to further investigate the mechanisms for the NBR, as well as to verify whether the NBR in alert macaques is consistent with either previously-reported results in anesthetized macaques or alert humans.

To investigate these inconsistencies, we established a protocol to acquire fMRI data from an alert and behaving NHP. We measured the BOLD response to four different stimuli, in order to establish areas of PBR and NBR. The stimuli consisted of flickering or rotating checkerboard rings which could be either small or large. We then compared the BOLD responses to cerebral blood volume (CBV)-sensitive responses, acquired in scans using ferumoxytol, an iron-based contrast agent. Acquiring these data allowed us to compare the relationship between the PBR, NBR, and CBV, as well as compare the responses to the different stimulus types.

Our results show that the experimental protocol was able to replicate the previously-reported relation between the PBR and CBV, where there is an increase in CBV associated with the PBR, and that this relation is consistent across all of our stimuli. We were able to demonstrate that the location of the NBR in the alert primate was predictable and consistent with previous studies in anesthetized primates and alert human studies. We go on to show that there is a decreased CBV response associated with the NBR for small stimuli, similarly to what has been reported in alert human subjects and contrary to the findings from anesthetized primates. The results on the relationship of the NBR and CBV responses for the large stimuli were inconclusive.

Lastly, we demonstrate a difference between the responses to flickering and rotating stimuli, and that the underlying difference is not due entirely to changes in CBV. Previous studies reported that NHPs had a NBR response associated with the rotating checkerboard that was more readily detectable than in humans. Here, we report that the magnitude of the NBR associated with the small rotating stimulus is greater than the NBR associated with the flickering stimulus, but that this is reversed for the large stimulus. Both were detectable, in contrast to previously-reported differences between anesthetized NHP and alert humans.

2 Abrégé

Le signal BOLD (blood-oxygen level-dependent) d'imagerie par résonance magnétique fonctionnelle (IRMf) est une mesure indirecte de l'activité neuronale. Les mécanismes qui génèrent la réponse BOLD positive (RBP) sont relativement bien compris, mais les mécanismes pour la réponse BOLD négative (RBN) ne le sont pas. De plus, il y a de l'incohérence entre les résultats des primates non-humain (PNH) et ceux des humains par rapport au volume sanguin cérébrale (VSC) et si celui-ci diminue ou augmente dans les régions de la RBN. Il y a aussi des incohérences avec l'ampleur de la RBN entre les PNH et les humains pour certain stimuli. Les stimuli rotatifs qui ont déjà été utilisée auparavant produisent une RBN très faible.

Le but de cet étude est d'enquêter les mécanismes pour la RBN, et de comparer si nos résultats sont cohérents avec les rapports pour l'humain conscient ou le PNH anethésié.

Pour vérifier les incohérences, nous avons établi un protocole pour acquérir des données d'IRMf avec un PNH alerte. Nous avons mesuré la réponse BOLD pour quatre stimulis différents afin d'établir des régions de RBP et RBN. Les stimulis sont de deux types, soit vacillant ou rotatif. Ils sont aussi de deux tailles, soit petite ou grande. Nous avons par après comparé la RBN et RBP avec les changements du VSC. Le VSC a été mesuré en utilisant le contraste magnétique ferumoxytol qui est à base de fer.

Nos résultats démontrent que notre protocole est en mesure de reproduire la connexion entre la RBP et le VSC, où il y a une augmentation de VSC associée avec les régions de RBP. Nous constatons aussi que la région de la RBN pouvait être reproduite et qu'elle allait dans le même sens que d'autres études. Nous avons détecté une baisse de VSC associée à la RBN pour les petits stimuli, mais nous ne pouvions pas déterminer la relation pour les grands stimuli car les régions la RBN et du VSC ne coïncidaient pas suffisamment.

Finalement, nous avons démontré une différence entre les réponses aux stimuli vacillants et rotatifs, et que la différence n'était pas causée entièrement par les changements de VSC. D'autres études ont rapporté que les PNH avaient une RBN causé par le stimulus rotatif qui était plus élevée qu'avec les humains. Nous démontrons que l'ampleur de la RBN associé avec le petit stimulus rotatif est plus élevée que pour le stimulus vacillant, mais que c'était inversé pour le grand stimulus. Il était possible de détecter les deux RBN, contrairement à la différence entre l'humain conscient et le PNH anesthésié.

3 Acknowledgements

The work done for this thesis required the establishment of a platform for performing alert monkey fMRI scans, which was first at McGill (and Canada, as far as we know). Consequently, there are a lot of people to thank for their assistance, both professionally and personally.

Firstly, the entire staff of the animal care facility at the MNI, who were invariably reliable. A special thanks to Dr. Jessica Hutta for always being patient with the non-emergencies that I was always panicking about, and Cathy Hunt for making herself available for my questions and concerns.

The MRI staff of the BIC were indispensable: David Costa, Ron Lopez, Louise Marcotte, and André Cormier. Not only did they help us set up our equipment and optimized our time in the scanner, but they always made the stressful atmosphere around the experiment much calmer and more pleasant.

Siemens researcher Dr. Raphael Paquin not only displayed a remarkable ability to adapt one of Siemens' WIP sequences during scans, but was patient with us throughout the entire process.

There were also previous lab members who built the platform and trained our monkey that deserve thanks. Dr. Martin Villeneuve, who trained the monkey, did the bulk of the initial experimental setup, and helped code some of the training protocol. Ze Shan Yao, who did some of the coding, showed me how it was currently designed, and trained me to handle the monkeys. Pascal Kropf, whose questions beginning with, "Something I don't understand is…" regularly revealed my own misunderstandings.

All this would not have possible without Dr. Amir Shmuel, who gave me a second chance at academia when most others wouldn't have. A special thanks for his work on and patience with reviewing this thesis.

Lastly, and most importantly, thank you to Majmun and Kofiko. I saw you more than my own family, and did all I could to make your time with me pleasant. The people closest to me asked about you regularly, if only because asking me about anything else would immediately result in news about you anyway. You'll never read this, but I'm happy that you'll continue to be in caring hands.

4 Contribution of Authors

There were four major contributors for this thesis: Alexandre Hutton, Ze Shan Yao, Martin Villeneuve, and Amir Shmuel.

Initiation and design of the study

Amir Shmuel initiated the study. Alexandre Hutton and Amir Shmuel designed the study.

Experimental Setup

The experimental setup was designed by Amir Shmuel. It was first created by Martin Villeneuve, and the procedure was adapted to the current study and formalized by Alexandre Hutton. Amir Shmuel adapted the design of the chair for the current study. Martin Villeneuve and Ze Shan Yao created custom modules for MonkeyLab, which were then adapted by Alexandre Hutton. Training of the non-human primate was done in succession by Martin Villeneuve, Ze Shan Yao, and Alexandre Hutton.

Data Acquisition

Alexandre Hutton set up the experiments, monitored animal behaviour, and acquired gaze position. The field of view and slice positioning was determined by Amir Shmuel. The MRI scanner was operated by MNI BIC's technicians.

Data Analysis

All analysis was performed by Alexandre Hutton, and methods and results were reviewed by Amir Shmuel.

Manuscript

This document was written by Alexandre Hutton and edited by Amir Shmuel.

5 Introduction

5.1 Acronyms

Acronym	Meaning		Acronym	Meaning
BOLD	Blood-oxygen level-dependent		NHP	Non-human primate
CAB	Contrast agent-based		NMR	Nuclear magnetic resonance
CBF	Cerebral blood flow		PBR	Positive BOLD response
CBV	Cerebral blood volume		PE	Phase encoding
$CMRO_2$	Cerebral metabolic rate of oxygen		pO_2	Partial pressure of O_2
fMRI	Functional MRI		T1WI	T_1-weighted image
GLM	General linear model		T2WI	T_2-weighted image
HbO, HbR	Oxy- and deoxyhemoglobin		TE	Echo time
HRF	Hemodynamic response function		TI	Inversion time
MRI	Magnetic resonance imaging		TR	Repetition time
MTT	Mean Transit Time		V1	Primary visual cortex
NBR	Negative BOLD response		SNR	Signal-to-noise ratio
CNR	Contrast-to-noise ratio		fCNR	functional CNR
LFP	Local field potential		MUA	Multi-unit activity
MION	Monocrystalline iron oxide nanoparticle		ASL	Arterial spin labelling

5.2 Definitions

Term	Definition
Gaze	Position at which the subject is looking.
Run	Single fMRI experiment. In this thesis, one run is the collection of 158 volumes.
Session	Collection of fMRI experiments. In this thesis, one session uses a single stimulus and consists of a variable number of runs.
SNR	Signal level relative to the noise level.

5.3 Motivation

MRI is a non-invasive imaging method capable of giving details about the structure of a person's brain without any long-term side-effects. FMRI allows us to detect areas of neuronal activation through hemodynamic coupling. The most commonly used signal is the blood-oxygen level-dependent (BOLD) response, which is modulated by three factors: $CMRO_2$, CBV, and CBF. The relationship between these three factors and the positive BOLD response is well-understood. Their relation to the lesser-known negative BOLD response, however, is much less studied. Previous studies report inconsistent results between humans and animal models [1, 2]. Specifically, while [1] reported increased CBV response in association with NBR in anesthetized primates, [2] observed decreased CBV response in alert human subjects under the same conditions. There have also been inconsistencies in the magnitude of the response to different types of stimuli, namely flickering and rotating checkerboards. Specifically, rotating checkers stimuli, which have been commonly used and elicited NBRs in the visual cortex of anesthetized primates, elicited only a diminished NBR in the human visual cortex. To explain these inconsistencies, [2] suggested three possible explanations: differences in posture (supine for human subjects, standing in a vertical bore for primates), state of alertness (anesthesia applied to primates), or species.

Animal models are extremely important for performing invasive measurements that are not possible to do in humans; a difference in the neurovascular coupling mechanisms would weaken the effectiveness of these models. As such, we believed that the contradiction warranted further investigation. Thus, the inconsistency with regard to the CBV response associated with NBR between alert humans [2] and anesthetized primates [1] motivates this study.

For this thesis, we intend to test whether the species difference was responsible for the increased CBV in primates instead of the expected decrease in NBR regions observed in human subjects. In addition, since anesthesia is known to affect the BOLD signal [3, 4], we use an alert NHP, which allows us to investigate the alternative hypothesis, namely that anesthesia effects caused the difference between the CBV responses associated with NBR in alert human subjects and anesthetized primates. We do this in two steps: first, we use an experimental paradigm that elicits a NBR in an alert macaque monkey, and second, we repeat the experiment after injecting a magnetic contrast that is sensitive to CBV.

Interestingly, [1] and [2] showed inconsistent magnitudes of NBR between alert human and

anesthetized primates in response to rotating checkers stimuli. In primates, rotating checkerboards elicited PBR of 2% and NBR of -1% relative to baseline. In alert human subjects, the number of voxels for the NBR rotating ring was smaller than the number of activated voxels with the flickering stimulus (81 for rotating vs. 960 for flickering). Whereas the PBR in response to both flickering and rotating checkerboard was similar to that obtained in primates in response to rotating checkerboard (~2%), the NBR was not. Flickering checkerboard stimuli elicited NBR (-1%); in contrast to the results in primates, rotating checkerboard elicited only a diminished NBR (-0.0006%). Thus, NBR was more readily detected with the rotating checkerboard in monkeys than in humans. This discrepancy motivates our second main aim. By using fMRI in an alert primate, we will test whether the reported inconsistency between the NBR in response to rotating checkers stimuli in humans and primates can be attributed to anesthesia.

5.4 Hypothesis

A previous study [2] reported decreases in CBV associated with the NBR in humans, contradicting their own results in anesthetized NHPs [1, 2]. Given the similarity between NHP and human brains, we hypothesize that this inconsistency is not due to the difference in species, but due to the difference in state of alertness (effects of anesthesia). We therefore hypothesize that if we used alert NHPs, we would detect a decrease in CBV associated with the NBR.

5.5 Objectives

We had a number of goals for this thesis:

1. Establish a platform for alert NHP fMRI, including protocols for measuring CBV via injectable MRI contrasts.
2. Test the reproducibility of the PBR and NBR in an alert NHP.
3. Investigate the neurovascular coupling between the PBR, NBR, and CBV responses.
4. Test whether the reported CBV discrepancy, namely decreases and increases in CBV associated with NBR in alert human subjects and anesthetized primates, respectively, were primarily due to anesthesia or a species difference.
5. Test whether rotating checkers stimuli elicit NBR in alert primates similarly to the response in anesthetized primates and contrary to findings in alert human subjects.

5.6 Background

This section provides the background necessary to understand the thesis. The methods used for this thesis are built on the principle of nuclear magnetic resonance (NMR), which is typically referred to as magnetic resonance imaging (MRI) in the context of medical imaging. Following the root cause of the NMR effect is begging to fall into the rabbit hole, so the explanation stops before classical physics becomes insufficient. . Most of the physics explanations and equations are either adapted, derived, or taken from Functional Magnetic Resonance Imaging [5], which in turn takes it from Magnetic Resonance Imaging: Physical Principles and Sequence Design [6]. After explaining the principles behind MRI, a summary is presented about the brain's structure and the biological sources for the functional signals.

5.6.1 **MRI Overview**

Magnetic resonance works by applying a strong magnetic field to the subject being imaged. The atomic nuclei reorient themselves so that their magnetic moment aligns itself either parallel or anti-parallel to the field. Once aligned, a measurable signal can be detected by applying a radiofrequency (RF) and shifting the magnetization so that it is perpendicular to the static field. After waiting a prescribed amount of time, the signal will give a measure of different magnetic properties. Depending on how the RF pulse is applied and on how long the measurement delay is, we can emphasize specific magnetic properties of tissues. Although MRI can be used to image different nuclei (such as phosphorus-13 [7], carbon-13 [8], and many others), most studies rely on hydrogen nuclei (protons) due to its abundance in the human body. We can get a 3D image by varying the magnetic field across space, and a 4D image by repeating the entire process multiple times.

5.6.2 **NMR**

Magnetic Moment, Angular Momentum, and the Gyromagnetic Ratio

The nucleus consists of two types of particles, protons and neutrons, each with their own spin. Atoms with an odd number of either protons or neutrons will have a net spin. Consequently, a spinning particle has angular momentum, and a spinning charge has a magnetic moment[1]. To move things into a more quantitative direction, we can throw in some equations and find that the angular momentum and magnetic moment are closely related.

1 If you are wondering how an uncharged neutron can give rise to a magnetic moment, it's currently thought that the moment is caused by the neutron's underlying quark structure. Refer to aforementioned rabbit hole.

The magnetic moment is the torque an object would experience when placed in a magnetic field **B**. If we choose a simplified model of the proton as a point charge moving in a circle of radius *r*, we'll have a system with a magnetic moment with magnitude $|\mu| = IA = I\,\pi r^2$, where I is the current and A is the area of the loop. The direction of the moment is given by the right hand rule applied to the charge's loop. The current is given by the amount of charge moving through an area per unit time. If we take our point charge to have a period T, the current moving through an area is $\frac{q}{T}$, where 'q' is the elementary charge. The magnitude of the magnetic moment is then $|\mu| = \frac{q}{T}\pi r^2$.

Similarly, the angular momentum of our point charge is given by $L = m\,\omega r^2$, where m is the mass, and ω is the angular velocity. The direction of the angular momentum is the same as the magnetic moment. Using the same description as above for the motion of the particle, we can expand the angular momentum to: $L = m\frac{2\pi}{T}r^2$.

The similarity between the angular momentum and magnetic moment becomes apparent, and can be simplified to: $\boldsymbol{\mu} = \gamma \boldsymbol{L}$, with $\gamma = \frac{q}{2m}$.

γ is the gyromagnetic ratio. The relation between these two quantities is crucial to magnetic resonance because it governs precession, which in turn governs how we excite our system and get a useful signal.

Moments and the B_0 Field

The properties discussed in the previous section are not immediately useful for looking at neuroanatomy. Let's start by adding a magnetic field to our proton to see what happens.

The external field will cause magnetic moments to align themselves with the field. The torque generated on our proton is given by: $\boldsymbol{\tau = \mu\, x\, B.}$

To get an intuitive understanding of the torque's effect, we can simply look at properties of the cross-product. First, there will be no torque if the magnetic moment is either parallel or antiparallel. Second, the torque is always perpendicular to both the magnetic field and the moment. In other words, the torque will cause the proton to spin around the magnetic field direction.

Mathematically, we can see this by using our understanding of torque and the equivalency between the magnetic moment and angular momentum. Torque is the rotational equivalent to a force, similar to angular momentum and momentum. Force is the first derivative of momentum

(with respect to time), and torque is the first derivative of angular momentum:

$\boldsymbol{\tau} = \frac{dL}{dt}$.

Combining the previous equations, we obtain:

$$\frac{d\boldsymbol{\mu}}{dt} = \gamma(\boldsymbol{\mu} x B) \qquad \text{Equation 1}$$

With no loss of generality, we'll assume that our B-field is in the z direction, and that we have arbitrary initial conditions:

$$\boldsymbol{\mu}(t) = \mu_{x0}\vec{\boldsymbol{x}} + \mu_{y0}\vec{\boldsymbol{y}} + \mu_{z0}\vec{\boldsymbol{z}} \qquad \text{Equation 2}$$

With these assumptions from equation 3, we can divide equation 2 into a set of three easily-solved differential equations:

$\frac{d\mu_x}{dt} = \gamma\mu_y B_0$	$\frac{d\mu_y}{dt} = \gamma\mu_x B_0$	$\frac{d\mu_z}{dt} = 0$

Solving for μ_y and substituting, we get:

$$\mu_y = \frac{1}{\gamma B_0}\frac{d\mu_x}{dt}$$

$$\frac{d\mu_y}{dt} = \frac{1}{\gamma B_0}\frac{d^2\mu_x}{dt} = -\gamma B_0 \mu_y$$

$$\frac{d^2\mu_x}{dt} = -\gamma^2 B_0^2 \mu_x$$

Recognizing the form of differential equation in the last line, we know the solution will take the form of:

$\mu_x = a\cos(\gamma B_0 t) + b\sin(\gamma B_0 t)$	$\mu_y = a\sin(\gamma B_0 t) + b\cos(\gamma B_0 t)$

Where "a" and "b" are arbitrary coefficients.

By applying the initial conditions, we obtain the full solution of:

$\mu_x = \mu_{x0}\cos(\gamma B_0 t) + \mu_{y0}\sin(\gamma B_0 t)$	$\mu_y = \mu_{x0}\sin(\gamma B_0 t) + \mu_{y0}\cos(\gamma B_0 t)$

With some algebra, we can see that this path traces a circle of radius $= \sqrt{\mu_{x0}^2 + \mu_{y0}^2}$.

The result is this: given some initial transverse magnetization and an external B-field, protons

will precess around the B-field direction at a frequency γB_0, known as the Larmor frequency. This frequency will be important for getting a signal from our protons.

Multiple Protons and the B_0 field

Investigating the effects of a magnetic field on single protons is an important exercise, but MRI doesn't look at single protons. Rather, it considers the magnetization of an entire volume of hydrogen atoms, where the magnetization is the vector sum of all magnetization moments within a group. It is important to consider the interaction between multiple neurons.

One of the important concepts that was previously alluded to was the stability of the magnetic moment; there are only two directions where the proton will not be subject to torques - parallel and antiparallel to the B-field. At first glance, this might hint that we should see no net magnetization since the moments of multiple protons would cancel each other out. Luckily, there is a small energy difference between parallel and antiparallel states, which causes more moments to be in the parallel state. The energy difference is rather miniscule:

$$\Delta E = 2\mu B_0$$

$$\Delta E = \frac{h}{2\pi}\gamma B_0 \approx 2.8 * 10^{-26} B_0$$

If using a 3T B-field, this corresponds to the energy of a single photon at 127.7MHz, which is very little. This lends itself very well to a Boltzmann distribution, with the difference between the number of atoms with parallel and anti-parallel orientations given by:

$$P_p - P_a = \frac{\Delta E}{2k_b T}$$

The difference gives rise to a net magnetization, given by:

$$\vec{M} = \frac{\Delta E}{2k_b T} n\, \mu_z\, \vec{z}$$

The same math that was applied to the single-proton case of magnetic moments and precession can be applied here, and gives us the same circularly-rotating net field as with the moments. Whereas a single proton has a constant magnetization, the net magnetization is not constant due to the interaction between multiple protons. The reason for this is discussed in the following sections.

Exciting Systems

Now that we have a net magnetization, we need to find a way of manipulating it to give us a meaningful signal. Based on the discussion thus far, it would be fair to say that MRI shouldn't

work: if a proton starts with a magnetic moment with a component in the x-y plane, it will precess indefinitely since there is there is no torque that reorients the moment back in the z-direction. Luckily, thermal energy reorients the moments such that all particles eventually return to the lowest available energy states: parallel and anti-parallel moments. Since there is a slight preference for alignment along the parallel direction, the magnetization will be parallel to the large B_0 field.

Despite being able to direct the net magnetization, we won't be able to extract any information from a constant magnetization - we need a varying signal to detect. As was shown in detail in the previous sections, we know that we can get a varying signal if we can tip the magnetization away from the longitudinal axis and into the transverse plane. To do that, we need to re-use some of the effects we've seen this far:

- Applying an external B-field produces a torque perpendicular to both the magnetic moment and the B-field.
- A constant B-field makes the protons precess around a single direction.
- The protons will precess with frequency γB_0 around the longitudinal direction once their magnetic moments are tipped away.

Our goal is to move the longitudinal magnetization into the transverse plane so that we can get a signal from the precessing protons. If we tried to apply a constant B-field in one of the transverse directions to do that, the protons would precess around a second axis, which would make signal measurements much more difficult. Instead, we can apply a B-field in such a way that the torque is always redirecting the magnetization towards the anti-parallel direction. The only way to do that is to ensure that the B-field is always perpendicular to the magnetic moment, and the only way to do that it is to have a rotating B-field that matches the precessing protons. This is where the Larmor frequency comes in: if we apply a B-field that rotates within the transverse plane, we can apply a torque that will rotate the moment towards the anti-parallel direction. If we time our excitation properly, we can excite our system until the magnetization reaches the transverse plane, and then stop. The result is that our net magnetization will be entirely in the transverse plane, and we will get the largest signal possible. With some clever manipulations of the magnetization, we can get some extra information out of our volumes.

Relaxation Mechanisms

When given no excitation energy, our volume will return to its steady-state magnetization along

the longitudinal direction with no transverse component. It does this in two ways: longitudinal and transverse relaxation.

Longitudinal Relaxation

Longitudinal relaxation refers to the longitudinal magnetization returning to its steady state. This occurs when the protons either release or absorb energy from their surroundings to return to their parallel or anti-parallel orientations, respectively. The longitudinal magnetization recovers asymptotically, given by the exponential:

$$M_z = M_0\left(1 - e^{-\frac{t}{T_1}}\right)$$

T_1 is a coefficient that is characteristic to a type of tissue[2] (i.e., different tissue types will have different values for T_1).

Transverse Relaxation

Transverse relaxation refers to the reduction of the transverse component of the relaxation back to zero. The important thing to realize about transverse relaxation is that although the magnetic moments of each proton has a constant magnitude, their magnitude of their sum will vary as the protons' magnetic moments begin to point in different directions. Any loss of coherence in the phase of the moments will cause a drop in the net magnetization. This is the principle cause of transverse relaxation. There are two causes for the gradual phase incoherence: proton-proton interaction and local field inhomogeneities.

Interactions between protons (aka spin-spin) result is an irregular dephasing of protons caused by the B-fields generated by nearby protons. Since the process is not regular (i.e., can't be described), it cannot be reversed. If the magnetization is tipped entirely into the transverse plane, the transverse magnetization decays exponentially, described by:

$$M_{xy} = M_0 e^{-\frac{t}{T_2}}$$

T_2 is another coefficient that is characteristic to a type of tissue.

The second cause of dephasing, B-field inhomogeneities, results in small differences between the expected and actual Larmor frequency. As a result, the slower/faster protons will have a phase which changes differently from their neighbours. Unless field inhomogeneities are specifically addressed[3], the transverse component will decay with a time constant T_2^* instead of T_2. T_2^* is

2 More generally, it is characteristic to a molecular environment, but our interest is in brain tissue.

3 The effect of field inhomogeneities can be corrected by using a spin-echo sequence.

necessarily shorter than T_2.

Bloch Equation

By combining the previous two equations for the longitudinal and transverse magnetizations with the equation for a precessing magnetization, we get the equation governing MR signal generation, the Bloch equation:

$$\frac{d\vec{M}}{dt} = \gamma\vec{M}\ x\ \vec{B} + \frac{1}{T_1}(M_0 - M_z) - \frac{1}{T_2}(M_x + M_y)$$

The Bloch equation describes the rate at which the magnetization varies with time. We can compare the components in each of the x-y-z directions to check that the relaxation mechanisms are consistent: looking at the M_z component, $(M_0 - M_z)$, we see that there is a positive rate of change until $M_0 = M_z$.

Spatial Encoding

Our goal thus far has been to find a way of generating 3D images of the brain. We've established a system of generating signals that depend on tissue type, but not how to deal with a volume with multiple tissue types. Without addressing this, we would get a single voxel instead of the several thousand we'd like to get. To image an entire volume with some kind of tissue discrimination, we use gradients in the B-field to encode spatial information in the signal we'll measure.

Gradients

When we looked at both the magnetic moment and the net magnetization, we saw that they precessed at a rate given by the Larmor frequency, $\omega = \gamma B_0$. If we had a field whose strength varied in space instead of a uniform B_0 field, we could get the Larmor frequency to encode the location of the protons. That is, suppose that:

$$\omega = \omega(x, y, z) = \gamma B(x, y, z)$$

This setup seems like it would let us image an entire volume in a single shot, but it isn't practically realizable to have a unique B-field strength at every point. Instead, we can establish field gradients that vary linearly with position. Gradients bring a new issue: applying two gradients in the same space creates a single gradient with a different slope. Naively applying gradients won't give us the spatial encoding we need. *However,* we can be clever about applying the gradients: instead of applying them at the same time, we can apply them in succession. We have three directions to code for, and are divided into slice selection, phase encoding, and frequency encoding.

When we measure our signal, it is not inherently location-sensitive, and it will include the magnetization from our entire volume. The signal is given by an integral over space which incorporates the initial magnetization, T_2 relaxation, and phase changes in time:

$$S(t) = \int_x \int_y \int_z M_{xy0}(x,y,z) e^{-\frac{t}{T_2}} e^{-i\omega_0 t} e^{-i\gamma \int_0^t G_x(\tau)\vec{x} + G_y(\tau)\vec{y} + G_z(\tau)\vec{z}\, d\tau} dx\, dy\, dz$$

Variable	**Definition**
S(t)	Measured signal
M_{xy0}	Initial magnetization in x-y plane
T_2	T_2 relaxation constant
ω_0	Larmor frequency at B_0
γ	Gyromagnetic ratio
G_x, G_y, G_z	Gradient strengths in x, y, z directions.

Since our immediate interest lies only in the spatial information we can extract from the signal, we can remove the T_2 relaxation ($e^{-\frac{t}{T_2}}$) and the phase change due to the B_0 field ($e^{-i\omega_0 t}$) and simplify the equation to:

$$S(t) = \int_x \int_y \int_z M_{xy0}(x,y,z) e^{-i\gamma \int_0^t G_x(\tau)\vec{x} + G_y(\tau)\vec{y} + G_z(\tau)\vec{z}\, d\tau} dx\, dy\, dz$$

This equation further simplifies as we include the effects of our gradients.

Slice Selection (z)

The slice selection gradient is the simplest gradient. To follow convention, we'll use the z-direction (longitudinal) for slice selection. For this encoding, we want to get a signal from a specific range of z-coordinates ("slice"). Let's first apply our gradient, such that $B = B_0 + G_z z$, where G_z is the strength of the z-gradient.

We know that in order to tip the magnetization into the transverse plane, we need to excite the protons with a magnetic field rotating at their Larmor frequency. Once the magnetization is tipped into the transverse plane, it will keep precessing at a rate given by the B-field. This is the important part of slice selection: by changing the excitation frequency, we selectively tip the magnetization of different slices. If we then remove the z-gradient, the entire volume's Larmor

frequency will return to $\omega = \gamma B_0$, *but only protons in the selected slice will have a net magnetization in the transverse plane*. As such, we won't get any signal from the rest of the volume.

To see the effect of the gradient on our signal equation, we'll define some arbitrary limits. The excitation pulse is ideal (rectangular) and selects a slice defined by z-limits of $z_c \pm \frac{\Delta z}{2}$. There is no transverse magnetization outside of this slice. With these assumptions, we see that:

$$G_x = G_y = 0$$

$$M_{xy0}(x,y,z) = \begin{bmatrix} 0 & z < z_c - \frac{\Delta z}{2}, z > z_c + \frac{\Delta z}{2} \\ M_{xy}(x,y) & otherwise \end{bmatrix}$$

and:

$$S(t) = \int_x \int_y M_{xy}(x,y) e^{-i\gamma \int_0^t G_x(\tau)x + G_y(\tau)y \; d\tau} dx \, dy$$

The signal is then a function of the transverse magnetization and the accumulated phase at position (x,y).

Phase & Frequency Encoding (y-x)

Our protons convey information through a changing magnetization, which has three properties: magnitude, frequency, and phase. The magnitude is already carrying PD/T_1/T_2 information, so we can't use that. We can control the last two to encode our remaining spatial components.

Phase encoding is conceptually simple, but the math does not lend itself to an intuitive understanding. Imagine two protons whose moments have been put in the transverse plane. Initially, their moments are in phase and they are rotating at the same frequency. If we apply a gradient such that proton A experiences a small B-field increase and proton B experiences a decrease, they will begin to precess at different frequencies. We wait for a short time, then remove the gradient. Our protons will now precess at their initial frequencies, but (with proper timing) will have different phases. If we apply the same procedure to an entire volume, our y-position will be encoded in the phase of our magnetizations.

Frequency encoding is both conceptually and mathematically simple. Immediately before data acquisition, we turn on a gradient in the x-direction. As before, our protons will have precessing frequencies that vary in the x-direction. The idea is that once the signal is acquired, we can separate voxels in the x-direction by taking the Fourier transform, applying filters, and extracting

the magnetization from the filtered signal.

Mathematically, it is much more convenient to look at the effects of the x-y gradients on the signal equation, in an abstraction called k-space.

5.6.3 K-Space

K-space4 allows us to abstract away some of the difficulties in signal acquisition and instead deal with sampling the k-space of an image. First, let's define what we mean by k-space:

$$S(t) = \int_x \int_y M_{xy}(x,y) e^{-i\gamma \int_0^t G_x(\tau)x + G_y(\tau)y \, dt} dx \, dy$$

$$S(t) = \int_x \int_y M_{xy}(x,y) e^{-i\gamma \int_0^t G_x(\tau)x \, d\tau} e^{-i\gamma \int_0^t G_y(\tau)y \, d\tau} dx \, dy$$

We then make a simple substitution:

$$k_x = \frac{\gamma}{2\pi} \int_0^t G_x(\tau) d\tau$$

$$k_y = \frac{\gamma}{2\pi} \int_0^t G_y(\tau) d\tau$$

$$S(t) = \int_x \int_y M_{xy} e^{-i2\pi k_x(t)x} e^{-i2\pi k_y(t)y} dx \, dy$$

This form bears a striking resemblance to the Fourier transform:

$$F(2\pi f) = \int_{-\infty}^{\infty} f(t) e^{-2\pi f t} dt$$

.

Instead of representing temporal frequencies, our signal measures 2D spatial frequencies k_x and k_y. In order to extract M_{xy}, we need to build a 2D map of our k-space:

$$S(k_x, k_y) = \int_x \int_y M_{xy} e^{-i2\pi k_x x} e^{-i2\pi k_y y} dx \, dy$$

.

By controlling our gradients' magnitudes and duration, we can control which part of the k-space we sample. Once we have an appropriately-sampled k-space, we can take the 2D inverse Fourier transform to extract our magnetization which has been spatially localized.

$$M_{xy} = \int_{k_x} \int_{k_y} S(k_x, k_y) e^{i2\pi x k_x} e^{i2\pi y k_y} dk_x dk_y$$

.

4 Note that these signals are digitally sampled, so the discrete Fourier transform should be used. Converting from a continuous-time, continuous-value signal to a discrete-time, discrete-value signal presents its own difficulties and requirements, but the details of digital signal processing are not immediately relevant.

5.6.4 **Image Weighting**

There are several magnetic properties of tissues that are commonly measured, namely the proton density (PD), the longitudinal relaxation time constant (T_1), and the transverse relaxation time constant (T_2), and a combination of T_2 and field inhomogeneity (T_2^*).

Proton Density

The net magnetization is proportional to the number of protons in an area. An area with lots of protons will have a stronger net magnetization than an area with very few protons. By simply moving the net magnetization into the transverse plane and measuring the signal, we can get an idea of the relative proton densities in a volume. PD is probably the conceptually-simplest weighting to obtain, but does not give the best anatomical contrast.

T_1-Weighted

Different tissues will have different relaxation coefficients; if we can design a sequence of excitation pulses so that the signal is heavily dependent on T_1, we can get an image that will show us where tissues with different T_1 values are located. The simplest way to do this is to apply a 90° excitation pulse, allow some time for T_1 recovery, apply another 90° pulse and measure the result.

This is what happens within each step:

Step	**Effect**
Initial	Net magnetization is in longitudinal direction.
90° excitation pulse	Puts net magnetization into transverse plane.
Wait	Longitudinal relaxation occurs, with longitudinal magnetization recovering depending on T_1.
90° excitation pulse	Puts net magnetization into transverse plane.
Measure signal	If the second pulse is applied before the longitudinal magnetization can fully recover, different tissue types will have different magnitudes for the longitudinal components, weighted by their respective values for T_1.

The goal of a T_1 image is to get a contrast between tissue types. A similar approach to getting a T1WI is to use a 180° pulse before the 90° pulse, which places the net magnetization in the anti-parallel direction. The T_1 recovery is the same as before, but the magnetization has extra time for the tissues to differentiate themselves. The result is greater contrast at the cost of a small signal loss. This type of sequence is known as inversion recovery, and it was used for this thesis to get

T_1w structural images.

T_1 weighting is particularly useful for delineating grey and white matter. Fluids are markedly absent in T_1 images, as seen in the CSF of the ventricles.

T_2- and T_2-Weighted Images*

We know that tissues have different values for T_1, T_2, and T_2^*. Tissues with long T_1 values don't necessarily have long T_2^* values, meaning that we can use T_2^* to put emphasis on tissue types different from the T1WI. T_2^*-weighting depends on both spin-spin interactions and field inhomogeneity. The pulse sequence is simple: from the longitudinal magnetization, we apply a 90^o pulse to tip it into the transverse plane, wait for dephasing to occur, then measure the signal. In order to minimize T_1 effects, it is important to allow the longitudinal vector to recover between 90^o pulses. T_2-weighted images are obtained in a similar manner, but the dephasing needs to be reversed to remove the effects of field inhomogeneities. This is done by applying a 180^o pulse and waiting for the moments to rephrase (duration is equal to the time between the 90^o and 180^o pulses).

T_2^* weighting is useful for detecting changes in blood oxygenation, and is typically used in BOLD [9] imaging.

5.6.5 **MRI & Functional MRI**

MRI allows us to obtain a static image of a brain. Although already immensely useful, we're interested in detecting neuronal activity. For that, we'll need to obtain multiple sequential volumes, as well as have some idea of how neuronal activity affects an MRI signal. The next few sections will cover the latter.

Neuronal Activity

Activity in the brain occurs through the activity of neurons. For the purposes of this explanation, we'll describe neurons using a simplistic model. A single neuron consists of three sections: dendrites, soma, and axon. Dendrites serve as input, taking the activity of connected neurons and sending excitatory and inhibitory post-synaptic potentials to the cell body. The soma integrates all these potentials from the dendrites, and if the sum is large enough, a large electrical pulse ("action potential") is sent along the neuron's axon to be relayed to other neurons.

The brain is divided into functional areas, where neurons in an area form networks to perform similar actions; the motor cortex helps to process motor actions, the thalamus relays sensory

information, the visual cortex processes visual information. By selecting our method of stimulation, we can trigger different sections of the brain.

Electrically-active neurons need to replenish their energy stores by taking in glucose and oxygen from the extracellular space [10]. The same is true on a larger scale: when an area becomes active, the brain needs a method to quickly replenish glucose and oxygen present in that area. Since blood is the carrier of both these resources, the brain needs a method of increasing blood delivery to areas that are active. The blood response is known as the hemodynamic response, and the connection between neuronal activity and the hemodynamic response is called neurovascular coupling.

Hemodynamic Response

Blood vessels must react to increases in neurophysiological activity and change the local blood flow to reflect changes in energy demand. This adaptation is termed the hemodynamic response. In the brain, metabolism can be assessed by a few indicators, such as glucose uptake or O_2 consumption. The latter is termed the cerebral metabolic rate of oxygen ($CMRO_2$).

Early studies by Raichle et al. showed that there was a direct correlation between CBF and $CMRO_2$ in brains at rest [11]. Calculating the $CMRO_2$ requires the product of three variables: oxygen extraction fraction (OEF), CBF, and arterial oxygenation. Raichle et al. were able to measure both CBF and $CMRO_2$ by consecutively injecting radioactive oxygen (^{15}O) in two forms: one in oxyhemoglobin, the other in water. By measuring the amount of ^{15}O deposited in tissue (extrapolated from a decay curve) compared to the injected amount (initial peak), they were able to get a measure of oxygen extraction. The second injection of $H_2{}^{15}O$ gave them a direct measure of blood flow. With a third measurement of arterial oxygenation, both CBF and $CMRO_2$ were measured in different regions of the brain. They found a direct correlation between the two, which showed that brain regions with high resting metabolism receive more blood.

Almost a decade later, a revolutionary article by Fox and Raichle [12] provided evidence of decoupling between CBF and $CMRO_2$. Their experiment involved three different methods of introducing ^{15}O to measure CBF, CBV, and OEF. CBF and OEF were measured as in [11], but OEF was measured using inhaled ^{15}O-labeled oxygen instead of injected hemoglobin. CBV was measured using a method similar to the one described in [13], but used ^{15}O instead of ^{11}C. ^{15}O-labeled carbon monoxide was inhaled by the subject. By comparing the counts per second in cerebral tissue and the peripheral vessels, they were able to get a measure for CBV using the

following equation (from [13]): $CBV = \frac{C_{br}}{C_{bl} f P_{bl} P_t} * 100$, where "$C_{br}$ is the concentration of ^{11}C-labeled carbon monoxide in the brain, C_{bl} is the concentration of ^{11}C-labeled carbon monoxide in the blood, f is the ratio of the mean cerebral small vessel hematocrit to large vessel hematocrit, P_{bl} is the density of blood, and P_t is the density of brain tissue.".

One set of measurements was done while the subjects were resting, the other while their finger pads were electrically stimulated. The results showed that compared to rest, the stimulated condition showed differences in the contralateral somatosensory cortex: a large increase in CBF, no significant increase in $CMRO_2$, and small increase in CBV. The results showed a decoupling between CBF and $CMRO_2$. The amplitude and speed of the increase in CBF suggest that the response is not modulated by the build-up of metabolites. Further, the partial pressure of O_2 (PO_2) and pH did not precede the rise in CBF, indicating that changes in these two factors are not the driving force of the increased CBF. Later studies found that the CBF response is not affected by either hypoglycemia or hypoxia [14], indicating that the hemodynamic response is not triggered by a feedback mechanism.

CBV was not directly examined until well after the measurements of CBF and $CMRO_2$. Rosen et al. [15, 16] explored CBV using a gadolinium-based contrast agent, Gd-DPTA. This contrast agent doesn't cross the blood-brain barrier, which made it ideal for measuring the volume in blood vessels only. In their second paper, the authors measured CBV-weighted images while the subjects viewed either darkness or flashing LEDs. The same group, Belliveau et al. [17], published the first fMRI data using Gd-DPTA and a visual stimulus paradigm, and found that CBV increased by 32 ± 10% (±SD).

As discussed in a recent opinion article [18], there are four likely scenarios for the decoupling of CBF and CBV:

1) O_2 can only increase with a large increase in CBF.
2) The partial pressure of O_2 decreases quickly with distance from the nearest blood vessel. Large CBF response may be necessary to support cells further away from blood vessels.
3) The large CBF response might be a safety mechanism in case oxygen delivery is affected (e.g. brief interruption).
4) The CBF response may be necessary for something other than oxygen delivery.

A model was proposed for the first scenario [19]. Given that an increase in CBF means a

decrease in mean transit time (MTT)[5], and that a decrease in MTT means a decrease in the OEF, the model states that the increased CBF with decreased OEF is necessary to compensate for a small increase in $CMRO_2$.

The second and third scenarios appear to be the most likely, especially when considered together. A two-photon microscopy measurement of tissue oxygenation [20] showed a gradient of pO_2 which decreased to low levels further away from blood vessels. Later, it was shown that the pO_2 of these distant locations remained constant during activation, while there was an increase at locations closer to the blood vessel [21]. The authors' conclusion was that the CBF overcompensation seen in blood vessels is necessary to maintain a constant pO_2 even in locations distant from blood vessels. It would be sufficient for the pO_2 to simply return to baseline shortly after an increased $CMRO_2$, but it would also be somewhat risky; any interruption in O_2 supply would cause the distant neurons to become hypoxic.

The last scenario, where CBF serves for something other than O_2 delivery, is unlikely. Two substances are consumed to produce energy for neuronal activity; glucose and oxygen. Glucose concentration in cortical tissue at rest is about 2mM [22], compared to a metabolic rate of about 28.5 nmol/mL/s [23]. By comparison, resting O_2 concentrations in cortical tissue is approximately 30nmol/mL [18, 24] and a metabolic rate of around 30nmol/mL/s [23, 25]. An interruption in the supply of glucose would thus be less disastrous than the interruption of O_2 supply. Further, the CBF response's primary role is unlikely to be carrying away metabolites, as the early experiments of Fox and Raichle [12] showed that the CBF response occurred before any change in deoxyhemoglobin was detectable.

Neurovascular Unit

The details of the mechanism behind neurovascular coupling are not fully known, but experimental results exclude certain possibilities. The early experiments of Fox and Raichle [12] exclude the possibility that metabolites are solely responsible for the CBF response, for example. Although not all the details are known, there is evidence for the involvement of particular cells, together termed the "neurovascular unit," which together are responsible for the hemodynamic response. The neurovascular unit includes numerous components: neurons, the extracellular matrix, astrocytes, pericytes, and the endothelium [26]. Depending on the literary source and size

[5] Given that MTT = CBV/CBF [104], this is necessarily true. Briefly, MTT is a measure of how quickly blood passes through vessels.

of the vessel being considered, the definition can be expanded to include microglia and smooth muscle cells [27]. A comprehensive review of neurovascular coupling, the neurovascular unit, and its components can be found in [28].

Neurons

The neurovascular unit's purpose is, in the most general terms, to control the blood supply to better meet the needs of nearby cells. As previously discussed, the metabolic needs of the brain is dictated by the needs of neurons, particularly for oxygen. There is evidence for types of neurons interacting directly with the endothelium and astrocytes:

Type	Vasodilation/vasoconstriction	Source
Noradrenergic	Mostly vasoconstriction	[29, 30]
Serotonergic	Mixed	[31] [32]
Cholinergic	Vasodilation[6]	[33, 34]
GABA-ergic	Mixed [35]	[36]

Not surprisingly, neurons play a critical role in maintaining their own energy supply. Neurons directly connecting to the endothelium is only one of several pathways for controlling blood flow.

Astrocytes

Astrocytes are another component of the neurovascular unit. Astrocytes appear to play some role in developing the blood-brain barrier (BBB) [37] (though they may not [38, 39]), but our interest is mainly the astrocytes' role in functional hypo/hyperemia. Due to their end-feet completely surrounding the endothelial cells, it was initially believed that the astrocytes themselves formed the BBB. It was demonstrated that horseradish peroxidase could pass between the gaps of the end-feet [40], leaving the endothelial cells to form the BBB. Astrocytes serve as one of the paths between neuronal activity and nearby blood vessels (the other being diffusion). Zonta et al. [41] demonstrated the importance of the astrocytes' glutamate-mediated [Ca^{2+}] responses by selectively triggering or inhibiting these responses and measuring the amount of dilation in the connected arterioles. Triggering the response caused a reproducible increase in vessel diameter

[6] For *cerebral* arteries, due to M_5 muscarinic receptors. Vasoconstriction elsewhere.

while inhibiting the response reduced the amount of activity-dependent dilation.

Pericytes & Smooth Muscle Cells

Pericytes (PCs) are located outside the endothelial tissue but within the sheath of astrocytic endfeet [26]. The functional role of pericytes is not fully understood. In large vessels such as arterioles, vasoconstriction and vasodilation is achieved in part by contraction and relaxation of smooth muscle cells. These are not present in capillaries, which are the most immediate supply of energy for neurons. In 2001, PCs were found to contain constricting proteins [42]. There is evidence of pericyte constriction causing vasoconstriction in the retinal capillaries of rats when acetylcholine levels are controlled [43], which indirectly triggers the contractile proteins. A recent study [44] showed that pericytes can be caused to dilate by neuronal activity, and that they are responsible for about 84% of the increase in blood flow.

Endothelial Cells

The endothelial cells (ECs) form the blood vessels. ECs in the cortex differ slightly from the rest of the body [45]. Besides being surrounded by astrocytes, cortical ECs show a heavily reduced permeability to most molecules due to their lack of fenestrations and presence of tight junctions (TJs) between adjacent ECs [46]. Small molecules such as water or gases like O_2 or CO_2 diffuse freely across the endothelium, while larger molecules such as glucose require specialized transport proteins to enter the brain. Lipid-soluble molecules (e.g., ethanol) will also diffuse across the EC.

The ECs' role in functional hyperemia shouldn't be understated. Neuron-to-astrocyte signalling is important for dilating nearby blood vessels, and the PCs and SMCs are at least partially responsible for the mechanical constriction and relaxation, but these changes occur locally. Decreasing the local flow resistance will not sufficiently increase the blood flow since the upstream resistance of larger vessels is significantly larger [47]. Two mechanisms for upstream communication have been proposed; intramural vascular signalling and flow-mediated vasodilation. Intramural signalling involves upstream communication through the gap junctions of ECs and SMCs. One study tested several molecules and found them to cause upstream vasodilation in rat cerebral arterioles [48]. A number of vasoactive molecules have been identified (see table 1, [28]), but their details are not immediately relevant for this study. For flow-mediated vasodilation, the proposed mechanism is that the small local increase causes an

increase in shear stress of upstream vessels [28], which in turn causes them to dilate. One issue that remains unclear in both cases is how non-activated vessels fed by the same upstream vessel increase their resistance to keep their local CBF constant.

5.6.6 **Visual System**

Anatomy

Visual information is relayed a few times before being presented to the brain for processing. Light enters the eye and strikes photoreceptors[7] located in the retina, which in turn cause ganglion cells to relay the information to the lateral geniculate nucleus (LGN). The LGN is a thalamic nucleus which relays visual information directly to the primary visual cortex (V1), located in the posterior area of the brain.

Visual Cortex

The visual cortex is divided into multiple sections, each with their own purposes. There are three areas of the visual cortex which are important for this study: the primary, secondary, and tertiary visual cortices.

The primary visual cortex, V1, is the first to process visual information, and responds to simple features within stimuli, such as edges (contrast), spatial & temporal frequencies, and orientation [49]. V1 relays information to V2, V3, and back to the LGN for feedback [50]. The secondary visual cortex, V2, is located anterior to V1. It represents different quadrants of the visual field, and responds primarily to orientation, spatial frequency, color, stereopsis and visual motion. The tertiary visual complex, V3, responds to motion. The exact purpose of V3 is debated, but it is worth mentioning since the motion in our stimuli is likely to activate it.

5.6.7 **Positive BOLD Response**

The neurovascular unit's purpose is to control blood flow based on neural activity. These microscopic changes are visible through MRI sequences which are affected by blood parameters. As early as 1936, Pauling and Coryell [51] explored the structure of oxyhemoglobin, deoxyhemoglobin, and carbonmonoxyhemoglobin. They found that oxyhemoglobin was paramagnetic, while deoxyhemoglobin was diamagnetic. Ogawa et al. [52] used this property in

[7] Rods and cones

1990 to demonstrate a T_2^* contrast based on blood oxygenation in rats. Two years later, the first functional blood-oxygenation level-dependent (BOLD) contrast was reported independently by Kwong et al., Ogawa et al., and Bandettini et al. [53, 54, 55]. All three groups produced timecourses which showed a significant change in signal during periods of stimulus, and they were able to localize the activation to specific areas of the brain. Kwong and Ogawa presented activation following a subject's exposure to light, and showed that the activation was well-localized in the visual cortex. Bandettini presented the activation in response to a finger-tapping test, and it was localized to the sensorimotor cortex.

These results showed that the BOLD signal was consistent with previous PET studies (such as [11, 12]) without the need for the injection of radioactive material. When combined with our knowledge of neurovascular coupling, the BOLD signal gives us an indirect measure of local neuronal activity.

The BOLD signal is governed by three parameters: $CMRO_2$, CBV, and CBF:

$$BOLD\ \alpha \frac{CBF}{CBV\ x\ CMRO_2} \qquad \textit{Equation 3}$$

The effect of each parameter is to change the amount of deoxyhemoglobin in a given volume. An increase in CBV means a voxel will have a higher proportion of blood to tissue, which means the signal will be more attenuated. Since deoxyhemoglobin is paramagnetic, the tissue-blood proportion is most significant to the BOLD signal when $CMRO_2$ is elevated and can produce enough deoxyhemoglobin to fill the extra volume. The combination of an increased CBV and $CMRO_2$ increases the total deoxyhemoglobin and decreases the BOLD signal. A higher CBF means deoxygenated blood will be replaced more quickly by freshly-oxygenated blood, which increases the BOLD signal. Incidentally, this is only possible because the rate at which oxygen is extracted from hemoglobin decreases as the CBF increases.

The MRI signal observed after neuronal activation has a few stages, and the timecourse is described in the following figure.

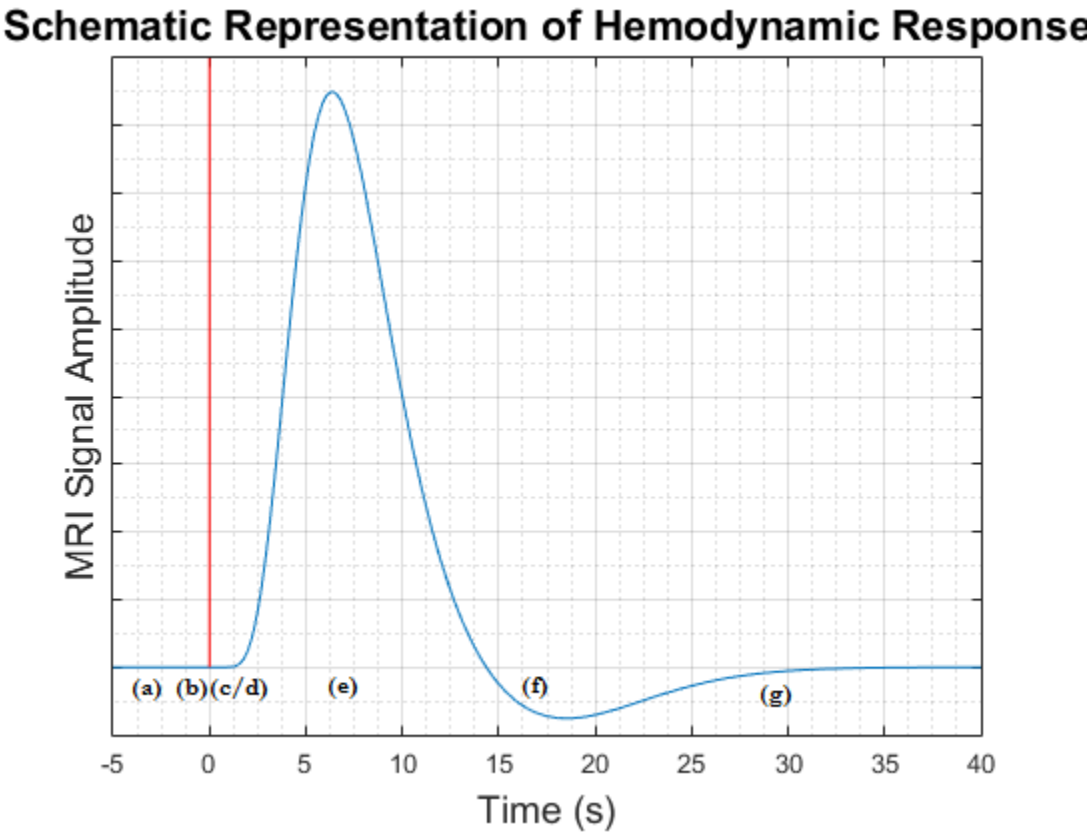

Figure 1. Timecourse of the hemodynamic response to a brief stimulus.
The exact shape of the timecourse varies based on the degree of the response and the brain region, but will generally resemble the figure. A few important regions can be seen: (a) baseline signal. (b) stimulus. (c) short delay. (d) initial dip, not shown since it is not reliable. (e) signal increase. (f) undershoot, decrease below baseline. (g) return to baseline. The timeline for the whole response is approximately 30 seconds, but the shape and timing varies between areas and stimulation paradigms.

5.6.8 **BOLD & Neuronal Activity**

The stated but unverified assumption with the BOLD signal was that it reflected changes in the activity of neurons within a voxel. This assumption was not verified for the PBR until 2001, when Logothetis et al. [56] performed invasive local-field potentials (LFP) and multi-unit activity (MUA) measurements simultaneously with BOLD measurements in anesthetized monkeys. MUA is mostly representative of neuronal action potentials close to the electrode (on the order of hundreds of microns [57, 58]), and can be roughly viewed as the output of neurons.

The LFP represents the activity of dendrites and the soma of neurons in the general area around the neuron (a few millimeters [59, 60]), and can be viewed as the input to neurons. By comparing the BOLD signal to the underlying neuronal activity, Logothetis et al. found that the PBR was best explained by the LFP. As stated by the authors, this finding suggests that the BOLD signal is tightly-coupled with energy-expensive synaptic activity rather than action potentials.
Although the relationship between neuronal activity and the BOLD signal was demonstrated, there still remained the fact that the BOLD signal is dominated by large blood vessels, particularly veins in gradient-echo scans [61], indicating that the detected activation might not reflect local changes in neuronal activity. Intuitively, this is due to changes in deoxyhemoglobin that propagate in large veins beyond the activated region. The change in deoxyhemoglobin occurs primarily in veins, which receive more oxyhemoglobin than they would otherwise. The result is that the BOLD signal is seen slightly downstream from areas of neuronal activity [62]. This problem can be somewhat mitigated by the use of higher static field strengths [63], since the transverse magnetization constants T_2 and T_2* of blood are smaller at higher field strengths relative to the tissue T_2 and T_2* [64].

5.6.9 **Negative BOLD Response**

Whereas the positive BOLD response refers to an *increase* in the MRI signal caused by the hemodynamic response, the negative BOLD response (NBR) refers to a *decrease* in the signal. The decrease in blood flow was thoroughly tested by Shulman et al. [65] for PET, and was reported in fMRI shortly afterwards [66, 67, 68, 56]. The NBR was not directly explored until 2002 [69], where it was systematically compared to the PBR in the human occipital cortex.
The exact origin of the NBR is still somewhat controversial, but there is increasing evidence that it is caused by changes in neuronal activity. Early results [67, 70, 71] hypothesized that the NBR was a result of the adjacent PBR, the intuitive reasoning being that an increase in blood flow to one area of the brain would cause a decrease in nearby areas. This result was supported by an optical imaging study in rats [72] that showed there was no significant change in neuronal activity when they detected the NBR. Although the experiment used optical imaging instead of fMRI, the two are closely tied since they both look at changes in blood oxygenation. Another study in ischemia-induced rats used laser-Doppler measurements to measure blood flow in the cerebellum simultaneously with electrical activity [73], and found a decrease in blood flow

associated with a decrease in neuronal activity. In 2004, a study by Stefanovic et al. [74] used an experimental paradigm known to cause a decrease in neuronal activity in the ipsilateral motor cortex and reliably detected the NBR. Further, their data was consistent with one of the possibilities proposed earlier [69], where the NBR was caused by a small decrease in $CMRO_2$ but larger decrease in CBF. A few years later, Shmuel et al. [75] looked into relating the NBR to neuronal activity by applying the methods previously used for the PBR [56]. As before, the study looked at V1 in anesthetized macaques. The results were in-line with the findings for the PBR; the NBR was closely related to the LFP, which decreased with the introduction of the stimulus and immediately preceded the NBR. Although the results did not entirely rule out a vascular contribution to the NBR, they did show that at least 60% of the NBR was explained by decreases in neuronal activity. Further evidence for the neuronal activation was brought forward in 2014 by Mullinger et al. [76], who performed simultaneous EEG-BOLD-CBF in humans to show a decrease in mu-band (8-12 Hz) power that was concurrent with the NBR and decreases in CBF. Recently, two papers by Goense [1] and Huber [2] explored the layer-dependence of both PBR and NBR. The 2012 paper by Goense et al. investigated the responses in anesthetized macaques. Goense et al. used a 4.7T MRI to measure BOLD, CBV, and CBF signals while the NHPs were shown two concentric checkerboard rotating rings. The stimulus was previously shown to elicit both PBR and NBR [69, 75]. One advantage of this stimulus is that the layout of V1 places the NBR between two areas that showed a PBR. The CBV-weighted signal was acquired by injecting monocrystalline iron oxide nanoparticle (MION), a contrast agent which changes T_2 and T_2^* of nearby voxels. The CBF was measured using arterial spin labeling (ASL), which excites protons before they enter the brain (typically in the neck) and measures the signal in a slices within the brain. Another image is taken without first exciting the protons. When the difference is taken between the two volumes, the signal is strongest in areas which received the most labeled protons (the areas with the highest CBF). In areas of PBR, Goense et al. found BOLD, MION, and CBF signal changes of 1.7% ± 0.6%, -6.8% ± 3.4%, and 21.1% ±8.1% (mean ± standard deviation) respectively. In areas of NBR, they found changes of -0.4% ± 0.2%, -1.7% ± 0.7%, and -6.7% ± 2.9% for the same signals. Note that the negative MION response associated with NBR reflects an increase in CBV. The resolution of their scans allowed them to find differences in the laminar profile of the neurovascular coupling in both the positive and negative responses; the results are summarized in Table 1.

Table 1. Laminar profile of positive and negative responses (NHP) from Goense et al. 2012.

Positive Response Type	Laminar Profile		Negative Response Type	Laminar Profile
BOLD	Maximum at cortical surface		BOLD	Maximum at cortical center
CBV	Equal between surface and center.		CBV	Maximum around layer IV
CBF	Maximum around layer IV		CBF	Maximum at cortical surface

As can be observed from the amplitude values, the signals associated with the NBR are much smaller by a factor of roughly 1/4. The change in CBV was the surprising result of this study; in both the positive and negative responses, they found a decrease in the MION signal (an *increase* in CBV). This was a surprising result, as it contradicted previously-reported results [70] that showed a decrease in CBV for areas of NBR. There were several changes in the experimental procedure that could account for the differences: anesthetics, species, and posture. Nonetheless, the results offer evidence that the mechanisms behind the PBR and NBR differ, despite the strong similarities seen up to that point.

Huber et al. performed a similar high-resolution fMRI experiment two years later, using alert human subjects instead of NHPs [2]. Whereas the monkey experiments showed an *increase* in CBV, the results in humans showed a *decrease* in CBV in NBR regions, consistent with previous reports on NBR but inconsistent with the NHP results. In that study, three stimuli were compared. The first stimulus was two rotating concentric rings, similar to the one used in Goense et al. 2012. The second stimulus was a small flickering checkerboard, and the last was a full-field flickering checkerboard. BOLD measurements were acquired in the same manner as in the 2012 paper, but CBV measurements were acquired using a CBV-sensitive pulse sequence, SS-SI-VASO[8]. CBF was acquired using pulsed ASL, which didn't give enough resolution to compare the response in the cortical surface and deeper layers. The results for the positive and negative responses are summarized in Table 2.

[8] SS-SI-VASO: Slice Selective Slab Inversion Vascular Space Occupancy

Table 2. Laminar profile of positive and negative responses in humans from Huber et al. 2014.

Positive Response Type	Laminar Profile		Negative Response Type	Laminar Profile
BOLD	Maximum at cortical surface		BOLD	Equal between cortical surface and deeper layers
CBV	Equal between cortical surface and deeper layers		CBV	Maximum at cortical surface

The same CBV measurements were repeated in NHPs in order to compare the results of the new pulse sequence (SS-SI-VASO) with those obtained via a contrast agent. The NHP results using SS-SI-VASO were consistent with previous NHP results, but inconsistent with the new human results. Several possibilities were suggested to explain the difference, such as differences in fixation, experimental setup, arterial pressure due to anesthesia or posture, or in interstitial space and CSF dynamics in anesthesia.

Interestingly, [1] and [2] showed, in addition, inconsistent magnitudes of NBR between alert human and anesthetized primates in response to rotating checkers stimuli. In primates, rotating checkerboard elicited PBR of 2% and NBR of -1% relative to baseline. In alert human subjects, the number of voxels for the NBR rotating ring was smaller than the number of activated voxels with the flickering stimulus (81 for rotating vs. 960 for flickering). Whereas the PBR in response to both flickering and rotating checkerboard was similar to that obtained in primates in response to rotating checkerboard (~2%), the NBR was not. Flickering checkerboard stimuli elicited NBR (-1%); in contrast to the results in primates, rotating checkerboard elicited only a diminished NBR (-0.0006%). Thus, NBR was more readily detected with the rotating checkerboard in monkeys than in humans.

These two inconsistencies between non-human primate (NHP) and human studies, with regard to the sign of the cerebral blood volume response associated with NBR and the magnitude of the NBR to rotating checkers stimuli, motivate my study. For more details, please see the sections on motivation, hypothesis and objectives above.

6 Methods

6.1 Data Acquisition

6.1.1 **Software**

All training, stimulus presentation, and gaze calibration was performed using the MonkeyLab platform for MATLAB [77], written by Prof. Erik Cook (Department of Physiology, McGill University) and Vincent Beliveau. Monkeylab allows the integration of different modules to control several aspects of an experiment (e.g., stimulus presentation, gaze calibration, data acquisition, etc.). Custom code stimulus presentation and calibration was written by Ze Shan Yao, Martin Villeneuve, and myself for our specific experiments. MonkeyLab's stimulus presentation is created and displayed using the Psychophysics Toolbox [78, 79, 80]. EyeLink data is obtained via the EyeLink toolbox [81].

6.1.2 **NHP Training**

Our goal is to stimulate the visual cortex in a known and predictable manner to trigger the NBR. Two types of visual stimuli were chosen, and each one requires the subject to fixate on a specific point for the duration of the task without moving. Humans can do this with relative ease, but NHPs require intensive training for us to be able to extract useful information from the MRI.

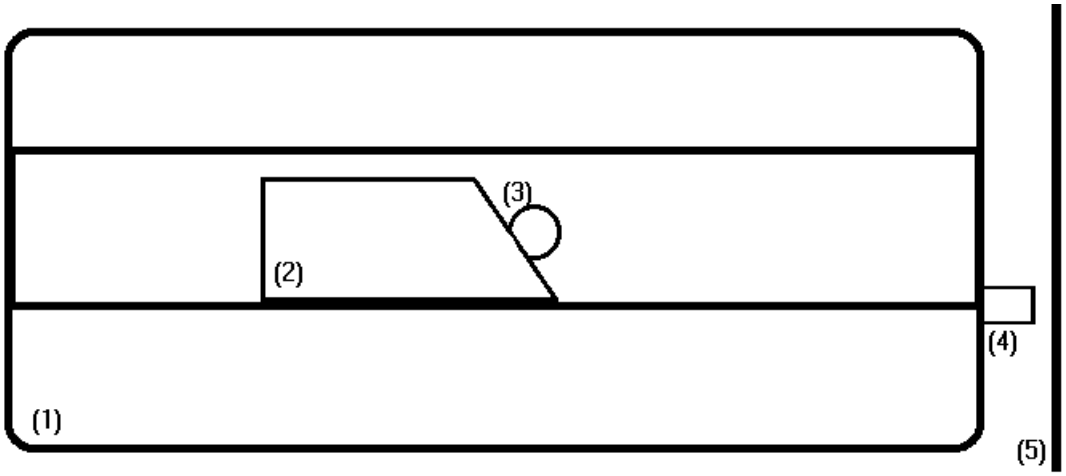

Figure 2. Schematic representation of the positioning of the NHP in the MRI.
(1) Scanner. (2) NHP chair. (3) Eye-tracking camera. (5) Projection screen.

The NHP is gradually trained to enter a box ("chair") which will contain it for the duration of the

experiment. The chair is designed such that the NHP's head will be pointing towards a screen. An MRI-compatible post [82] was surgically attached to the skull. After a recovery period, the post allows us to secure the head directly to the chair and prevent head movement during the MRI. The chair and headpost holder were designed by Rogue Research [83]. Modifications specific to our setup were designed by Dr. Shmuel. The chair was constructed by Hybex Innovations [84].

At this point, the NHP is largely immobile, but won't fixate on a given spot. The fixation training is rather demanding, and it is necessary to restrict access to fluids so that the animal will seek out fluid sources wherever possible. Using a combination of our stimulus, a gaze tracker, and a juice dispenser, we are able to give juice when the NHP's gaze falls within an acceptable margin of the fixation point. The NHP gradually learns to fixate on the point for longer periods of time.

The real MRI environment is more complex than a simple screen, and it is necessary to acclimate the NHP to similar conditions before the real scan since NHPs are easily upset by new objects and environments. Environment confounds are added gradually across sessions, depending on the NHP's performance. The gaze training is performed in a tube that has a screen at one end and a slide-in table at the other. The NHP is slid into the tube, where it can see a screen. The tube is equipped with speakers, which play the sound made by different MRI pulse sequences. Since our experiment uses coils placed around the visual cortex, fake coils are used during the training. The duration of the training sessions is progressively increased to about 90 minutes per session; although the scans will not typically last that long, it is important that the NHP remains calm and willing to work throughout the entire scan in order to allow for efficient data acquisition.

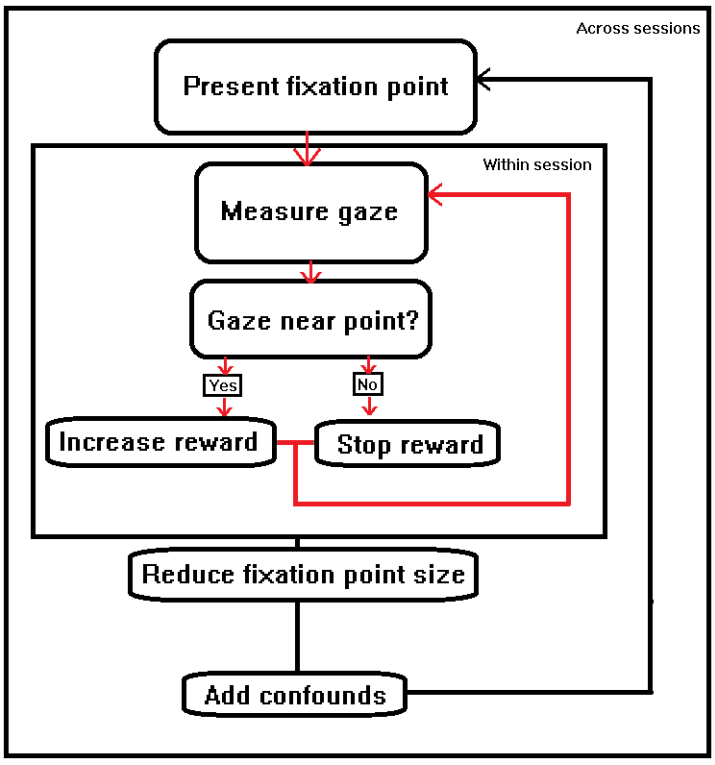

Figure 3. Training Flow Chart

The second part of the experiment, measuring CBV-weighted fMRI, requires the intravenous injection of a

contrast agent. Perhaps unsurprisingly, NHPs don't like being held and poked with syringes, and require some habituation before it can be done with minimal risk. The first part of the training requires opening part of the chair, holding the animal's leg for a period of time, letting go, then giving a juice reward. The process is repeated until the NHP can be held calmly for at least 60s. The process is summarized in Figure 3.

6.1.3 **Stimuli**

Four stimuli were used: two types, each with two sets of parameters. The stimuli were either a flickering or rotating checkered ring, with either a small or large radius. The stimuli were presented on a background of mean luminance so that the total illumination would remain fixed. When no stimulus is shown, only the fixation spot and mean luminance background is displayed. Figure 4 shows the stimulus.

The flickering ring inverted the black/white checkers at a rate of 8Hz (16 inversions/s). The rotating ring rotated at a rate of 60 degrees/s, and reversed direction every 2s. All other parameters were identical across stimulus types.

Small rings had an inner radius of 1 degree of visual angle and outer radius of 4 degrees of visual angle. Within these rings were 7 sets of checkered rings, each containing 24 checkers.

Large rings had an inner radius of 5 degrees of visual angle and outer radius of 12 degrees of visual angle. Within these rings were 8 sets of checkered rings, each containing 48 checkers.

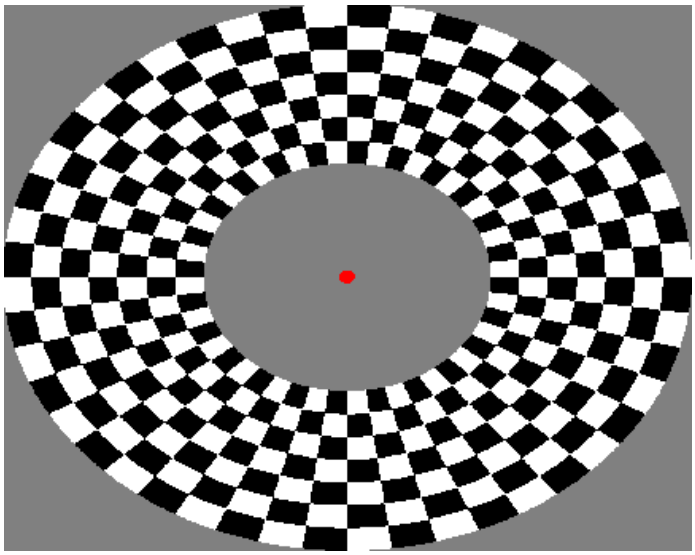

Figure 4. Image of the large stimulus.

The smaller stimulus is similar, with an extra ring and larger checkers to maintain a similar size.

6.1.4 **Stimulus Presentation**

The stimuli were projected on a back-projection screen at the end of the MRI bore. Changes in stimulus conditions ("on" vs. "off") were aligned with the MRI's volume acquisition via triggers sent by the scanner. Due to the low amplitude of the NBR, only one stimulus type was presented per session to allow averaging over multiple runs within the session. The display progresses with every trigger, and can be converted to time by multiplying by the sequence's TR (2s). No stimulus-onset asynchrony was used.

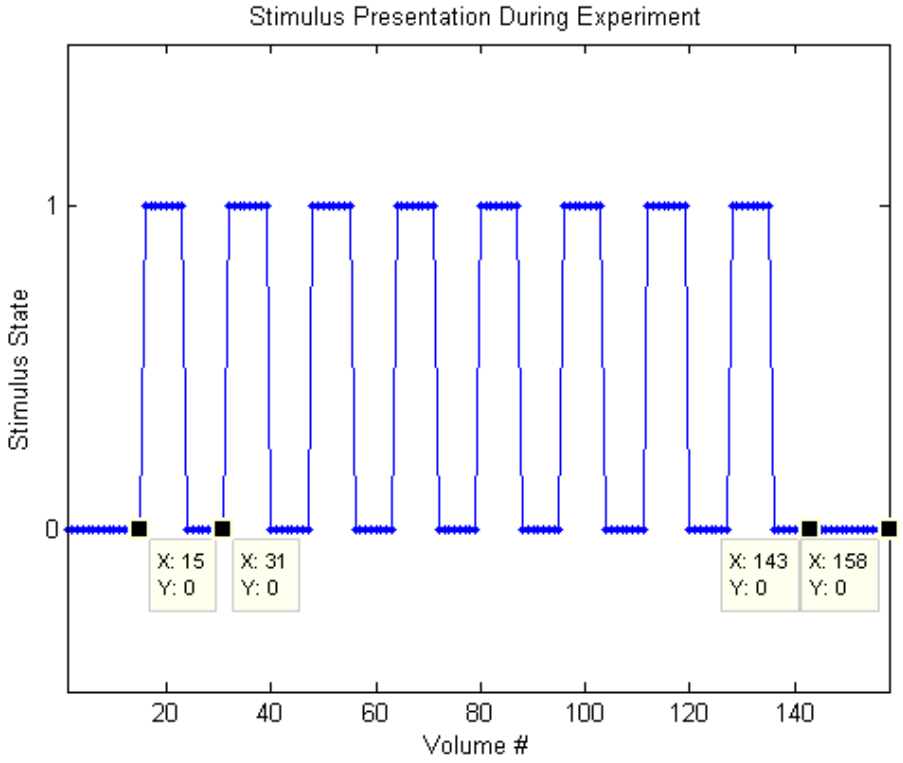

Figure 5. Timing of the stimulus presentation.

A value of 1 indicates the stimulus was being shown. A value of 0 indicates that only the fixation spot appeared on the screen. The timing is: initial 15 volumes baseline, followed by 8 repetitions of 8 volumes on, 8 volumes off, ending with 15 baseline volumes.

6.1.5 **Gaze Tracking**

The EyeLink 1000 Plus from SR Research was used for eye tracking. The gaze tracker was calibrated at the start of every experiment by moving the fixation spot to five predetermined locations: one at the center of the screen, and four in the corners of a square with a length of 1

degree. The calibration is done by multiplying the outputs of the EyeLink (x- and y-position of gaze) with a calibration matrix. The matrix is 3x2, with the last row containing the translation. While the calibration points are presented, the gaze position is measured until it is within a given margin of the point. Based on the average location, a small correction is made to the calibration matrix so that the average location moves closer to the dot's location. By repeating this while the dot is at different locations, we can gradually reduce the margin. If the system is completely uncalibrated (e.g. in a new environment), the system requires some manual intervention before the gaze calibration can be automated. During the experiment, the animal's gaze is tracked and saved for future analysis. As with training, juice is given only when the gaze falls within a small area around the fixation spot.

6.1.6 **MRI**

MRI data was acquired using a Siemens TrioTim 3T scanner (actual strength: 2.89T). Several images were acquired: T_1-weighted structural images, phase-reversed images for distortion correction, T_2^*-weighted BOLD volumes, and T_2^*-weighted CBV volumes. The first three volumes of every scan were not recorded to allow the magnetization to reach steady-state.

T_1 structural

Before any experiments were performed, a high-resolution T_1 image was acquired while the NHP was anesthetized. It was used as a structural reference volume; all acquired data was registered to this volume.

At the start of every experiment, an in-session T_1-weighted volume was acquired as an intermediate registration step between the functional data and the high-resolution structural image.

BOLD Images

T_2^*-weighted images were acquired to detect the PBR and NBR. Volumes were acquired with a limited field of view that focused on the occipital cortex by applying two saturation bands to remove N/2 ghosting. Refer to Table 3 for scan parameters. Images with a reversed phase encode direction were acquired for distortion correction; all other parameters were unchanged.

CAB Images

There are a few ways to get a CBV-weighted signal that does not require an external contrast agents. These were excluded in favour of ferumoxytol either because they were difficult to use

with NHPs or did not have a comparable fCNR. Vascular space occupancy (VASO) and its variants (SS-VASO, SS-SI-VASO) have a signal change of about 2% during visual stimulation with a checkerboard [85]. A later VASO study reported similar results for finger tapping [86] at 7T. By comparison, ferumoxytol at 3T caused signal changes of 6-8% during a finger-tapping task [87] without correcting for BOLD contamination. Given that the NBR has a much smaller amplitude [69], ferumoxytol was selected to measure CBV over pulse sequences to increase our chances of detecting changes associated

Contrast agents in fMRI (and imaging in general) serve to amplify magnetic differences in biological tissues. Contrast agents specific to MRI affect the local B-field, typically by reducing the values of T_1, T_2, or T_2^*. One class of contrast agents are iron oxide nanoparticles, which cause a strong decrease in T_2^*. The contrast agent used in this study, ferumoxytol is injected and causes blood vessels to appear much darker than they normally would. Since ferumoxytol has a very long half-life (>15 hours [88]) in humans, it lends itself particularly well to tracking CBV. Changes in blood volume directly affect how much ferumoxytol is in a voxel, and the effect is more significant than the signal changes caused by oxygenation differences. Ferumoxytol reduces the T_2^* of grey matter by approximately half [87], and the acquisition TE is consequently cut in half. Knowing that assuming that the T_2^* of the contrast agent and blood can be considered additive with relatively small error [89], the reduced TE reduces the BOLD contribution to the signal by a factor of approximately 1.5 [9]. Without further correcting for the BOLD contribution, estimations of CBV change will have an error of 10-20% [89].

CAB images were acquired using a T_2^*-weighted sequence, with a different TE and echo spacing to account for the changes caused by the injected contrast agent. Two saturation bands were applied to limit the field of view (FoV) to the occipital cortex and remove N/2 ghosting. Refer to Table 3 for scan parameters. The saturation bands allowed for a narrow FoV in the phase encoding direction, which allowed for high-resolution fMRI. Images with a reversed phase encode direction were acquired for distortion correction; all other parameters were unchanged.

[9] The signal in the transverse plane decays by $e^{-\frac{TE}{T_2^*}}$. Comparing TE = 16ms to TE = 30ms and assuming a T_2^* of approximately 30ms, we see that the shorter TE causes the measured signal to be 1.5 times larger.

Measurements

One transmission coil was used to produce the MRI signal and two sets of surface coils were used to measure it. The coils were produced by Windmiller Kolster Scientific [82]. The transmission coil was placed above the NHP's head (see Figure 6). The two sets of reception coils were placed around the head; one pair on the right side of the NHP's head, the other placed behind the approximate location of V1. Data was reconstructed using a sum of squares (part of Siemens' software, description of method can be found here: [90]). In order to maximize the SNR, all coils were tuned to the Larmor frequency (123.2 MHz) after being placed around the NHP's head, but before the scanning session. Tuning was done using the 505NV+ RF Sweeper from Morris Instruments [91]. The asymmetric positioning was selected to maximize our chances of finding the low-amplitude NBR in single trials. Pilot experiments with symmetric placement failed to show runs with any single-trial activation, while the asymmetric positioning had a few single-trial activations. Single-trial activations were later dropped in favour of averaging over runs for simple statistical power, but the asymmetric positioning was retained so that later acquisitions would be consistent with previous ones. Consequently, our acquisitions are more sensitive to one side of the head than the other, removing our ability to address the symmetry of possible activations. Given that our stimuli are all circular, the asymmetry was not a large concern.

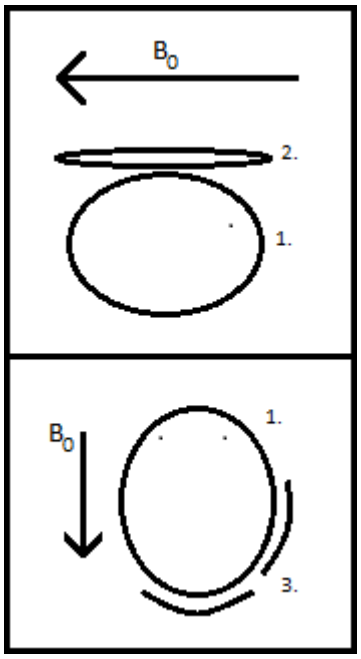

Figure 6. Coil placement around NHP's head. 1. NHP's head. 2. Transmission coil. 3. Reception coils.

6.1.7 **Summary of MRI Sequence Parameters**

Table 3: MRI sequence parameters

	T_1 structural	BOLD	CAB
Voxel size	1x1x1 mm^3	1.3 x 1.3 x 2.0 mm^3	1.3 x 1.3 x 2.0 mm^3
TR	2000ms	2000ms	2000ms
TE	3.43ms	30ms	16ms
TI	900ms	-	-
Weighting	T_1	T_2^*	T_2^*
Flip angle	9^o	90^o	90^o
Bandwidth	240 Hz/Px	1370 Hz/Px	946 Hz/Px
Echo spacing	7ms	0.83ms	0.94ms
Slice acquisition	Ascending	Interleaved ascending	Interleaved ascending
EPI Factor	-	36	36
Partial Fourier	No	No	6/8

6.2 Analysis

The initial steps of the analysis were performed using various FSL [92, 93, 94] tools (FEAT, MCFLIRT [95], FUGUE).

6.2.1 **Brain extraction**

The scalp was removed before any processing was done. This step is necessary to ensure a good registration in the brain. Due to the extra muscle and the limited FoV, FSL's brain extraction produced very poor results; consequently, brain extraction was performed manually for both structural and functional scans.

6.2.2 **Motion outliers**

Volumes that showed excessive residual motion were excluded from the statistical analysis by including an explanatory variable to account for them. Residual motion in a volume was measured by comparing the RMS of the difference of intensity values between the volume and the reference volume. Excessive motion is based on the percentile ranking of the RMS of all corrected volumes; an RMS value exceeding the 75^{th} percentile plus 1.5 times the interquartile range is considered an outlier (this is the default for FSL's fsl_motion_outlier). In terms of the

general linear model (GLM), a column of zeroes was added with a single 1 at the index corresponding to the outlying volume.

6.2.3 **Pre-processing**

Preprocessing was performed by FEAT, and included the following steps. Motion correction was performed using MCFLIRT, which uses a rigid-body transformation to register the volumes within a run to themselves. Slice timing was corrected for interleaved acquisition. The data was prewhitened[10] using FILM. The data was spatially smoothed using a 1mm FWHM Gaussian. A temporal high-pass filter with a cutoff of 0.01Hz was used. Distortion correction was performed by acquiring volumes with reversed phase encoding polarities. The resulting image has opposite spatial distortions, which tools like FSL's FUGUE can use to do non-linear registration to correct the distortion. The method is fully described in [96].

6.2.4 **GLM**

The base GLM uses logical values for the state of the stimulus: 1 for on, 0 for off. The activation model is then convolved with a model of the hemodynamic response (the model is termed the hemodynamic response function, HRF) to model the expected timecourse of the signal. The model timecourse is high-pass filtered using the same filter as in the pre-processing step. The derivative of the HRF is also added to the GLM to compensate for small time shifts in the HRF[11]. Finally, regressors accounting for motion outliers for each volume are added individually to the GLM. The GLM is then used to compute t-maps for every volume to find voxels with significant activation.

6.2.5 **Registration**

All data was registered to a common, high-resolution T_1 structural image acquired while the NHP was anesthetized. The functional data was first registered to an intermediate T_1 image that was acquired in the same session. The intermediate image is then registered to the high-resolution image, and the overall transformation is applied to the functional data. Since applying

[10] The GLM formulation assumes white noise, which is not always the case with MRI data. Prewhitening estimates the relation between timepoints and reduces it to make the GLM assumption valid.
[11] Similar to a first-order Taylor approximation.

the transformations to the data causes interpolation errors, the transformation is applied only when averaging multiple data sets. The functional-to-intermediate registration used 3 translation parameters with a small search space since both were acquired in the same session. The intermediate-to-standard registration used 3 translation and 3 rotation parameters.

6.2.6 **Averaging**

Since the NBR has a low SNR, it is necessary for us to average multiple functional runs together. All runs are registered to a common space (high resolution T_1) and then averaged. The resulting statistical maps (obtained by t-tests) shows voxels with significant activation, and can subsequently be used in cluster analysis using Gaussian random field to account for multiple comparisons. The analysis for PBR used a voxel Z-threshold of 2.3, whereas the analysis for NBR used a voxel Z-threshold of 1.0. Since the contrast agent-based (CAB) signal is reversed relative to CBV changes (an increase in CBV causes a decrease in signal, and vice versa), the opposite was done: the negative response used a Z-threshold of 2.3 and the positive response used a Z-threshold of 1.0. Given the sometimes-capricious nature of NHPs, the number of trials varied with the NHP's willingness to work.

Table 4. Number of trials averaged together for each condition.

Stimulus	Acquisition	Repetition	Number of Trials
Small flickering	BOLD	1	7
Small flickering	BOLD	2	7
Small rotating	BOLD	1	8
Large flickering	BOLD	1	7
Large flickering	BOLD	2	8
Large rotating	BOLD	1	7
Small flickering	CAB	1	5
Small rotating	CAB	1	5
Large flickering	CAB	1	6
Large rotating	CAB	1	6

6.2.7 **Baseline**

This section contains the information for producing the plots in the results section. Baseline value was taken as the first ten volumes and the two volumes immediately preceding the stimulus. Consequently, the reported percent change represents the amplitude difference between the BOLD signal just prior to stimulation and the peak of the response.

7 Results

7.1 Gaze Position

Throughout every experiment, the NHP's gaze was tracked and recorded. The following figure show the gaze position throughout an entire session. Blinks were interpreted as either NaN or very large values (>100 degrees) and were excluded from the presented data. When the NHP partially closed his eyes, it was typically interpreted as left-right motion.

As can be seen from all the plot below, the NHP's gaze was well-fixed on the center point. Non-zero means are attributed to two reasons. Primarily, calibration is accurate to only 0.5 degrees in either the x- or y-direction. Secondly, partial eye closure tends to register as a gaze shift towards the left (negative x). In either case, the tight grouping in all cases indicates that the NHP's gaze was very good and within the 1-degree window around the center. Figure 7 shows the heat map from only one experiment, but is very similar to the others (see appendix for other experiments). The mean and standard deviation of the gaze position for all experiments is given in Table 5.

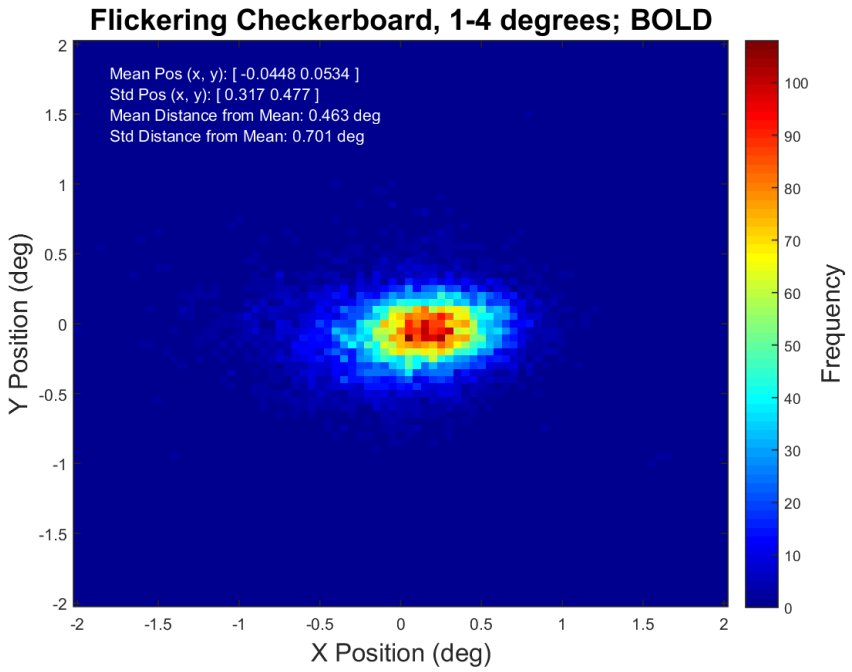

Figure 7. Heat map of the NHP's gaze during the first small flickering BOLD experiment.

Table 5. Gaze statistics.

Experiment	Mean Gaze Position (deg)		Standard Dev. Of Position (deg)		Mean Distance from Mean Position (deg)	Standard Dev. Of Distance from Mean (deg)
	x	y	x	y		
Small Flickering BOLD (1)	-0.0448	0.0534	0.317	0.477	0.463	0.701
Small Flickering BOLD (2)	-0.0303	-0.201	0.298	0.347	0.380	0.540
Large Flickering BOLD (1)	-0.133	-0.237	0.316	0.408	0.417	0.557
Large Flickering BOLD (2)	0.0253	-0.112	0.291	0.401	0.405	0.588
Small Rotating BOLD	-0.26	0.0795	0.288	0.436	0.436	0.541
Large Rotating BOLD	-0.047	-0.0209	0.305	0.465	0.445	0.619
Small Flickering CAB	-0.0726	0.218	0.287	0.68	0.587	0.745
Large Flickering CAB	-0.0209	0	0.349	0.545	0.553	0.783
Small Rotating CAB	0.0643	0.21	0.27	0.614	0.541	0.603
Large Rotating CAB	-0.027	0.0146	0.34	0.503	0.525	0.811

Table 6. Gaze statistics.

For each experiment, the average position and the distance from the average position are shown. The mean gaze position gives us the center of fixation, while the distance tells us how much the gaze moves around.

7.2 Flickering Checkerboard

Two goals of this study are addressed in this section. First, we compare both the PBR and NBR to the CAB signal (CBV response). The comparison is made by measuring the responses to a flickering checkerboard, with a total of six experiments being acquired: two sessions for the BOLD response to the small checkerboard, two sessions for the BOLD response to the large checkerboard, and one session for each the CAB response to the small and large checkerboards. The second goal was to test the reproducibility of the PBR and NBR in the alert NHP, which was accomplished by acquiring the BOLD experiments twice and comparing the two sessions

directly, as well as repeating the BOLD-CAB comparison with the two BOLD sessions.

7.2.1 **Activation Maps**

Figure 8 shows the response to different stimuli. The BOLD experiments were repeated once to test reproducibility. The maps for the small stimulus show the PBR in the lateral parts of the occipital cortex, which is the expected retinotopic location [97, 98]. The NBR is near the midline, consistent with existing literature [69, 75]. The CAB signal is reversed relative to the CBV. Ferumoxytol causes a signal drop, and its quantity in a voxel is directly proportional to CBV. There are two important results that can be seen. First, the CAB signal drop (increase in CBV) matches the location of the PBR. Again, this is consistent with existing literature [1, 2]. There is a CAB increase (CBV decrease) around the midline, approximately in the same location as the NBR.

The large stimulus displays a similar pattern. The PBR is observed around the midline in the occipital cortex, but the NBR is detected on only the right side. The matching cluster on the left side failed to reach significance. Both the PBR [69, 75] and NBR [1, 2] locations are consistent with literature. The CAB map corresponds well to the PBR, but the CAB increase (CBV decrease) is only detected in a small cluster on the left side. The matching CAB increase (CBV decrease) on the right side failed to reach significance. Since the NBR and CAB decrease were detected on opposite sides, there is only a little overlap between the two for the large stimulus. We expect the NBR and CAB increase to appear in symmetric coordinates of the visual cortex. Although the contrast-to-noise ratio is low, they appear in the expected coordinates.

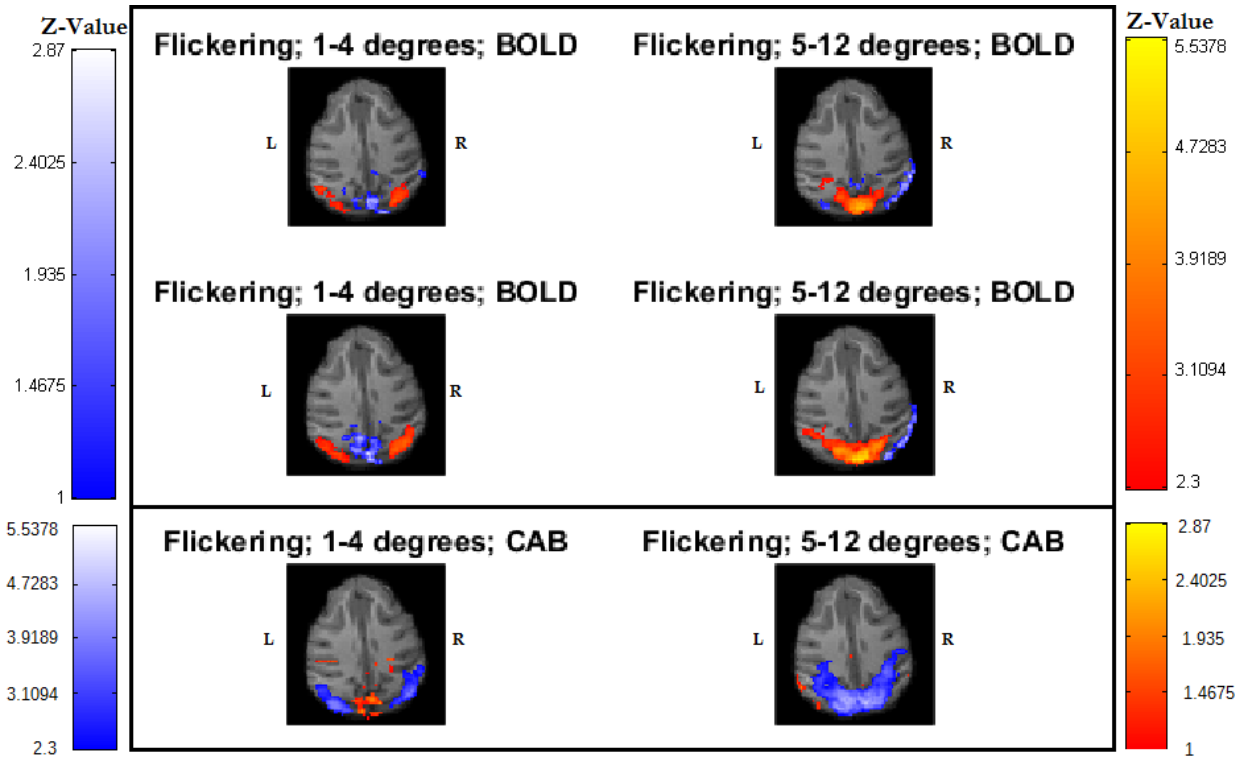

Figure 8. Activation maps (significant Z-values) for the flickering stimuli.
The stimuli for each map was as follows: small (left column) and large (right column) checkerboards, for both BOLD (top box) and the contrast agent based response (CAB; bottom box). All results were obtained from different days, including the two repetitions for the small and large stimulus. Hot colours show areas that had a significant signal increase, cold colours show areas that gave a significant signal decrease.

7.2.2 **Timecourses**

The following figures show the timecourses for the most significant cluster of each activation map. For the case of multiple significant clusters, only the two most significant clusters are displayed. The fitted model for each cluster is superimposed.

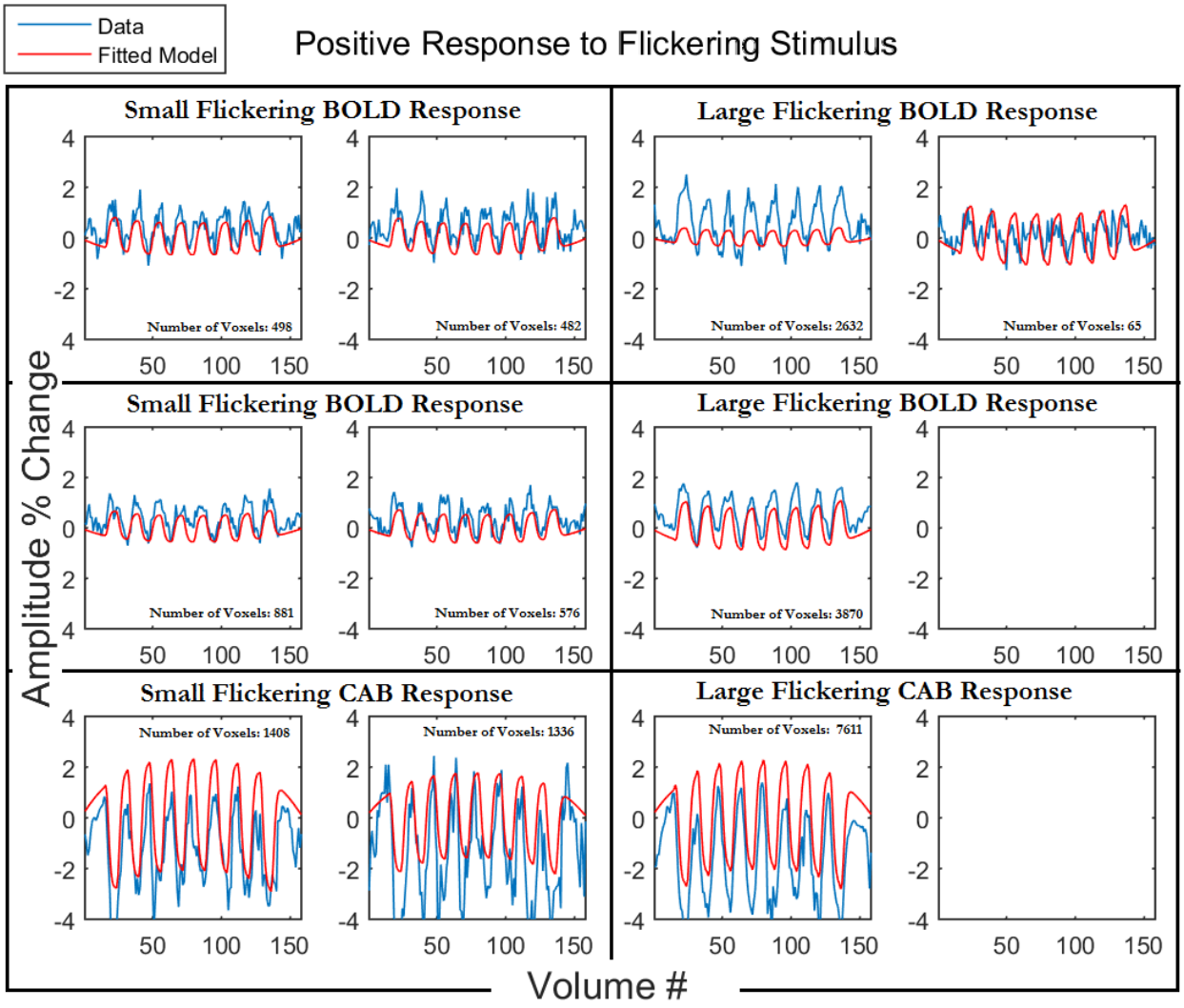

Figure 9. Timecourses the positive response to the flickering stimuli.

The timecourses are averaged over all voxels over the two most significant positive clusters. The most significant cluster is on the left, second-most on the right. The timecourses are in blue, the fitted model is in red. Plot positions correspond to the activation maps of Figure 8. Both the BOLD and CAB experiments had strong responses, and they show a strong similarity to the model. Blank plots indicate that there was only a single significant cluster.

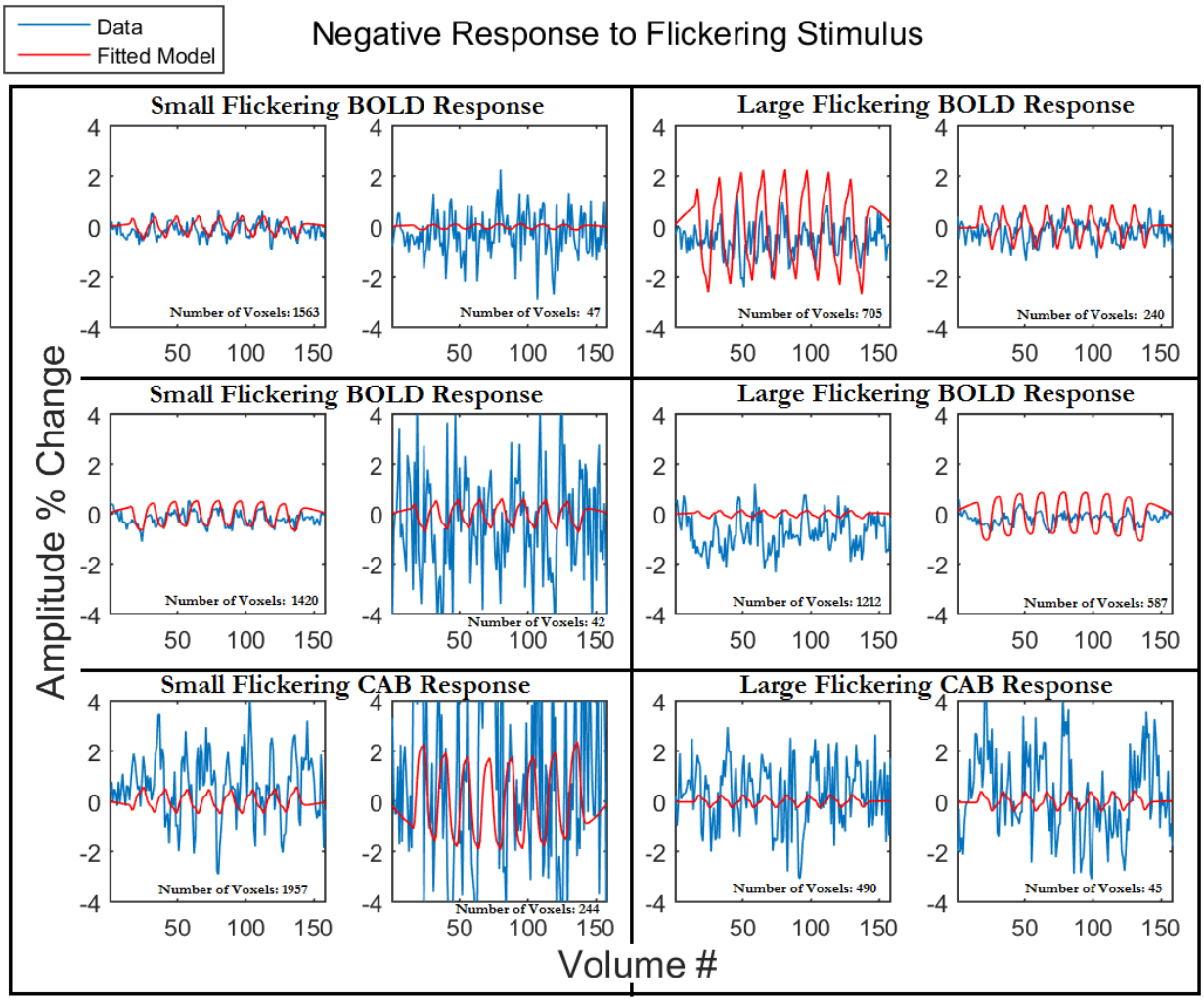

Figure 10. Timecourses for the negative response to the flickering stimuli. Timecourses were averaged over all voxels, and the two most significant negative clusters are presented. The most significant cluster is on the left, second-most on the right. The timecourses are in blue, the fitted model is in red. The timecourses don't match their model as well as those of the positive response, particularly for the CAB response.

7.2.3 **Peristimulus time-courses**

To get an idea of the shape of the response to each stimulation period, we can produce peristimulus plots for each experiment. For each of the plots in Figures 9 and 10, the period immediately following the start of the stimulus was averaged. Sixteen time points were taken, starting from the two volumes preceding the stimulus. Every experiment had eight of these

blocks, and they were averaged together to produce the peristimulus plots. Only the two most significant clusters are plotted (left most significant, right second-most). Plots without a positive response indicate that there was only a single positive response significant cluster. Most of the plots start with at a non-zero value.

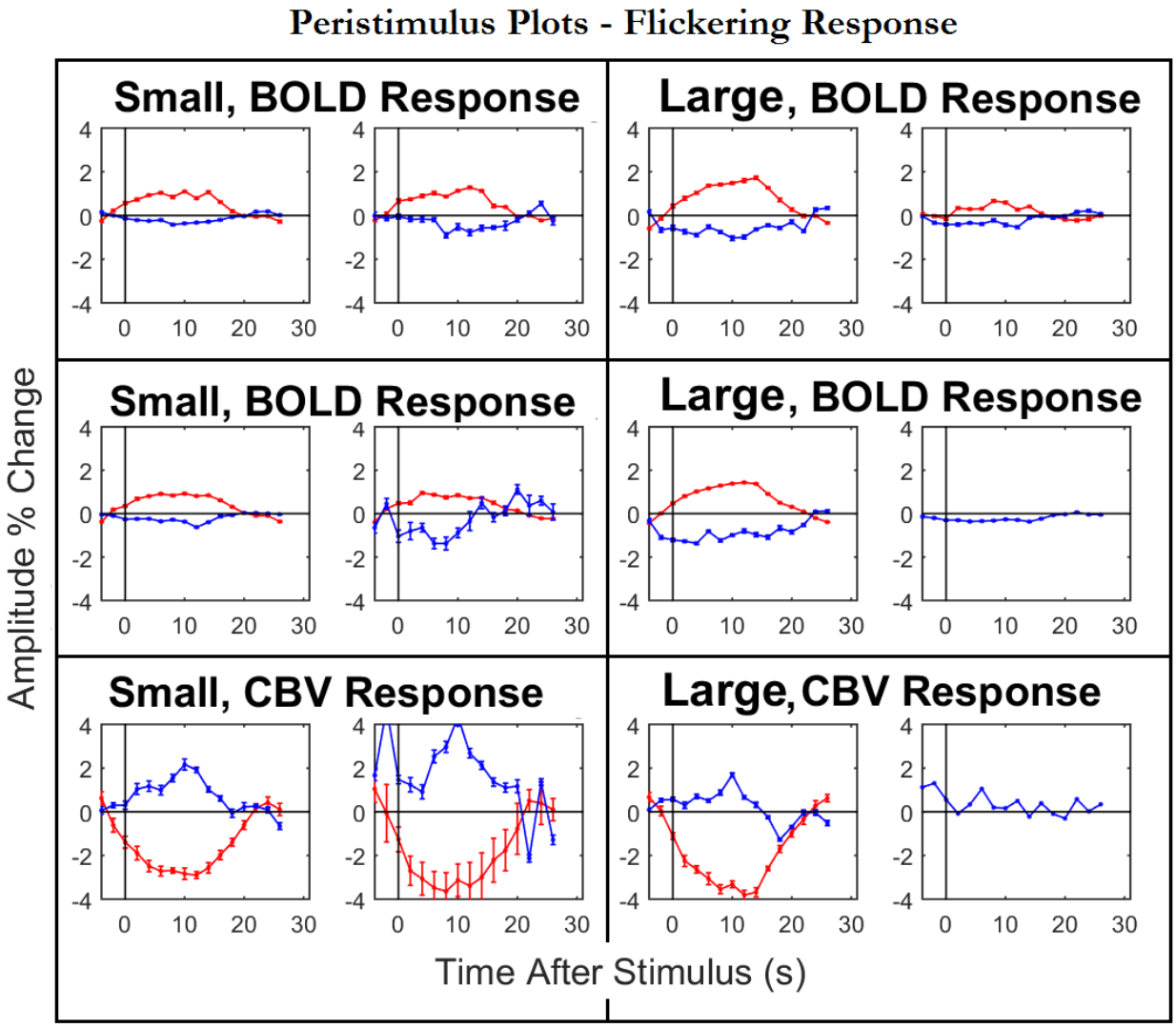

Figure 11. Peristimulus plots for all flickering stimuli.

7.2.4 **Reproducibility**

Both sizes for the flickering checkerboard were tested twice, each time on a separate day. Comparing the response across days can give us an indication of the data's reproducibility. A mask containing only voxels that were significant in both experiments was created and applied to both experiments. The amplitude's percent change from baseline between "on" and "off" sections of the timecourse was computed for each experiment. For stimuli of the same size, the relative amplitude change from one experiment was plotted against the same measure from the same experiment performed on a different day. The mean (circle) and standard deviation (lines) computed over voxels from both experiments are displayed on each plot. Statistics for the plots of this section are summarized in Table 7. To quantify the amount of spatial overlap between the two results, we can calculate the overlap using:

$$Fraction\ Overlap = \frac{2 * N_{overlap}}{N_{Exp1} + N_{Exp2}},$$

where $N_{overlap}$ represents the number of overlapping voxels and N_{Exp1} and N_{Exp2} represent the number of significant voxels in the first and second experiments respectively. Given that our interest is in reproducibility rather than activation, the positive and negative activations are considered separately (i.e., a voxel with negative activation in one experiment and a positive activation in the other is not considered to be overlapping).

Small Flickering Checkerboard

Figure 12 shows good reproducibility for this stimulus, with most points in either the first or third quadrants. There are a few points in the fourth quadrant, indicating that the voxels showed a PBR in one experiment and a NBR in the other. Although undesirable, the result is not surprising since the PBR and NBR regions are very close together. Both positive-positive and negative-negative clusters were significant ($p<0.01$). The positive cluster had (BOLD, BOLD) means of (0.81%, 0.84%), indicating that the average PBR magnitude was comparable over both experiments. The negative cluster had (BOLD, BOLD) means of (-0.34%, -0.34%), indicating that the NBR also had a reproducible magnitude. The fraction overlap was 0.314 for the NBR and 0.552 for the PBR.

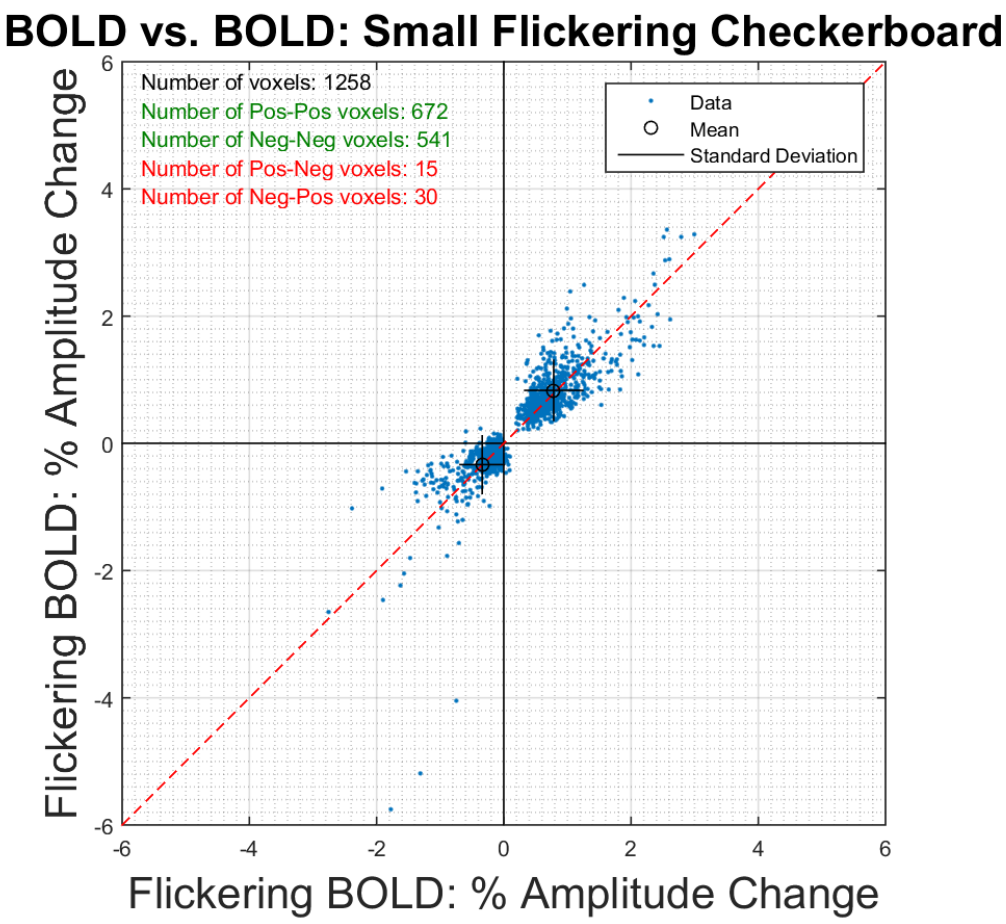

Figure 12. Comparison between small flickering checkerboard on different days.

Large Flickering Checkerboard

The results in figure 13 are comparable to those in figure 12, with most points lying in either the first or third quadrants. We see that there are more than twice as many significant voxels with this larger stimulus (2712 vs. 1258), but that there are fewer NBR voxels (490 vs. 541). Both clusters were nonetheless very significant ($p<0.01$). The positive cluster had (BOLD, BOLD) means of (1.21%, 1.13%), with the 95% confidence intervals overlapping between 1.16 and 1.17%. The negative cluster had (BOLD, BOLD) means of (-0.90%, -0.94%). The fraction overlap was 0.285 for the NBR and 0.673 for the PBR.

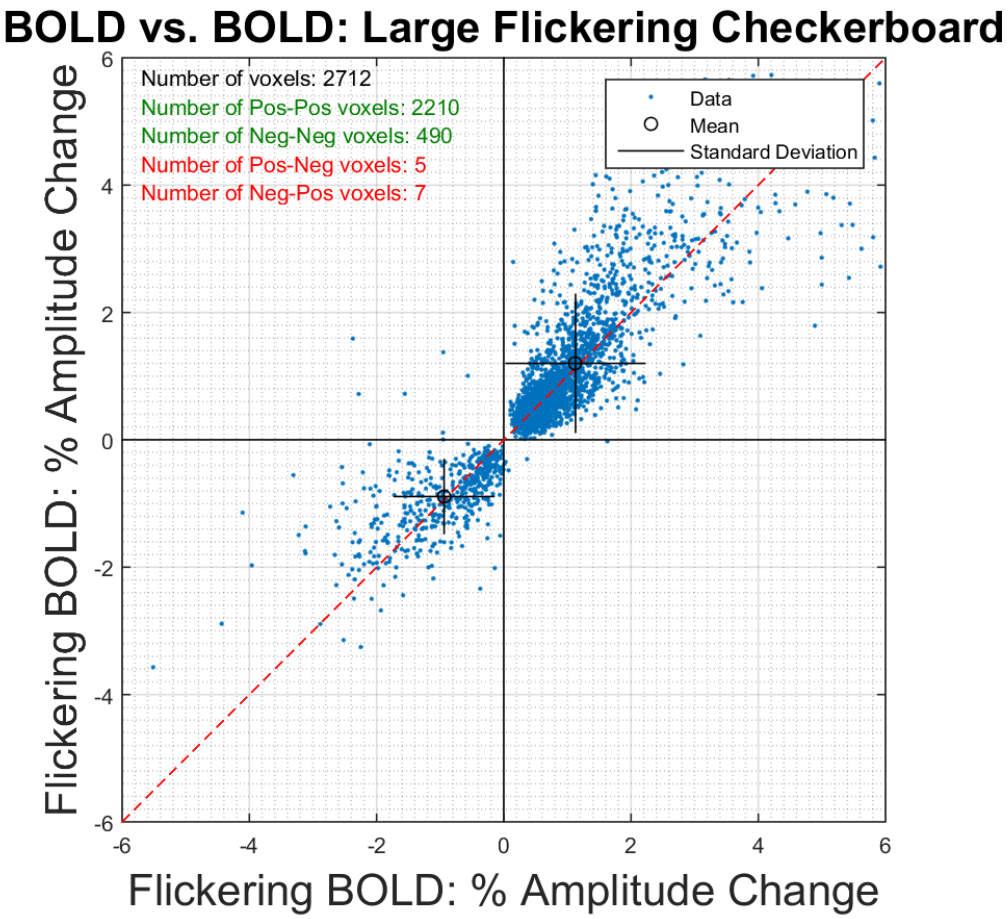

Figure 13. Comparison between large flickering checkerboard on different days.

7.2.5 **BOLD & CBV Relationship**

The main interest of this study is to compare the PBR and NBR to the corresponding CBV response. A process similar to the reproducibility plots is used: a mask was created that contained voxels that were significant in both the BOLD and CBV experiments. The percent change in signal amplitude was compared for the BOLD and CAB signals.

Figures 14-17 show the BOLD-CBV relationship for two sizes of the flickering checkerboard. The smaller checkerboard (figures 14, 15) has a clear relationship: voxels with a NBR have an increased CAB (decreased CBV), while voxels with a PBR have a decreased CAB (an increased CBV). The large checkerboard (figures 16, 17), doesn't show such a clear relationship. With the large checkerboard, voxels with a PBR show an overwhelming preference for an increase in CBV. However, there are almost no voxels which show a NBR that overlap with activated voxels

in the CAB activation map. The NBR voxels are in the right hemisphere, while the activated CAB voxels are in the left hemisphere. The coordinates where the NBR appears (in the right hemisphere, but not in the left hemisphere) can be explained by the low CNR of the NBR and that the RF coils are located immediately next to the activated regions. The CAB signal activation on the opposite side is counterintuitive. However, lowering the Z-threshold for clusters reveals small activation clusters for both NBR and CAB signal on both sides. The mean (circle) and the standard deviation (lines) computed over voxels for both experiments are displayed on each plot. The statistics related to the amplitude changes are included at the end of the results section, in Table 7.

Small Flickering Checkerboard

The CAB responses were compared to the BOLD responses, in the same manner as described in section 7.2.4, but applied to the BOLD and CAB experiments using the small flickering checkerboard. Figures 14 and 15 show a good correspondence between the PBR and the CAB decrease (CBV increase), shown in the second quadrant (428 voxels for both experiments). Similarly, the NBR fits well with the CAB increase (CBV decrease), seen in the fourth quadrant (255 and 254 voxels). All clusters for both repetitions of the BOLD experiment were very significant ($p<0.01$). For Figure 14, the positive cluster in the second quadrant had (CAB, BOLD) means of (-2.44%, 0.77%), and the negative cluster in the fourth quadrant had (CAB, BOLD) means of (0.81%, -0.34%).

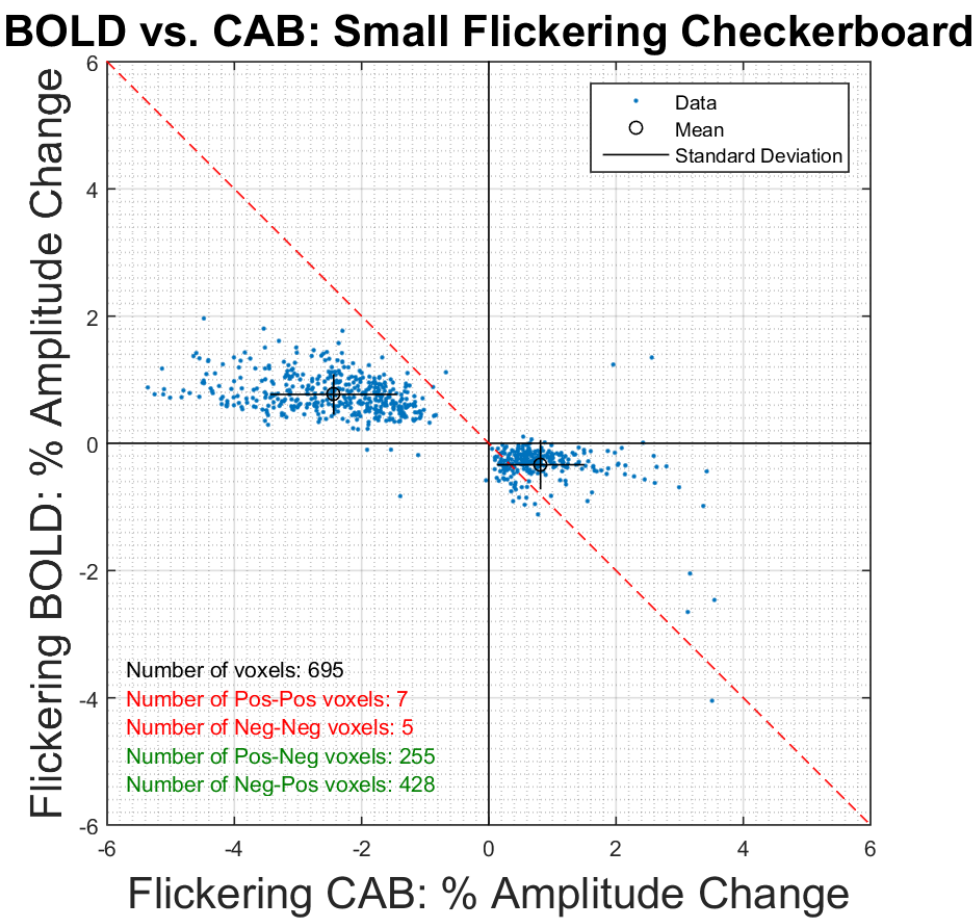

Figure 14. Comparison of the CAB signal and the BOLD response of the first small flickering checkerboard.

The results for Figure 15 are similar to those of Figure 14. Both clusters were very significant ($p<0.01$). The positive cluster in the second quadrant had (CAB, BOLD) means of (-2.44%, 0.77%), and the negative cluster in the fourth quadrant had (CAB, BOLD) means of (0.81%, -0.34%).

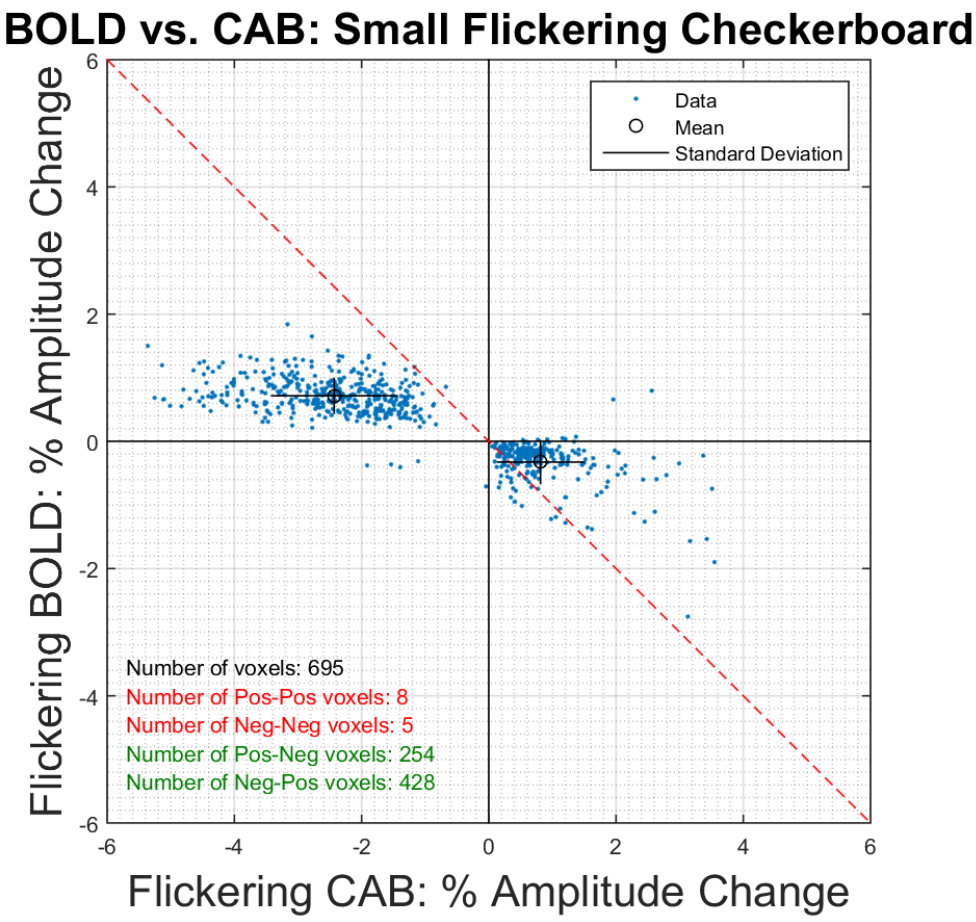

Figure 15. Comparison of the CAB signal and the BOLD response of the second small flickering checkerboard.

Large Flickering Checkerboard

The CAB responses were compared to the BOLD responses, in the same manner as described in section 7.2.4, but applied to the BOLD and CAB experiments using the large flickering checkerboard. The PBR and CAB corresponded very well, but there wasn't enough overlap between the NBR and CAB to compare the two (total of 21 and 20 voxels for the first and second experiments, respectively).

Figure 16 shows the comparison between the CAB and first BOLD experiments. The positive cluster in the second quadrant has (CAB, BOLD) means of (-4.09%, 1.15%). Figure 17 has similar results, with (CAB, BOLD) means of (-4.09%, 1.10%).

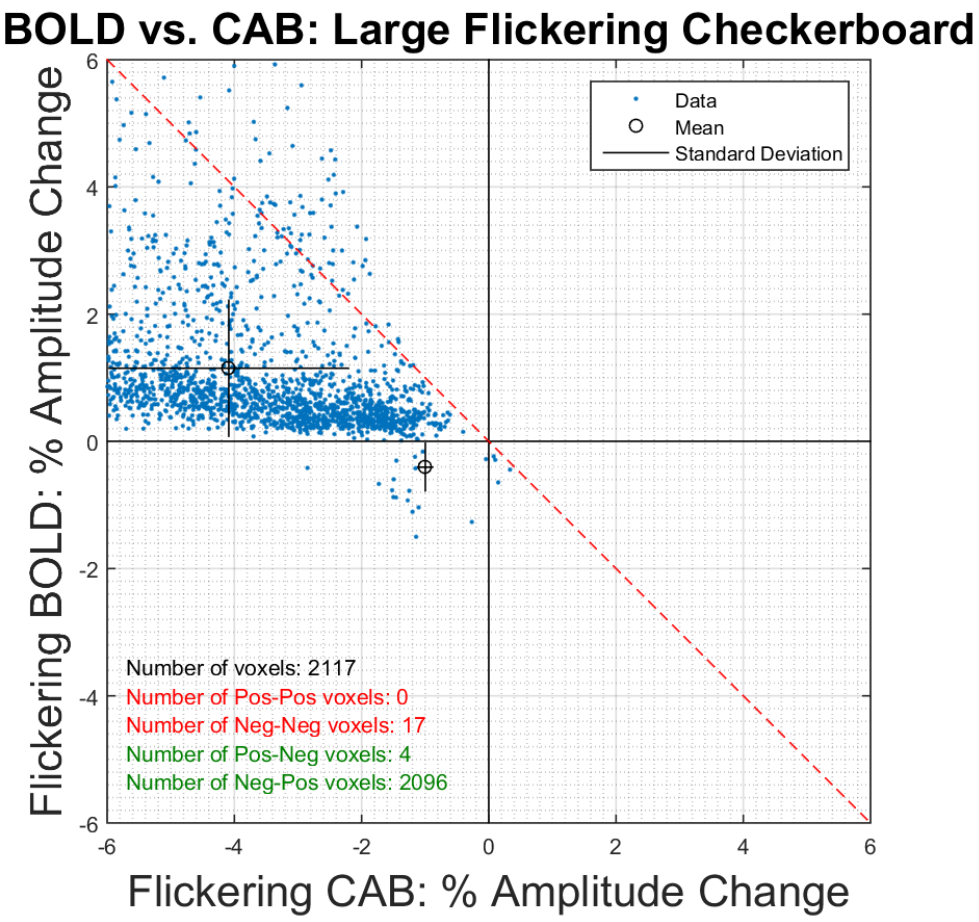

Figure 16. Comparison of the CAB signal and the BOLD response of the first large flickering checkerboard.

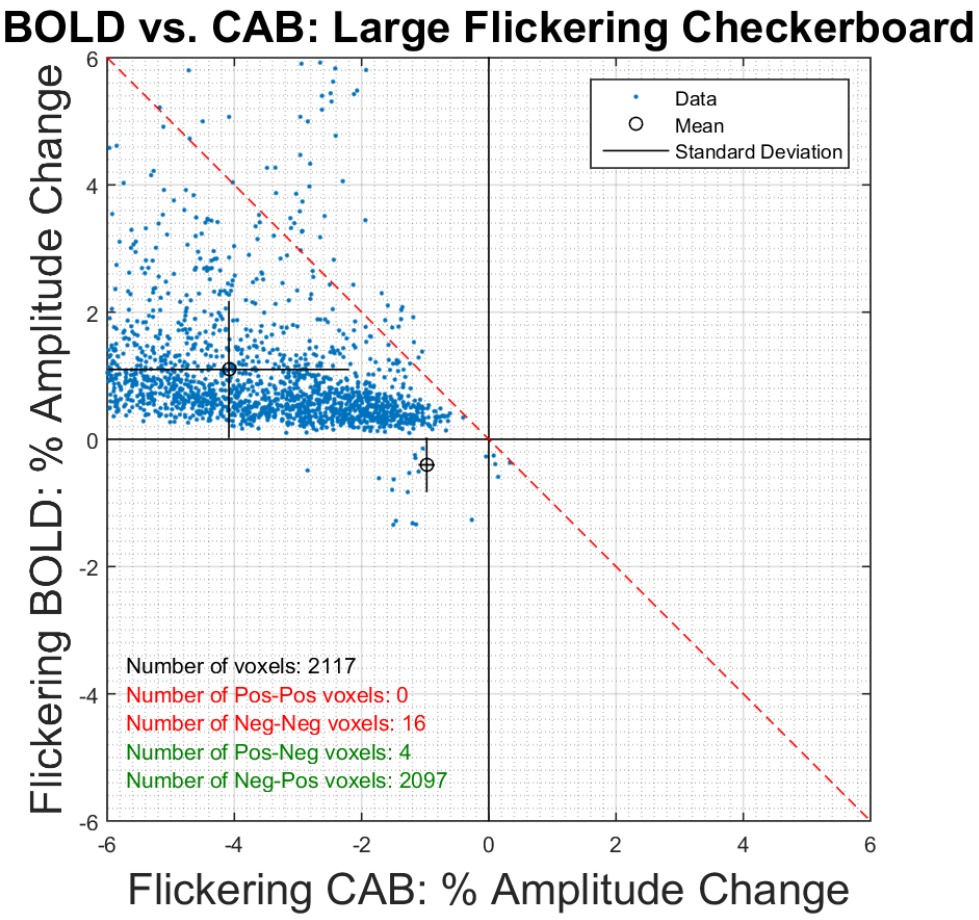

Figure 17. Comparison of the CAB signal and the BOLD response of the second large flickering checkerboard.

7.3 Rotating Checkerboard

One goal of this study is addressed in this section, which was to compare the PBR and NBR to the CAB signal (CBV response). Acquiring the data for the rotating checkerboards was also necessary for the next section, which compares the responses to flickering and rotating checkerboards. The BOLD-CAB comparison is done in the same manner as with the flickering checkerboard (section 7.2), except that the BOLD responses to rotating checkers were done in one session per stimulus (one day for the small stimulus and another day for the large stimulus). In other words, we did not test the reproducibility of the response to rotating checkers over two different sessions, as we did for flickering checkers.

7.3.1 **Activation Maps**

The information presented in Figure 18 is presented in the same manner as Figure 8, and the

results are similar. Refer to section 7.2.1 for a more detailed explanation. The small stimulus produces a PBR in the lateral parts of the occipital cortex, which is the expected retinotopic location [97, 98]. The NBR is around the midline, consistent with literature [69, 75]. The CAB negative response (CBV increase) matches the location of the PBR, and the CAB increase (CBV decrease) matches the location of the NBR.

The large stimulus produced complementary results for the PBR and CAB decrease (CBV increase), with both of these located around the midline. The NBR was spread across small clusters that were retinotopically consistent (lateral). There is a CAB increase (CBV decrease) in the left hemisphere, but the overlap between the NBR and CAB increase was limited.

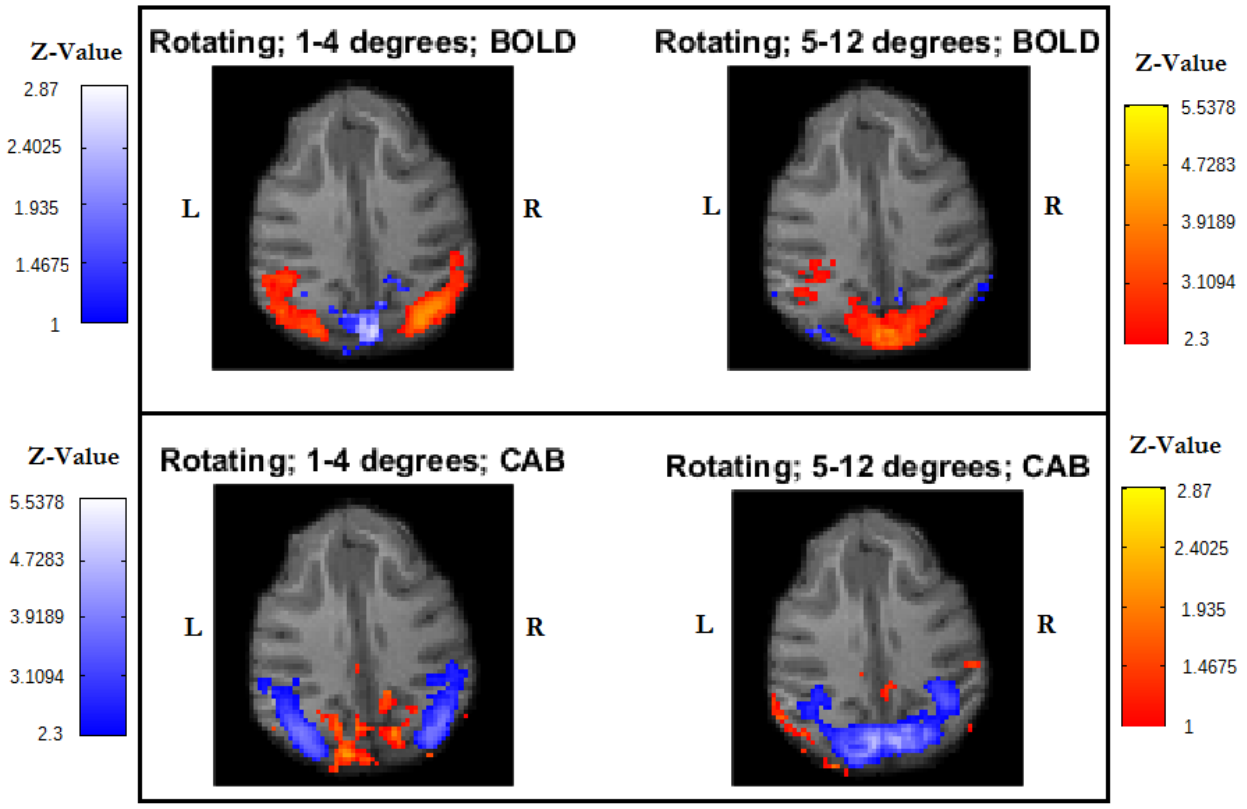

Figure 18. Activation maps (significant Z-values) for rotating stimuli.
Activation maps for the small (left column) and large (right column) checkerboards, for both BOLD (top box) and CAB (bottom box). All results were obtained from different days. Hot colours show areas that had a significant signal increase, cold colours show areas that gave a significant signal decrease.

7.3.2 **Timecourses**

The following figures show the timecourses for the most significant cluster of each activation map. For the case of multiple significant clusters, only the two most significant clusters are displayed. The fitted model for each cluster is superimposed.

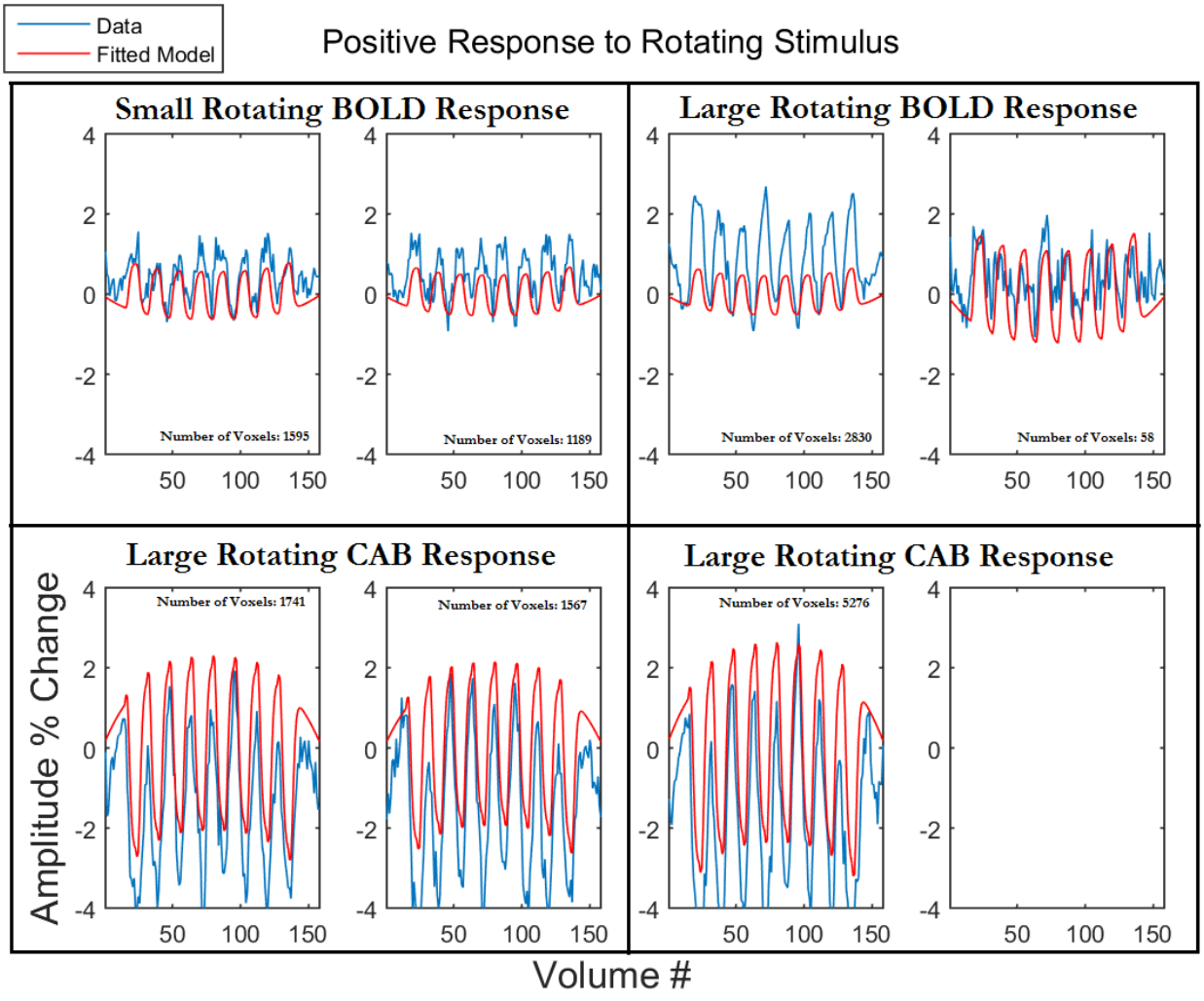

Figure 19. Timecourses for the positive response of the rotating stimuli. Timecourses were averaged over all voxels, separately for each of the two most significant positive clusters. The most significant cluster is on the left, second-most on the right. The timecourses are in blue, the fitted model is in red. The timecourses match their models for all conditions. The large rotating CAB response had only a single cluster.

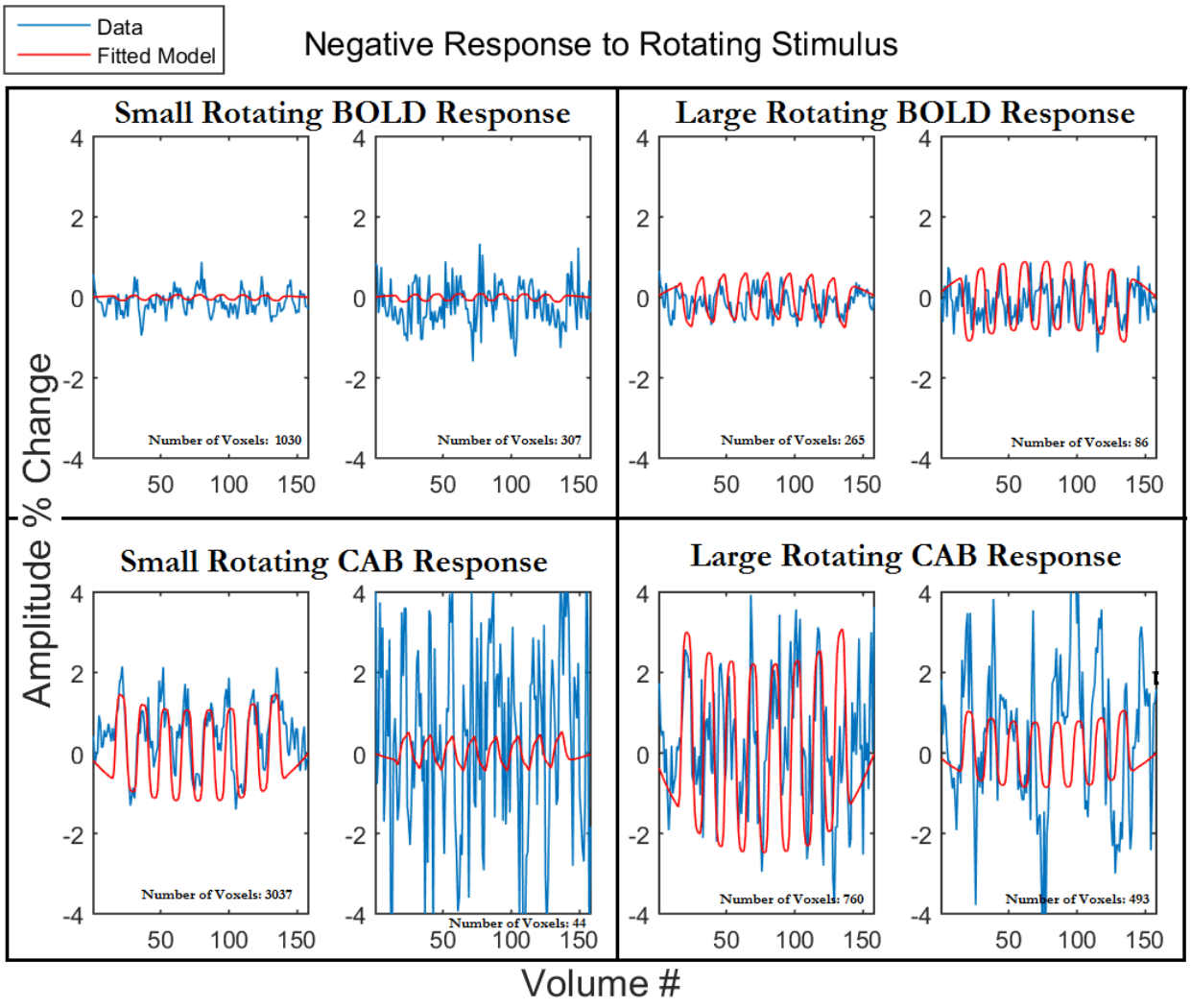

Figure 20. Timecourses for the negative response of the rotating stimuli. Timecourses were averaged over all voxels, separately for each of the two most significant negative clusters. The most significant cluster is on the left, second-most on the right. The timecourses are in blue, the fitted model is in red.

7.3.3 **Peristimulus time-courses**

To get an idea of the shape of the response to each stimulation period, we can produce peristimulus plots for each experiment. For each of the plots in Figures 19 and 20, the period immediately following the start of the stimulus was averaged. Sixteen time points were taken, starting from the two volumes preceding the stimulus. Every experiment had eight of these blocks, and they were averaged together to produce the peristimulus plots. Only the two most significant clusters are plotted (left most significant, right second-most). Plots without a positive response indicate that there was only a single positive response significant cluster.

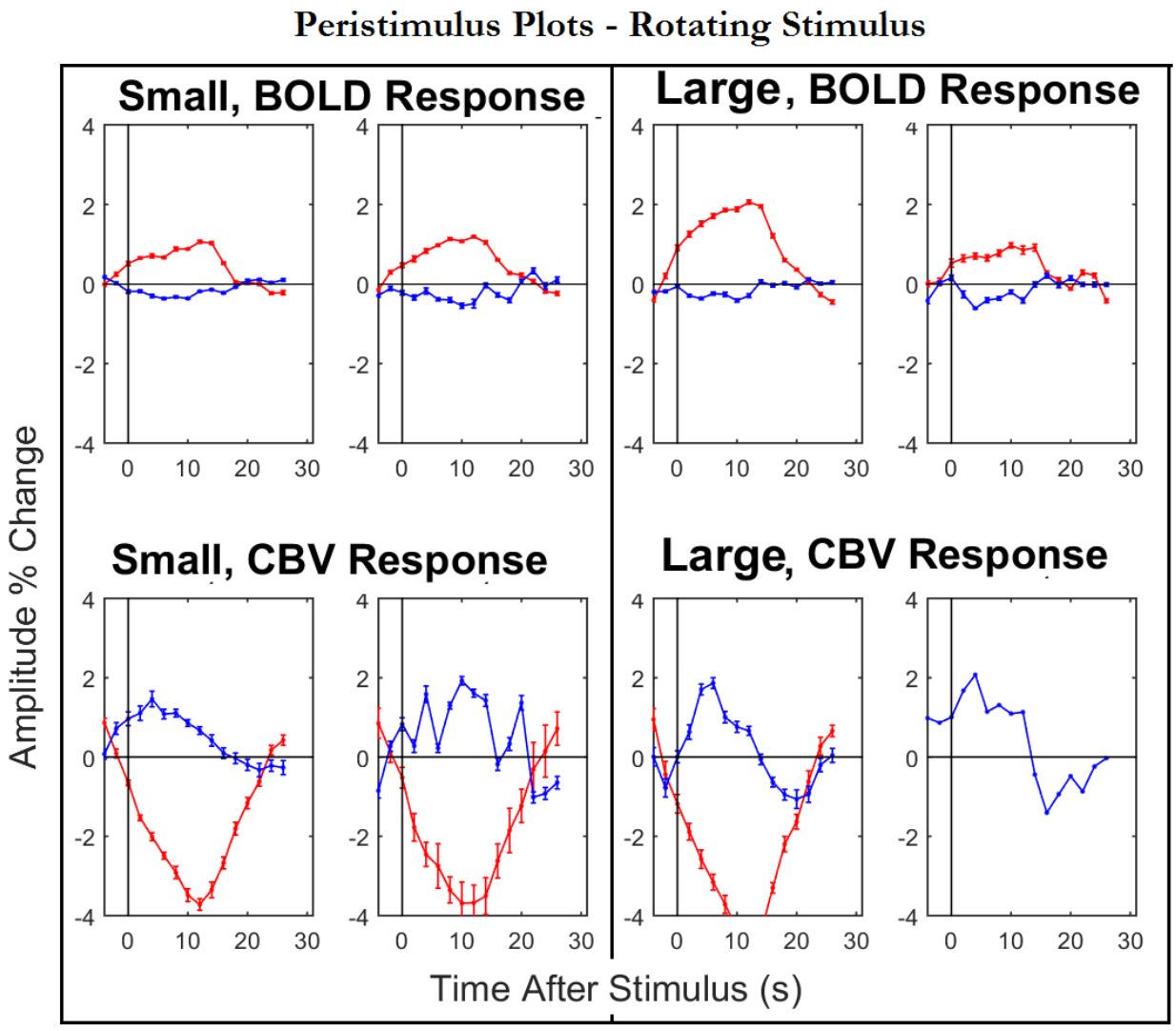

Figure 21. Peristimulus plots for all rotating stimuli.

7.3.4 **BOLD & CBV Relationship**

The main interest of this study is to compare the PBR and NBR to the corresponding CBV response. A mask was created that contained voxels that were significant in both a BOLD experiment and the CBV experiment. For each experiment, the percent change in amplitude relative to baseline was computed. The results for the BOLD signal were then plotted against those of the CAB signal.

Figures 22 and 23 show the BOLD-CAB relationship for two sizes of the rotating checkerboard. The smaller checkerboard (Figure 22) has a clear relationship: voxels with a NBR have an increased CAB signal (decreased CBV), while voxels with a PBR have a decrease in the CAB signal (increased CBV). The large checkerboard (Figure 23), doesn't show such a clear relationship. Voxels with a NBR seem to have no preference for either an increase or decrease in CAB signal, and there are a few PBR voxels that show a decrease in CBV. The mean (circle) and the standard deviation (lines) over all voxels for both experiments are displayed on each plot. The statistics related to the amplitude changes are included at the end of the results section, in Table 7.

Small Rotating Checkerboard

The CAB responses were compared to the BOLD responses, in the same manner as described in section 7.2.4, but applied to the BOLD and CAB experiments using the small rotating checkerboard. Figure 22 shows a good correspondence between the PBR and the CAB decrease (CBV increase), shown in the second quadrant (1641 voxels). The NBR fits well with the CAB increase (CBV decrease), shown in the fourth quadrant (454 voxels). Both clusters were very significant ($p<0.01$). For Figure 22, the positive cluster in the second quadrant had (CAB, BOLD) means of (-2.15%, 0.73%), and the negative cluster in the fourth quadrant had (CAB, BOLD) means of (0.96%, -0.29%).

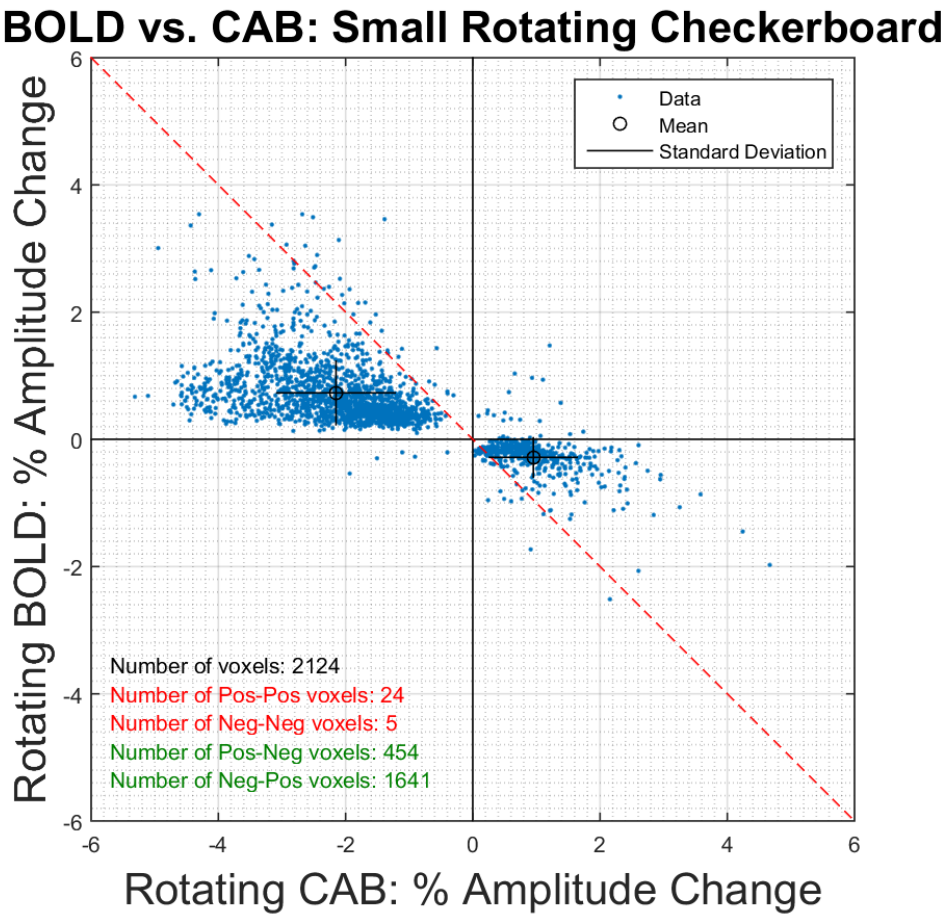

Figure 22. Comparison of the CAB signal and the BOLD response of the small rotating checkerboard.

Large Rotating Checkerboard

The CAB responses were compared to the BOLD responses, in the same manner as described in section 7.2.4, but applied to the BOLD and CAB experiments using the large rotating checkerboard. Figure 23 shows a good correspondence between the PBR and the CAB decrease (CBV increase), shown in the second quadrant (2040 voxels). The NBR fits poorly with the CAB increase (CBV decrease), shown in the fourth quadrant (34 voxels), which is likely due to the detected responses not overlapping. Only the positive cluster was significant ($p<0.01$). For Figure 23, the positive cluster in the second quadrant had (CAB, BOLD) means of (-3.83%, 1.13%). The negative cluster failed to reach significance.

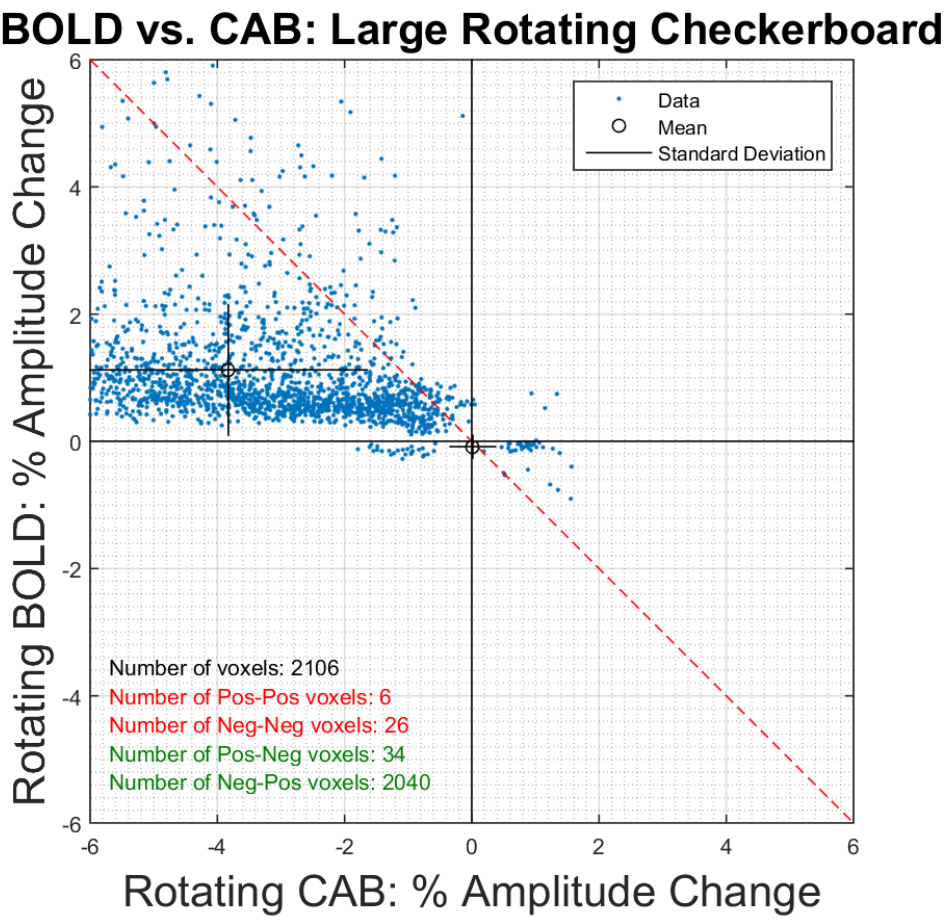

Figure 23. Comparison of the CAB signal and the BOLD response of the large rotating checkerboard.

7.4 Flickering vs. Rotating Checkerboard

One goal of this study is addressed in this section, which was to compare the PBR, NBR, and CBV responses between flickering and rotating checkerboards. All comparisons in this section are done in the same manner as described in section 7.2, but applied to the conditions of this section.

7.4.1 **BOLD**

Figures 24 and 25 show the relationship between the BOLD responses of the small rotating and flickering checkerboards. The small checkerboards have a good amount of overlap for both PBR and NBR voxels, and show that the magnitude of PBR for the rotating checkerboard is slightly higher than for the flickering checkerboard. The magnitude of the NBR for the rotating checkboard is also slightly greater than for the flickering checkerboard.

Figures 26 and 27 show the relationship between the BOLD responses for the large rotating and flickering checkerboards. The overlap between these two BOLD responses (60 voxels) is greater than the overlap between the BOLD and CAB signal (< 30 voxels) for the same stimulus. The magnitude of the PBR for the rotating checkerboard was once again slightly greater than the PBR for the flickering checkerboard. The magnitude of the NBR for the rotating checkerboard was also greater than for the flickering checkerboard. The mean (circle) and the standard deviation (lines) for the positive and negative clusters for both experiments are displayed on each plot. The statistics related to the amplitude changes are included at the end of the results section, in Table 7.

Small Stimulus

The results shown in figures 24 and 25 show that the small checkerboard produces a similar response whether it is flickering or rotating, but with a statistically-significant difference in amplitude. The rotating checkerboard had a greater magnitude for both PBR and NBR. Both figures 24 and 25 show a good correspondence between both the PBR and NBR across stimuli. All clusters were very significant ($p<0.01$).

For Figure 24, the positive cluster had (Rotating, Flickering) means of (0.99%, 0.8%). The negative cluster had (Rotating, Flickering) means of (-0.41%, -0.32%).

For Figure 25, the positive cluster had (Rotating, Flickering) means of (0.99%, 0.79%). The

negative cluster had (Rotating, Flickering) means of (-0.41%, -0.34%).

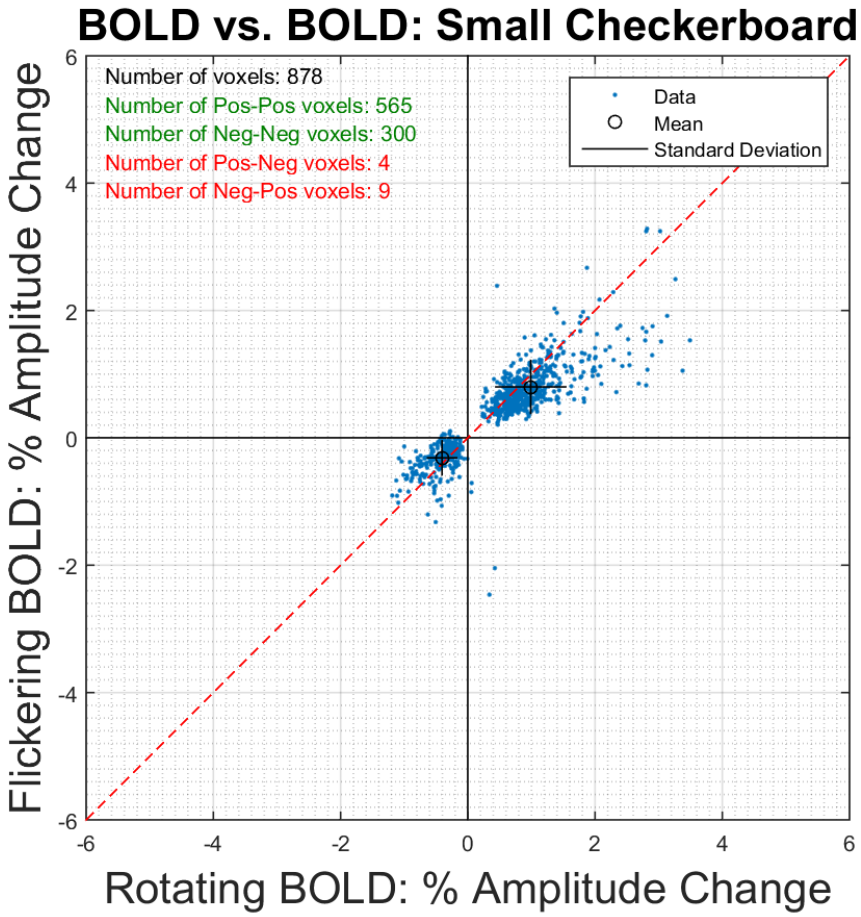

Figure 24. Comparison of the changes in the BOLD signal amplitude between the small rotating and first small flickering checkerboard.

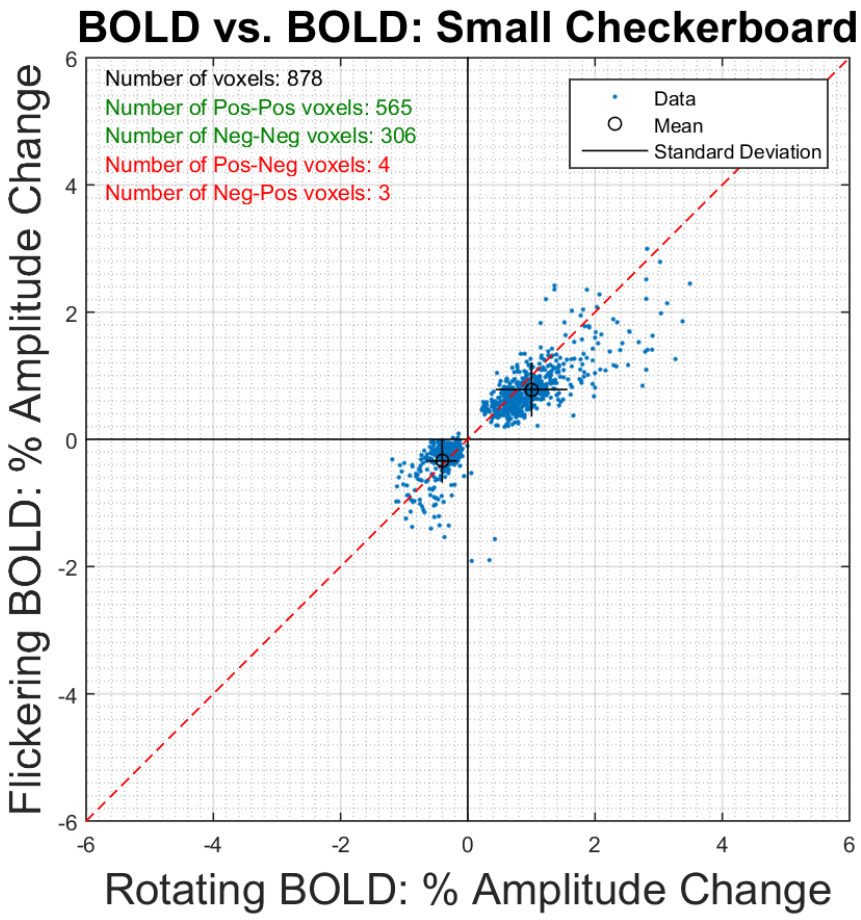

Figure 25. Comparison of the changes in the BOLD signal amplitude between the small rotating and second small flickering checkerboard.

Large Stimulus

The results shown in figures 26 and 27 show that the large checkerboard produces similar responses for both flickering and rotating checkerboards. There were statistically-significant differences in BOLD responses across stimulus types. The large rotating checkerboard had a greater PBR magnitude, but a smaller NBR magnitude. All clusters were significant ($p<0.01$).

For Figure 26, the positive cluster had (Rotating, Flickering) means of (1.55%, 1.39%). The negative cluster had (Rotating, Flickering) means of (-0.34%, -0.66%).

For Figure 27, the positive cluster had (Rotating, Flickering) means of (1.55%, 1.29%). The negative cluster had (Rotating, Flickering) means of (-0.34%, -0.74%).

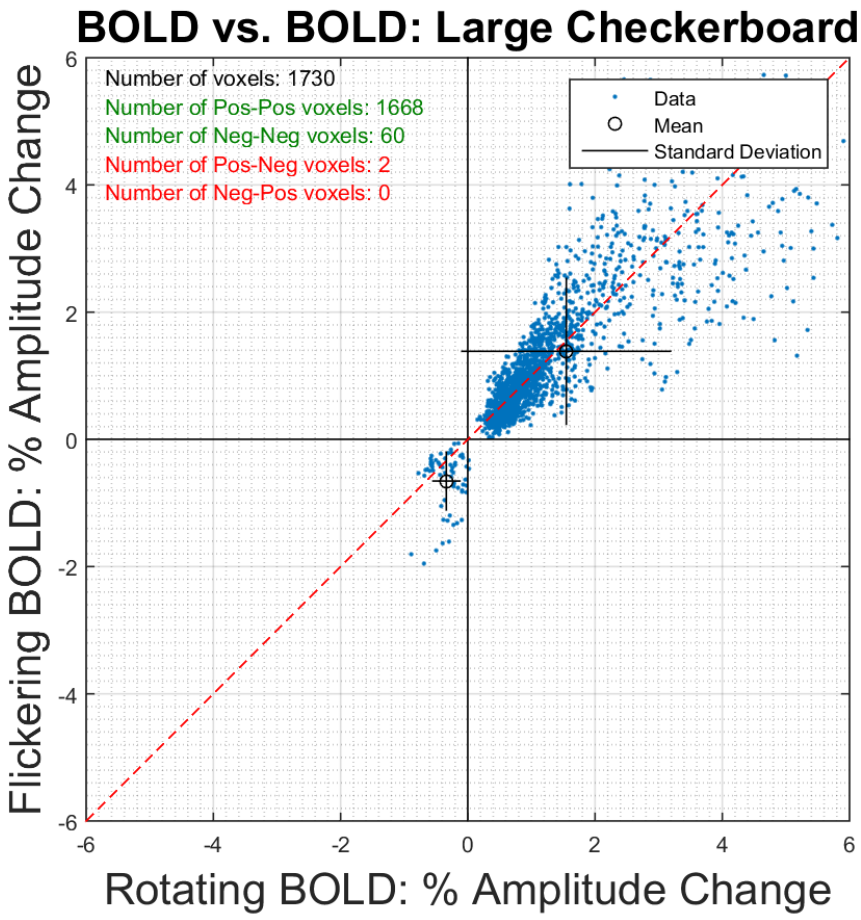

Figure 26. Comparison of the changes in BOLD signal amplitude between the large rotating and the first large rotating checkerboard.

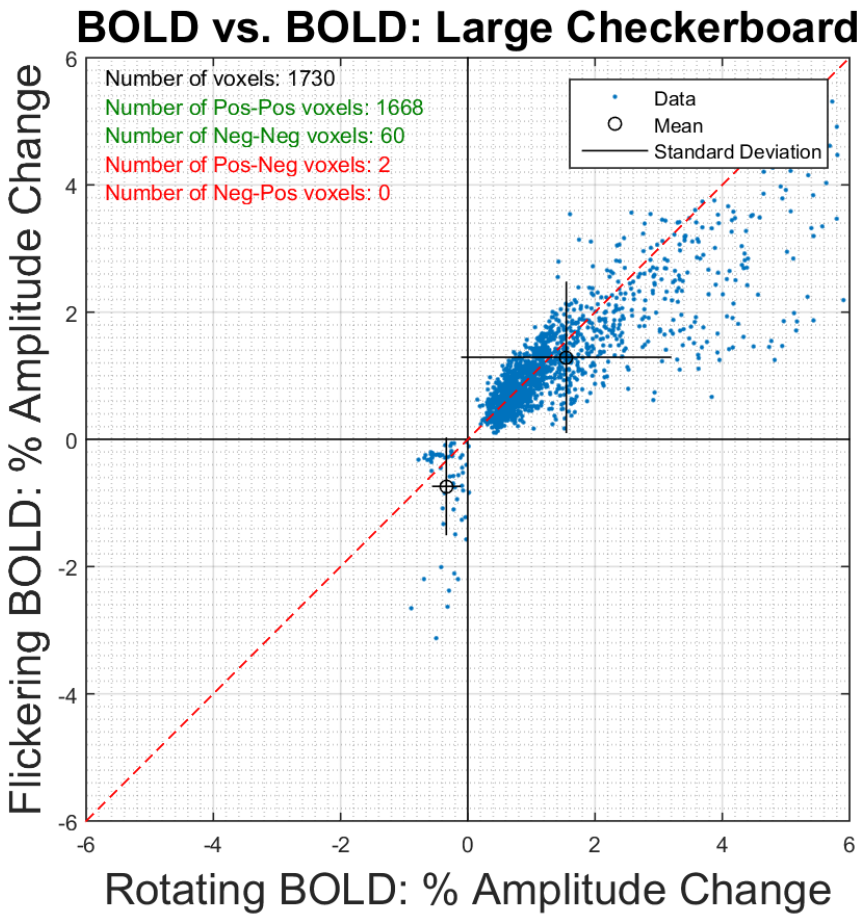

Figure 27. Comparison of the changes in BOLD signal amplitude between the large rotating and the second large rotating checkerboard.

7.4.2 **CAB**

Figure 28 shows the relationship between the CAB signals of the small rotating and flickering checkerboards. The CAB signal shows comparable magnitudes for both flickering and rotating stimuli, and for both positive and negative responses.

Figure 29 shows the relationship between the CAB responses for the large rotating and flickering checkerboards. The magnitude of the CAB decrease (CBV increase) is statistically greater for the flickering stimulus, but the CAB increase (CBV decrease) is statistically greater for the rotating stimulus. The mean (circle) and the standard deviation (lines) for both experiments are displayed on each plot. The statistics related to the amplitude changes are included at the end of the results section, in Table 7.

Small Stimulus

The results shown in Figure 28 show that the small checkerboard produces a similar response whether it is flickering or rotating. Both positive and negative clusters were very significant ($p<0.01$). The positive cluster in the third quadrant had (Rotating, Flickering) means of (-2.33%, -2.35%). The negative cluster in the first quadrant had (Rotating, Flickering) means of (1.16%, 1.19%).

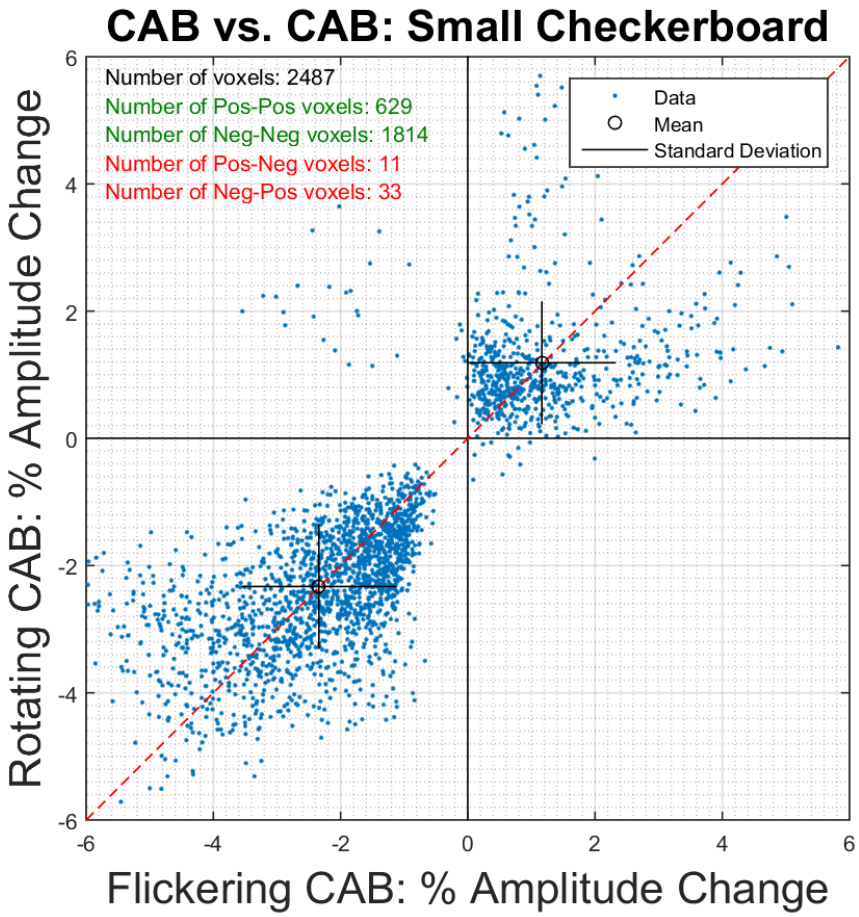

Figure 28.Comparison of the changes in the CAB signal between small rotating and small flickering checkerboard.

Large Stimulus

The results shown in Figure 29 show that the large checkerboard produces a similar response whether it is flickering or rotating, but with statistically significant differences. Both positive and negative clusters were very significant ($p<0.01$). The positive cluster in the third quadrant had (Rotating, Flickering) means of (-2.78%, -3.04%). The negative cluster in the first quadrant had (Rotating, Flickering) means of (1.02%, 0.16%).

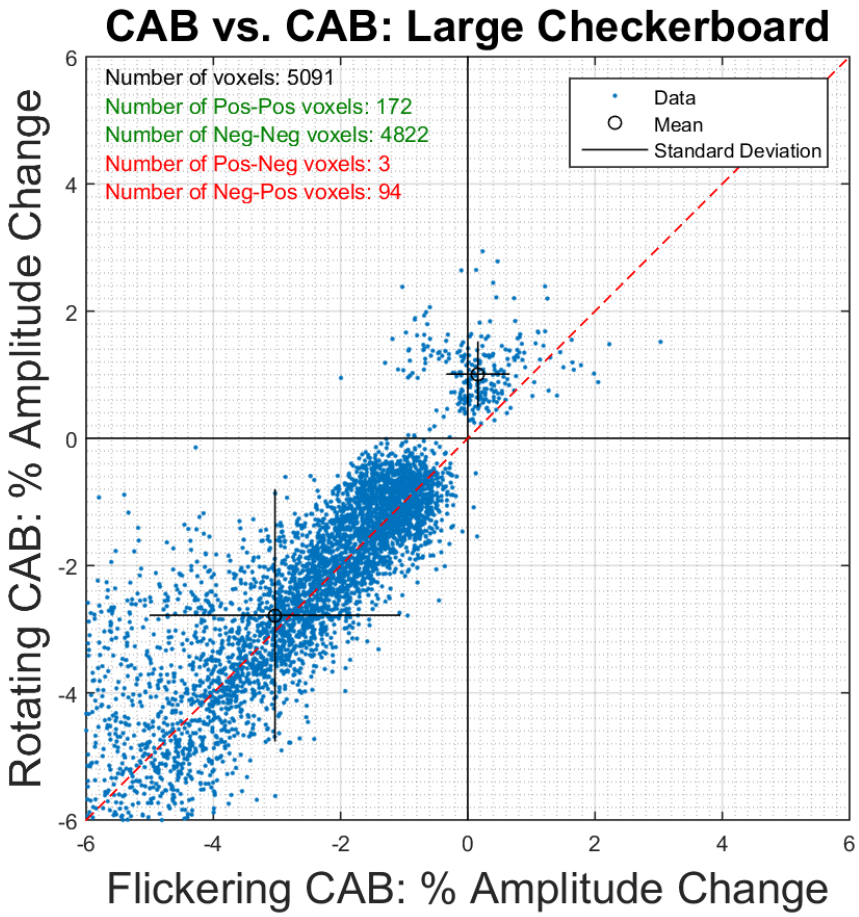

Figure 29. Comparison of the changes in the CAB signal between large rotating and large flickering checkerboard.

7.5 Amplitude Statistics

The following table has statistics for all experiments, along with the corresponding figure. Voxels are grouped together based on the results of the other experiment they are plotted with. That is, if stimulus A is plotted against stimulus B, voxels that were positive for stimulus A are grouped together for stimulus B, and vice versa. "Positive" refers to the sign of the BOLD response and the corresponding CAB in the same area (i.e., decreases in the CAB that occur in regions of the PBR are considered the “positive” response). P-values with asterisks did not meet the condition of $p<0.05$. Entries marked with ‘N/A’ had too few voxels, arbitrarily selected as fewer than 30 voxels.

Table 7. Statistics about the positive and negative responses.

Figure	Experiment	Response	$\log_{10}(p)$	95% Conf. Interval of Mean	Standard Deviation
Figure 12	Small Flick. BOLD (1)	Positive	-198.3	0.75, 0.82	0.46
		Negative	-80.5	-0.37, -0.31	0.35
	Small Flick. BOLD (2)	Positive	-210.5	0.80, 0.87	0.47
		Negative	-54.9	-0.37, -0.30	0.45
Figure 13	Large Flick. BOLD (1)	Positive	-inf	1.16, 1.25	1.08
		Negative	-123.6	-0.95, -0.84	0.58
	Large Flick. BOLD (2)	Positive	-inf	1.08, 1.17	1.09
		Negative	-95.4	-1.01, -0.87	0.78
Figure 14	Small Flick. CAB	Positive	-170.5	-2.54, -2.34	0.98
		Negative	-47.4	0.72, 0.90	0.67
	Small Flick. BOLD (1)	Positive	-182.6	0.74, 0.80	0.38
		Negative	-31.2	-0.38, -0.29	0.30
Figure 15	Small Flick. CAB	Positive	-169.3	-2.54, -2.33	0.67
		Negative	-46.6	0.72, 0.90	0.98
	Small Flick. BOLD (2)	Positive	-186.2	0.69, 0.74	0.34
		Negative	-36.4	-0.37, -0.28	0.27
Figure 16	Large Flick. CAB	Positive	-inf	-4.17, -4.01	0.12
		Negative	N/A	N/A	N/A
	Large Flick. BOLD (1)	Positive	-inf	1.10, 1.20	0.37
		Negative	N/A	N/A	N/A
Figure 17	Large Flick. CAB	Positive	-inf	-4.17, -4.01	0.16
		Negative	N/A	N/A	N/A
	Large Flick. BOLD (2)	Positive	-inf	1.05, 1.15	0.42
		Negative	N/A	N/A	N/A
Figure 22	Small Rot. CAB	Positive	-inf	-2.20, -2.10	0.69
		Negative	-100.5	0.89, 1.02	0.93
	Small Rot.	Positive	-inf	0.71, 0.75	0.31

	BOLD	Negative	-54.0	-0.32, -0.25	050
Figure 23	Large Rot. CAB	Positive	-inf	-3.92, -3.74	0.36
		Negative	-0.04*	-0.26, 0.28	2.18
	Large Rot. BOLD	Positive	-inf	1.08, 1.17	0.18
		Negative	-0.83*	-0.196, 0.031	1.02
Figure 24	Small Rot. BOLD	Positive	-176.1	0.94, 1.04	0.55
		Negative	-90.0	-0.43, -0.38	0.23
	Small Flick. BOLD (1)	Positive	-175.8	0.76, 0.84	0.41
		Negative	-75.6	-0.34, -0.29	0.27
Figure 25	Small Rot. BOLD	Positive	-181.7	0.96, 1.05	0.55
		Negative	-95.5	-0.43, -0.38	0.23
	Small Flick. BOLD (2)	Positive	-173.0	0.75, 0.822	0.41
		Negative	-56.2	-0.37, -0.30	0.33
Figure 26	Large Rot. BOLD	Positive	-232.0	1.47, 1.63	1.64
		Negative	-17.2	-0.39, -0.28	0.21
	Large Flick. BOLD (1)	Positive	-inf	1.33, 1.44	1.15
		Negative	-15.3	-0.77, -0.54	0.45
Figure 27	Large Rot. BOLD	Positive	-232.0	1.47, 1.63	1.64
		Negative	-17.22	-0.39, -0.28	0.21
	Large Flick. BOLD (2)	Positive	-287.0	1.23, 1.35	1.18
		Negative	-9.4	-0.94, -0.54	0.76
Figure 28	Small Flick. CAB	Positive	-inf	-2.40, -2.29	1.20
		Negative	-82.9	1.06, 1.26	1.15
	Small Rot. CAB	Positive	-inf	-2.38, -2.28	0.96
		Negative	-129.9	1.11, 1.26	0.95
Figure 29	Large Flick. CAB	Positive	-inf	-3.09, -2.98	1.96
		Negative	-4.3	0.08, 0.24	0.49
	Large Rot. CAB	Positive	-inf	-2.84, -2.72	1.97
		Negative	-56.4	0.93, 1.11	0.50

8 Discussion

This study had multiple goals. First, we wanted to establish a platform for performing fMRI experiments with NHP, perform CBV measurements, and verify the results. Second, we wanted to test the reproducibility of both the PBR and the NBR in an alert NHP. Third, we wanted to investigate the neurovascular coupling between the PBR, NBR, and CAB signals. Fourth, using the PBR, NBR, and CAB results, we wanted to test whether the discrepancy between NHP and human results were primarily due to anesthesia or a species difference. Last, we wanted to investigate differences in the magnitude of the response to flickering and rotating checkerboards, as previously reported.

8.1 BOLD and CAB Responses

8.1.1 PBR and CAB fMRI response

The relationship between the PBR and CBV is well-known [99], and is intuitive given the underlying physiological causes of the BOLD signal. The regional increase in CBF is associated with an increase in CBV. The CBF change is what causes the BOLD signal to increase, and the CBV changes accommodate the increased amount of blood being passed through blood vessels. For this study to be the least bit credible, it is important that our experiments are able to reproduce this effect.

All of our results that compared the CAB and BOLD signals (figures 14-17, 22, 23) were consistent: when voxels displayed a PBR, there was a statistically significant decrease in the CAB signal (Table 7), indicating an increase in CBV. To show this, we can look at four conditions where the CAB is compared to the PBR: small or large, flickering or rotating. Taking only voxels which showed a PBR in the BOLD experiment, we can see how they responded in the CBV-weighted experiment.

Table 8. Summary of amplitude changes for CAB associated with the PBR.

Stimulus Type	95% Confidence for CAB % change (associated with PBR)
Small Flickering CAB	-2.54, -2.33
Small Rotating CAB	-2.20, -2.10
Large Flickering CAB	-4.17, -4.01
Large Rotating CAB	-3.92, -3.74

Looking at Table 8, we see that regardless of the size or type of stimulus, all CAB signal changes are significantly negative, as expected. For the small flickering stimulus, the CAB had an expected percent change between -2.54% and -2.33%. The large flickering stimulus gave almost identical intervals, indicating the CAB amplitude change to be between -2.82% and -2.67%. The rotating checkerboards gave smaller responses for both sizes; between -1.17% and -1.09% for the small stimulus, and between -2.10% and -2.14% for the large stimulus.

Overall, these results indicate that there is a reproducible CAB decrease (CBV increase) that is associated with the PBR, consistent with literature [1, 2]. This result is not new, but achieves one of our goals. Namely, it confirms that our platform for performing fMRI and CBV measurements in alert macaques is able to reproduce results extant in the literature.

8.1.2 **NBR and CAB**

The comparison of the NBR and the CAB was the main goal of this thesis. Previous work reported on the neurovascular coupling in the barrel cortex of anesthetized rats using optical imaging [100] and showed that the NBR was mainly associated with decreases in CBV and an increase in HbR. Work in the primary visual cortex of anesthetized cats showed similar results [70], showing a CBV-weighted (MION) signal change of about 1% in areas of the NBR. Recent work in humans [2] reported a CBV decrease of around 7%. The same paper mentions that the experiment was repeated in anesthetized macaques, but found a CBV *increase* in V1, consistent with their previous work [1] in macaques, but contradictory with their results in humans.

In this study, our results show that alert macaques show the same negative CBV response associated with the NBR when small stimuli were used, but produced inconclusive results with the large stimuli.

Table 9. Summary of amplitude changes for CAB associated with the NBR.

Stimulus Type	95% Confidence for CAB % change (Negative)
Small Flickering CAB	0.72, 0.90
Small Rotating CAB	0.89, 1.02
Large Flickering CAB	Too few voxels (< 30)
Large Rotating CAB	-0.26, 0.28

As can be seen in Table 9, the small stimuli produced significantly-positive changes in the CAB signal, indicating a decrease in CBV. The large stimuli produced either too few voxels or a CAB amplitude that was not significantly different from zero. An important thing to consider is the voxel overlap in our data. Whereas the small stimuli produced an NBR located along the midline of the occipital lobe, the large stimuli produce an NBR in the lateral parts of the visual cortex. The NBR for the flickering stimulus is clearly visible (Figure 8), but the CAB signal is only significant on the opposite side. Given that the stimulus is symmetric, the asymmetry in the response is possibly due to a difference in experimental setup, such as the placement of surface coils. Nonetheless, the asymmetry causes very few voxels NBR voxels to overlap, leading to a poor representation of the association between the NBR and the CAB signal.

Lowering significance threshold reveals a CAB increase (CBV decrease) that overlaps with the NBR cluster. This indicates that the issue is more one of SNR and CNR than it is a systematic one. The same applies to the large rotating stimulus, though for the large stimulus the NBR is not as strong as with the flickering.

Of note, large ring stimuli produce low amplitude NBR in central visual field regions of human lower visual areas too [69]. One possibility that may underlie this phenomenon is the continuous attention that the subjects have to pay to the fixation spot. Such attention is known to increase both neurophysiological activity and BOLD signal. Thus, the persistent attention and corresponding increase in neuronal activity and BOLD signal possibly counter any NBR that does appear under these conditions in anesthetized primates [75].

8.1.3 **CBV to CAB**

An important point to note is that the reported changes are in the CAB signal, not the CBV. Although the CAB signal is proportional to changes in CBV, it is not a direct representation of it. The CAB signal contains contamination from changes in CBF and $CMRO_2$, and deriving a measure for the CBV would require using a method such as suggested by Kennan et al. [101]. The method works by comparing the changes in relaxation constants (R_2^*, or equivalently T_2^*) in an experiment before and after a contrast agent is injected, as well as before and during activation in both cases. By comparing the constants before and during activation, we can measure the relative contribution of CBV changes to the changes in R_2^*. Applying this method to

NHPs is difficult, and not necessarily reliable. Using our current experimental setup, the NHP is secured via a headpost and RF coils are placed around its head. During a scan, the NHP is positioned to face forward in a sphinx position[12]. Injecting a contrast agent involves placing the NHP's chair upright, lifting up part of the panels, and injecting the contrast. Getting the necessary data for the method would require us to remove the NHP from the MRI room, remove the headpost and coils, inject the contrast agent, and then replace everything before returning to the scanner. Although this is certainly possible, our immediate goal was to detect whether a change could be detected at all. Given that NHPs remain cooperative for a limited time (in our case about 50-60 minutes, optimistically), the extra steps would have heavily reduced the number of complete datasets we could acquire without necessarily addressing the question of interest. Now that CBV decreases have been detected in alert macaques, future work can focus on optimizing its quantification.

Another point to consider is the origin of the BOLD and CAB signals, which may also account for the non-perfect overlap. The BOLD signal originates predominantly from large veins [102], since veins are where the largest change in oxygenation occurs. Further, the BOLD signal can be located downstream from the activated area [62], whereas the CAB signal is more spatially specific to the site of changes in neuronal activity [103].

8.2 Flickering vs. Rotating Stimuli

8.2.1 **PBR & NBR**

One of the goals of this study was to compare the responses of flickering and rotating checkerboards. Figures 24-27 show that both stimulus types have a similar PBR and NBR, quantified in Table 7. A difference in the amplitude of the NBR to rotating stimuli is consistent with existing literature [2], suggesting that the difference in activation between flickering and rotating checkerboards could be caused by the difference in stimuli.

Table 10. Summary of amplitude changes for BOLD responses; comparison of flickering and rotating checkerboards.

Stimulus Type	Response Type	95% Confidence for BOLD % change.
Small Flickering BOLD	Positive	0.76, 0.84 (1st exp.) 0.75, 0.82 (2nd exp.)

[12] See [113], figure 2.

	Negative	-0.34, -0.29 (1st exp.) -0.37, -0.30 (2nd exp.)
Small Rotating BOLD	Positive	0.96, 1.05
	Negative	-0.43, -0.38
Large Flickering BOLD	Positive	1.33, 1.44 (1st exp.) 1.23, 1.35 (2nd exp.)
	Negative	-0.77, -0.54 (1st exp.) -0.94, -0.54 (2nd exp.)
Large Rotating BOLD	Positive	1.47, 1.63
	Negative	-0.39, -0.28

As we can see from Table 10, the small rotating checkerboard has a larger response magnitude than the small flickering checkerboard for both the PBR and the NBR. For the large stimulus, the rotating checkerboard had a larger PBR, but a smaller NBR. The smaller NBR for the large rotating checkerboard is consistent with [2], which reported a smaller number of significant voxels in the NBR for a similar rotating checkerboard.

Overall, our results show that rotating checkerboards do elicit NBR in alert primates, just as they did in anesthetized primates. It is possible that the discrepancy between the NBR elicited in our alert primate experiments by rotating checkers, and the lack of such response in Huber's experiments is caused by a difference in temporal frequency of the rotation. Huber and colleagues rotated their stimulus at a rate of 120º/sec, compared to 60º/sec in our experiment. We expect that our stimulus engages more higher visual areas than the fast rotating stimulus used by Huber and colleagues. Thus, a more potent suppression can be applied by these higher visual areas in response to our rotating checkers compared to Huber's, explaining the difference in the magnitudes of the NBR.

8.2.2 **CAB**

To further examine the differences between the rotating and flickering checkerboards, we also examined the differences in the CAB responses, summarized in the table below.

Table 11. Summary of amplitude changes for CAB response; comparison of flickering and rotating checkerboards.

Stimulus Type	Response Type	95% Confidence for CAB % change
Small Flickering CAB	Positive	-2.40, -2.29
	Negative	1.06, 1.26
Small Rotating CAB	Positive	-2.38, -2.28
	Negative	1.11, 1.26
Large Flickering CAB	Positive	-3.09, -2.98
	Negative	0.08, 0.24
Large Rotating CAB	Positive	-2.84, -2.72
	Negative	0.93, 1.11

Table 11 shows that the small stimuli produce almost identical amplitude changes for rotating and flickering checkers, despite the difference seen for BOLD. The large stimuli have slightly different amplitudes for the CAB responses. The flickering checkerboard has a larger CAB decrease (CBV increase) associated with the PBR, but the rotating checkerboard has a much greater CAB increase (CBV decrease) associated with the NBR.

The CAB differences in the small stimulus are not necessarily contradictory with the BOLD differences reported in section 8.2.1. The BOLD signal is proportional to the CBF and inversely proportional to the CBV and $CMRO_2$. Given that the CAB response is comparable between the small flickering and rotating checkerboards, we can hypothesize that the differences in the PBR are due to a larger CBF or a smaller $CMRO_2$ in the rotating checkerboard relative to the flickering checkerboard. More simply: either the rotating checkerboard has a greater CBF response relative to the flickering checkerboard, or it has a smaller $CMRO_2$.

The CAB differences between flickering and rotating checkers in the large stimuli are consistent, but it may not be immediately apparent. Looking at the CAB signal associated with the PBR, we see that the flickering stimulus has a larger magnitude. That is, the CBV increases more for the flickering stimulus. Since the BOLD signal is inversely proportional to the CBV, the flickering checkerboard has a smaller PBR. For the CAB signal associated with the NBR, the rotating checkerboard has a much greater CAB increase (CBV decrease), increasing the BOLD signal and making it less negative. The large flickering checkerboard has a greater CAB decrease (CBV increase) in PBR regions, resulting in a reduced BOLD signal. Similarly, the large flickering checkerboard has a very small CAB increase (CBV decrease) associated with the NBR regions, resulting in a larger BOLD

8.3 Differences with Previous Work

The statistics provided in Table 7 are consistent with previous reports, showing that the NBR amplitude was between half and a third of the PBR response. The ratio is only slightly smaller than reported in other studies [69, 2]. Data analysis was also slightly different. Other work [1, 2] used predefined ROIs to compare NBR and PBR, whereas our approach was to use significant clusters and compare the overlap between different experiments. Our TE was also slightly different; whereas [1] used identical TE across BOLD and CBV measurements our CAB signal was obtained using a much shorter TE than our BOLD data, which reduces the amount of BOLD contamination in the CAB signal [2].

8.4 Neuronal Correlates

Given the neural correlates reported by Logothetis et al. [104] for the PBR and by Shmuel et al. [75] for the NBR, we interpret our results to mean increased neural activity where the PBR is present, and reduced activity for areas where the NBR is present. Our results (decreased CBV associated with NBR) are consistent with previous results in alert human subjects showing negative CBF response associated with NBR [69]. To date, all studies that examined the relationship between CBF responses and neurophysiological activity have found that they matched well. Therefore, the decreased CBV that we observed, which has to be associated with decreased CBF, indirectly indicates that the NBR is associated with decreased neuronal activity. These results are consistent with a receptive field model that accounts for surround-suppression [105, 106], which reduces neuronal activity when a stimulus is presented in an area around its receptive field.

8.5 Methodological Considerations

The use of the injected contrast agent, feraheme, should be considered. Repeated injections led to a significant T_2^* signal drop around the occipital midline, even several days after the previous injection. The signal drop was not present in T_1 images, indicating that the drop is either due to susceptibility or inhomogeneity differences. Based on feraheme's reported accumulation in tissue [107], we expect it to be the cause of the signal drop. We note that this would not affect the CAB responses that we report here.

9 Conclusion

Our study was able to accomplish its goals. A platform was established for training NHPs, acquiring alert fMRI data, and a protocol for injecting MRI contrast was completed. The reproducibility of both the PBR and the NBR in an alert macaque was demonstrated. We were able to reproduce the known coupling between the PBR and the CBV for all stimuli. The NBR was quantitatively associated with a decrease in CBV for the small stimuli. Large stimuli produced only small areas of activation for both the NBR and decreases in CBV. Although these regions were nearby, they either contained too few voxels or weren't significant enough. Comparing our study to previous results [1, 2], our results with the NBR and CBV are consistent with Huber et al.'s experiment in alert humans. In contrast, Goense et al. found that the CBV increased in anesthetized macaques, which was a blatant contradiction. The difference could have been accounted for by differences in alertness, species, or posture. Our results show that anesthesia is the most probable cause of the difference, but this can't be stated conclusively until similar acquisitions with anesthetized macaques are performed to account for possible differences caused by the scanner, pulse sequences, contrasts, etc.

Our final goal was to compare the response to flickering and rotating checkerboards. Oddly, the small rotating checkerboard had a larger amplitude for both the PBR and NBR, but the large rotating checkerboard had a larger amplitude for the PBR but a smaller amplitude for the NBR. These results were not contradicted by the CAB response to the small stimulus, and were consistent with the CAB response for the large stimulus. Overall, our results show that rotating checkerboards do elicit NBR in alert primates, just as they did in anesthetized primates. It is possible that the discrepancy between the NBR elicited in our alert primate experiments by rotating checkers, and the lack of such response in Huber's experiments is caused by a difference in temporal frequency of the rotational stimulus.

10 References

[1] J. Goense, H. Merkle and N. K. Logothetis, "High-Resolution fMRI Reveals Laminar Differences in Neurovascular Coupling between Positive and Negative BOLD Responses," *Neuron,* vol. 76, pp. 626-639, 2012.

[2] L. Huber, J. Goense, A. J. Kennerley, D. Ivanov, S. N. Krieger, J. Lepsien, R. Trampel, R. Turner and H. E. Moeller, "Investigation of the neurovascular coupling in positive and negative BOLD responses in human brain at 7T," *Neuron,* vol. 97, pp. 349-362, 2014.

[3] S. S. Kannurpatti and B. B. Biswal, "Effect of anesthesia on CBF, MAP, and fMRI-BOLD signal in response to apnea," *Brain Research,* vol. 1011, no. 2, pp. 141-147, 2004.

[4] D. P. Aksenov, L. Li, M. J. Miller, G. Iordanescu and A. M. Wyrwicz, "Effects of anesthesia on BOLD signal and neuronal activity in the somatosensory cortex," *Journal of Cerebral Blood Flow & Metabolism,* 2015.

[5] S. A. Huettel, A. W. Song and G. McCarthy, Functional Magnetic Resonance Imaging, Sinauer Associates, 2008.

[6] E. M. Haacke, R. W. Brown, M. R. Thompson and R. Venkatesan, Magnetic Resonance Imaging: Physical Principles and Sequence Design, Wiley-Liss, 1999.

[7] R. B. Moon and J. H. Richards, "Determination of Intracellular pH by 31P Magnetic Resonance," *The Journal of Biological Chemistry,* vol. 248, no. 20, pp. 7276-7278, 1973.

[8] N. Iriguchi and J. Hasegawa, "Carbon-13 magnetic resonance imaging of a human arm," *Magnetic Resonance Imaging,* vol. 11, no. 2, pp. 269-271, 1993.

[9] S. Ogawa, T. M. Lee, A. R. Kay and D. W. Tank, "Brain magnetic resonance imaging with contrast dependent on blood oxygenation," *Proceedings of the National Academy of Sciences,* vol. 87, pp. 9868-9872, 1990.

[10] E. Kandel, J. Schwartz and T. Jessell, Principles of Neural Science, 4th ed., McGraw-Hill Medical, 2000.

[11] M. E. Raichle, R. L. Grubb, M. H. Gado, J. O. Eichling and M. M. Ter-Pogossian, "Correlation Between Regional Cerebral Blood Flow and Oxidative Metabolism," *Archives of Neurology,* pp. 523-526, 1976.

[12] P. T. Fox and M. E. Raichle, "Focal physiological uncoupling of cerebral blood flow and oxidative metabolism during somatosensory stimulation in human subjects," *Proceedings of the National Academy of Sciences,* vol. 83, no. 4, pp. 1140-1144, 1986.

[13] R. L. Grubb, M. E. Raichle, C. S. Higgins and J. O. Eichling, "Measurement of Regional Cerebral Blood Volume by Emission Tomography," *Annals of Neurology,* vol. 4, pp. 322-328, 1978.

[14] D. Attwell and C. Iadecola, "The neural basis of functional brain imaging signals," *Trends in Neurosciences,* vol. 25, no. 12, pp. 621-625, 2002.

[15] B. R. Rosen, J. W. Belliveau, B. R. Buchbinder, R. C. McKinstry, L. M. Porkka, D. N. Kennedy, M. S. Neuder, C. R. Fisel, H. J. Aronen, K. K. Kwong, R. M. Weisskoff, M. S. Cohen and T. J. Brady, "Contrast Agents and Cerebral Hemodynamics," *Magnetic Resonance in Medicine,* vol. 19, pp. 285-292, 1991.

[16] B. R. Rosen, J. W. Belliveau, H. J. Aronen, D. Kennedy, B. R. Buchbinder, A. Fischman,

M. Gruber, J. Glas, R. M. Weisskoff, M. S. Cohen, F. H. Hochberg and T. J. Brady, "Susceptibility Contrast Imaging of Cerebral Blood Volume: Human Experience," *Magnetic Resonance in Medicine,* vol. 22, pp. 293-299, 1991.

[17] J. W. Belliveau, D. N. Kennedy, R. C. McKinstry, B. R. Buchbinder, R. M. Weisskoff, M. S. Cohen, J. M. Vevea, T. J. Brady and B. R. Rosen, "Functional Mapping of the Human Visual Cortex by Magnetic Resonance Imaging," *Science,* vol. 254, pp. 716-719, 1991.

[18] C. Leithner and G. Royl, "The oxygen paradox of neurovascular coupling," *Journal of Cerebral Blood Flow & Metabolsim,* vol. 34, pp. 19-29, 2014.

[19] R. B. Buxton and L. R. Frank, "A model for the coupling between cerebral blood flow and oxygen metabolism during neural stimulation," *Journal of Cerebral Blood Flow & Metabolism,* vol. 17, pp. 64-72, 1997.

[20] K. A. Kasischke, E. M. Lambert, B. Panepento, A. Sun, H. A. Gelbard, R. W. Burgess, T. H. Foster and M. Nedergaard, "Two-photon NADH imaging exposes boundaries of oxygen diffusion in cortical vascular supply regions," *Journal of Cerebral Blood Flow & Metabolism,* vol. 31, pp. 68-81, 2011.

[21] A. Devor, S. Sakadzic, P. A. Saisan, M. A. Yaseen, E. Roussakis, V. J. Srinivasan, S. A. Vinogradov, B. R. Rosen, R. B. Buxton, A. M. Dale and D. A. Boas, ""Overshoot" of O2 is required to maintain baseline tissue oxygenation at locations distal to blood vessels," *Journal of Neuroscience,* vol. 31, no. 38, pp. 13676-13681, 2011.

[22] I. A. Silver and M. Erecinska, "Edtracellular Glucose Concentration in Mammal Brain: Continuous Monitoring of Changes during Increased Neuronal Activity and upon Limitation in Oxygen Supply in Normo-, Hypo-, and Hyperglycemic Animals," *Journal of Neuroscience,* vol. 14, no. 6, pp. 5068-5076, 1994.

[23] P. H. Poulsen, D. F. Smith, L. Ostergaard, E. H. Danielsen, A. Gee and S. B. Hansen, "In vivo estimation of cerebral blood flow, oxygen consumption and glucose metabolism in the pig by [15O]water injection, [15O]oxygen inhalation and dual injections of [18F]fluorodeoxyglucose," *Journal of Neuroscience Methods,* vol. 77, pp. 199-209, 1997.

[24] N. Hayashi, B. A. Green, M. Gonzalez-Carvajal, J. Mora and R. P. Veraa, "Local blood flow, oxygen tension, and oxygen consumption in the rat spinal cord," *Journal of Neurosurgery,* vol. 58, pp. 516-525, 1983.

[25] H. Ito, I. Kanno and H. Fukuda, "Human cerebral circulation: positron emission tomography studies," *Annals of Nuclear Medicine,* vol. 19, no. 2, pp. 65-74, 2005.

[26] B. T. Hawkins and T. P. Davis, "The Blood-Brain Barrier/Neurovascular Unit in Health and Disease," *The American Society for Pharmacology and Experimental Therapeutics,* vol. 57, pp. 173-185, 2005.

[27] M. Krueger and I. Bechmann, "CNS Pericytes: Concepts, Misconceptions, and a Way Out," *Glia,* vol. 58, pp. 1-10, 2010.

[28] H. Girouard and C. Iadecola, "Neurovascular coupling in the normal brain and in hypertension, stroke, and Alzheimer disease," *Journal of Applied Physiology,* vol. 100, no. 1, pp. 328-335, 2006.

[29] E. Ben-Menachem, B. B. Johansson and T. H. Svensson, "Increased vulnerability of the blood-brain barrier to acute hypertension following depletion of brain noradrenaline," *Journal of Neural Transmission,* vol. 53, pp. 159-167, 1982.

[30] Z. Cohen, G. Molinatti and E. Hamel, "Astroglial and vascular interactions of noradrenaline terminals in the rat cerebral cortex," *Journal of Cerebral Blood Flow,* vol. 17, pp. 894-904, 1997.

[31] P. M. Vanhoutte, "Serotonin and the vascular wall," *International Journal of Cardiology,* vol. 14, no. 2, pp. 189-203, 1987.

[32] Z. Cohen, G. Bonvento, P. Lacombe and E. Hamel, "Serotonin in the regulation of brain microcirculation," *Progress in Neurobiology,* vol. 50, pp. 335-362, 1996.

[33] E. Vaucher and E. Hamel, "Cholinergic basal forebrain neurons project to cortical microvessels in the rat: electron microscopic study with anterogradely transported Phaseolus vulgaris leucoagglutinin and choline acetyltransferase immunocytochemistry," *Journal of Neuroscience,* vol. 15, pp. 7427-7441, 1995.

[34] X. K. Tong and E. Hamel, "Regional cholinergic denervation of cortical microvessels and nitric oxide synthase-containing neurons in Alzheimer's disease," *Neuroscience,* vol. 92, pp. 163-175, 1999.

[35] B. Cauli, X.-K. Tong, A. Rancillac, N. Serluca, B. Lambolez, J. Rossier and E. Hamel, "Cortical GABA Interneurons in Neurovascular Coupling: Relays for Subcortical Vasoactive Pathways," *The Journal of Neuroscience,* vol. 24, no. 41, pp. 8940-8949, 2004.

[36] E. Vaucher, X. Tong, N. Cholet, S. Lantin and E. Hamel, "GABA neurons provide a rich input to microvessels but not nitric oxide neurons in the rat cerebral cortex: a means for direct regulation of local cerebral blood flow," *Journal of Comparative Neurology,* vol. 421, pp. 161-171, 2000.

[37] J. Neuhaus, W. Risau and H. Wolburg, "Induction of Blood-Brain Barrier Characteristics in Bovine Brain Endothelial Cells by Rat Astroglial Cells in Transfilter Coculture," *Annals New York Academy of Sciences,* vol. 633, pp. 578-580, 1991.

[38] J. M. Krum, K. L. Kenyon and J. M. Rosenstein, "Expression of blood-brain barrier characteristics following neuronal loss and astroglial damage after administraction of anti-Thy-1 immunotoxin," *Experimental Neurology,* vol. 146, no. 1, pp. 33-45, 1997.

[39] J. A. Holash, D. M. Noden and P. A. Stewart, "Re-evaluating the role of astrocytes in blood-brain barrier induction," *Developmental Dynamics,* vol. 197, no. 1, pp. 14-25, 1993.

[40] M. W. Brightman and T. S. Reese, "Junctions between intimately apposed cell membranes in the vertebrate brain," *The Journal of Cell Biology,* vol. 40, pp. 648-677, 1969.

[41] M. Zonta, M. C. Angulo, S. Gobbo, B. Rosengarten, K.-A. Hossmann, T. Pozzan and G. Carmignoto, "Neuron-to-astrocyte signalling is central to the dynamic control of brain microcirculation," *Nature Neuroscience,* vol. 6, no. 1, pp. 43-50, 2003.

[42] R. Bandopadhyay, C. Orte, J. G. Lawrenson, A. R. Reid, S. De Silva and G. Allt, "Contractile proteins in pericytes at the blood-brain and blood-retinal barriers.," *Journal of Neurocytology,* vol. 30, no. 1, pp. 35-44, 2001.

[43] D. M. Wu, H. Kawamura, K. Sakagami, M. Kobayashi and D. G. Puro, "Cholinergic regulation of pericyte-containing retinal microvessels," *American Journal of Physiology. Heart and Circulatory Physiology.,* vol. 284, no. 6, pp. H2083-H2090, 2003.

[44] C. N. Hall, C. Reynell, B. Gesslein, N. B. Hamilton, A. Mishra, B. A. Sutherland, F. M. O'Farrell, A. M. Buchan, M. Lauritzen and D. Attwell, "Capillary pericytes regulate

cerebral blood flow in health and disease," *Nautre,* vol. 508, pp. 55-60, 2014.

[45] P. Ballabh, A. Braun and M. Nedergaard, "The blood-brain barrier: an overview; Structure, regulation, and clinical implications," *Neurobiology of Disease,* vol. 16, pp. 1-13, 2003.

[46] J. Laterra, R. Keep, L. A. Betz and G. W. Goldstein, "Blood-Brain Barrier," in *Basic Neurochemistry: Molecular, Cellular and Medical Aspects*, Philadelphia, Lippincott-Raven, 1999.

[47] B. R. Duling, R. D. Hogan, B. L. Langille, S. S. Segal, S. F. Vatner, H. Weigelt and M. A. Young, "Vasomotor control: functional hyperemia and beyond.," *Federation Proceedings,* vol. 46, no. 2, pp. 251-263, 1987.

[48] H. H. Dietrich, Y. Kajita and R. G. Dacey Jr., "Local and conducted vasomotor responses in isolated rat cerebral arterioles," *American Physiology Society,* vol. 96, pp. H1109-H1116, 1996.

[49] R. L. DeValois and B. K. K. DeValois, Spatial Vision, Oxford: Oxford University Press, 1988.

[50] S. R. Olsen, D. S. Bortone, H. Adesnik and M. Scanziani, "Gain control by layer six in cortical circuits of vision," *Nature,* vol. 483, pp. 47-54, 2012.

[51] L. Pauling and C. D. Coryell, "The Magnetic Properties and Structure of Hemoglobin, Oxyhemoglobin and Carbonmonoxyhemoglobin," *Proceedings of the Natural Academy of Sciences,* vol. 22, no. 4, pp. 210-216, 1936.

[52] S. Ogawa, T.-M. Lee, A. S. Nayak and P. Glynn, "Oxygenation-Sensitive Contrast in Magnetic Resonance Image of Rodent Brain at High Magnetic Fields," *Magnetic Resonance in Medicine,* vol. 14, pp. 68-78, 1990.

[53] K. K. Kwong, J. W. Belliveau, D. A. Chesler, I. E. Goldbero, R. M. Weisskoff, B. P. Poncelet, D. N. Kennedy, B. E. Hoppel, M. S. Cohen, R. Turner, H.-M. Cheng, T. J. Brady and B. R. Rosen, "Dynamic magnetic resonance imaging of human brain activity during primary sensory stimulation," *Proceedings of the National Academy of Sciences,* vol. 89, pp. 5675-5679, 1992.

[54] S. Ogawa, D. W. Tank, R. Menon, J. M. Ellermann, S.-G. Kim, H. Merkle and K. Ugurbil, "Intrinsic signal changes accompanying sensory stimulation: Functional brain mapping with magnetic resonance imaging," *Proceedings of the National Academy of Sciences,* vol. 89, pp. 5951-5955, 1992.

[55] P. A. Bandettini, E. C. Wong, R. S. Hinks, R. S. Tikofsky and J. S. Hyde, "Time Course EPI of Human Brain Function during Task Activation," *Magnetic Resonance in Medicine,* vol. 25, pp. 390-397, 1992.

[56] N. K. Logothetis, J. Pauls, M. Augath, T. Trinath and A. Oeltermann, "Neurophysiological investigation of the basis of the fMRI signal," *Nature,* vol. 412, pp. 150-157, 2001.

[57] A. D. Legatt, J. Arezzo and H. G. Vaughan Jr., "Averaged multiple unit activity as an estimate of phasic changes in local neuronal activity: effects of volume-conducted potentials," *Journal of Neuroscience Methods,* vol. 2, no. 2, pp. 203-217, 1980.

[58] W. J. Freeman, Mass Action in the Nervous System, New York: Academic Press, Inc, 1975.

[59] U. Mitzdorf, "Properties of the evoked potential generators: current source-density

analysis of visually evoked potentials in the cat cortex," *International Journal of Neuroscience,* vol. 33, no. 1-2, pp. 33-59, 1987.

[60] E. Juergens, A. Guettler and R. Eckhorn, "Visual stimulation elicits locked and induced gamma oscillations in monkey intracortical- and EEG-potentials, but not in human EEG," *Experimental Brain Research,* vol. 129, no. 2, pp. 247-259, 1999.

[61] S. G. Kim, K. Hendrich, X. Hu, H. Merkle and K. Ugurbil, "Potential pitfalls of functional MRI using conventional gradient-recalled echo techniques," *NMR in Biomedicine,* vol. 7, no. 1-2, pp. 69-74, 1994.

[62] R. Turner, "How Much Cortex Can a Vein Drain? Downstream Dilution of Activation-Related Cerebral Blood Oxygenation Changes," *NeuroImage,* vol. 16, pp. 1062-1067, 2002.

[63] T. Q. Duong, E. Yacoub, G. Adriany, X. Hu, K. Ugurbil and S.-G. Kim, "Microvascular BOLD Contribution at 4 and 7T in the Human Brain: Gradient-Echo and Spin-Echo fMRI With Supression of Blood Effects," *Magnetic Resonance in Medicine,* vol. 49, pp. 1019-1027, 2003.

[64] K. R. Thulborn, J. C. Waterton, P. M. Matthews and G. K. Radda, "Oxygenation dependence of the transverse relaxation time of water protons in whole blood at high field.," *Biochimica et Biophysica Acta.,* vol. 714, no. 2, pp. 265-270, 1982.

[65] G. L. Shulman, J. A. Fiez, M. Corbetta, R. L. Buckner, F. M. Miezin, M. E. Raichle and S. E. Petersen, "Common Blood Flow Changes across Visual Tasks: II. Decreases in Cerebral Cortex," *Journal of Cognitive Neuroscience,* vol. 9, no. 5, pp. 648-663, 1997.

[66] T. Paus, S. Marrett, K. J. Worsley and A. C. Evans, "Extraretinal Modulation of Cerebral Blood Flow in the Human Cortex: Implications for Saccadic Suppression," *Journal of Neurophysiology,* vol. 71, no. 5, pp. 2179-2183, 1995.

[67] R. B. H. Tootell, N. Hadjikhani, E. K. Hall, S. Marrett, W. Vanduffel, J. T. Vaughan and A. M. Dale, "The Retionotopy of Visual Spatial Attention," *Neuron,* vol. 21, pp. 1409-1422, 1998.

[68] J. D. Allison, K. J. Meador, D. W. Loring, R. E. Figueroa and J. C. Wright, "Functional MRI cerebral activation and deactivation during finger movement," *American Academy of Neurology,* vol. 54, pp. 135-142, 2000.

[69] A. Shmuel, E. Yacoub, J. Pfeuffer, P.-F. Van de Moortele, G. Adriany, X. Hu and K. Ugurbil, "Sustained Negative BOLD, Blood Flow and Oxygen Consumption Response and Its Coupling to the Positive Response in the Human Brain," *Neuron,* vol. 36, pp. 1195-1210, 2002.

[70] N. Harel, S.-P. Lee, T. Nagaoka, D.-S. Kim and S.-G. Kim, "Origin of Negative Blood Oxygenation Level-Dependent fMRI Signals," *Journal of Cerebral Blood Flow & Metabolism,* vol. 22, pp. 908-917, 2002.

[71] S. S. Kannurpatti and B. B. Biswal, "Negative Functional Response to Sensory Stimulation and Its Origins," *Journal of Cerebral Blood Flow & Metabolism,* vol. 24, pp. 703-712, 2004.

[72] A. Devor, I. Ulbert, A. K. Dunn, S. N. Narayanan, S. R. Jones, M. L. Andermann, D. A. Boas and A. M. Dale, "Coupling of the cortical hemodynamic response to cortical and thalamic neuronal activity," *Proceedings of the National Academy of Sciences,* vol. 24, pp.

703-712, 2004.

[73] L. Gold and M. Lauritzen, "Neuronal deactivation explains decreased cerebellar blood flow in response to focal cerebral ischemia or suppressed neocortical function," *Proceedings of the National Academy of Sciences,* vol. 99, no. 11, pp. 7699-7704, 2002.

[74] B. Stefanovic, J. M. Warnking and G. B. Pike, "Hemodynamic and metabolic responses to neuronal inhibition," *NeuroImage,* vol. 22, pp. 771-778, 2004.

[75] A. Shmuel, M. Augath, A. Oeltermann and N. K. Logothetis, "Negative functional MRI response correlates with decreases in neuronal activity in monkey visual area V1," *Nature Neuroscience,* vol. 9, no. 4, pp. 569-577, 2006.

[76] K. J. Mullinger, S. D. Mayhew, A. P. Bagshaw, R. Bowtell and S. T. Francis, "Evidence that the negative BOLD response is neuronal in origin: A simultaneous EEG-BOLD-CBF study in humans," *NeuroImage,* vol. 94, pp. 263-274, 2014.

[77] The MathWorks, Inc., MATLAB 2015a, Natick, Massachusetts, 2015.

[78] D. H. Brainard, "The Psychophysics Toolbox," *Spatial Vision,* vol. 10, pp. 433-436, 1997.

[79] D. G. Pelli, "The VideoToolbox software for visual psychophysics: Transforming numbers into movies.," *Spatial Vision,* vol. 10, pp. 437-442, 1997.

[80] M. Kleiner, D. Brainard and D. Pelli, "What's new in Psychtoolbox-3?," in *European Conference on Visual Perception Abstract Supplement*, 2007.

[81] F. W. Cornelissen, E. Peters and J. Palmer, "The Eyelink toolbox: Eye tracking with MATLAB and the Psychophysics Toolbox.," *Behavior Research Methods, Instruments & Computers,* vol. 34, pp. 613-617, 2002.

[82] Windmiller Kolster Scientific, "Windmiller Kolster Scientific," Windmiller Kolster Scientific, [Online]. Available: http://www.wkscientific.com/. [Accessed 05 08 2015].

[83] Rogue Research Inc., "Rogue Research," [Online]. Available: https://www.rogue-research.com/. [Accessed 05 08 2015].

[84] Hybex Innovations, "Hybex Innovations," [Online]. Available: http://www.hybex.com/en/. [Accessed 05 08 2015].

[85] H. Lu, J. Hua and P. C. M. van Zijl, "Noninvasive functional imaging of cerebral blood volume with vascular-space-occupancy (VASO) MRI," *NMR in Biomedicine,* vol. 26, pp. 932-948, 2013.

[86] L. Huber, J. Goense, A. J. Kennerley, R. Trampel, M. Guidi, E. Reimer, D. Ivanov, N. Neef, C. J. Gauthier, R. Turner and H. E. Moeller, "Cortical lamina-dependent blood volume changes in human brain at 7 T," *Neuroimage,* vol. 107, pp. 23-33, 2014.

[87] D. Qiu, G. Zaharchuk, T. Christen, W. W. Ni and M. E. Moseley, "Contrast-enhanced functional blood volume imaging (CE-fBI): Enhanced sensitivity for brain activation in humans using the ultrasmall superparamagnetic iron oxide agent ferumoxytol," *NeuroImage,* vol. 62, pp. 1726-1731, 2012.

[88] H. Canada, "Summary Basis of Decision (SBD) for FERAHEME," 26 06 2012. [Online]. Available: http://www.hc-sc.gc.ca/dhp-mps/prodpharma/sbd-smd/drug-med/sbd_smd_2012_feraheme_133250-eng.php. [Accessed 24 07 2015].

[89] J. B. Mandeville, J. J. A. Marota, B. E. Kosofsky, J. R. Keltner, R. Weissleder, B. R. Rosen and R. M. Weisskoff, "Dynamic Functional Imaging of Relative Cerebral Blood Volume During Rat Forepaw Stimulation," *Magnetic Resonance in Medicine,* vol. 39, no.

4, pp. 615-624, 1998.

[90] P. Kellman and E. R. McVeigh, "Image Reconstruction in SNR Units: A General Method for SNR Measurement," *Magnetic Resonance in Medicine,* vol. 54, no. 6, pp. 1439-1447, 2005.

[91] Morris Instruments, "RF Sweepers," 29 09 2011. [Online]. Available: http://morrisinstruments.com/sweeper.html. [Accessed 05 08 2015].

[92] M. Jenkinson, C. F. Beckmann, T. E. Behrens, M. W. Woolrich and S. M. Smith, "FSL," *NeuroImage,* vol. 62, pp. 782-790, 2012.

[93] M. W. Woolrich, S. Jbabdi, B. Patenaude, M. Chappell, S. Makni, T. Behrens, C. Beckmann, M. Jeninson and S. M. Smith, "Bayesian analysis of neuroimaging data in FSL.," *NeuroImage,* vol. 45, pp. S173-S186, 2009.

[94] S. M. Smith, M. Jenkinson, M. W. Woolrich, C. F. Beckmann, T. E. Behrens, H. Johansen-Berg, P. R. Bannister, M. De Luca, I. Drobnjak, D. E. Flitney, R. Niazy, J. Sauders, J. Vickers, Y. Zhang, N. De Stefano, J. M. Brady and P. M. Matthews, "Advances in functional and structural MR image analysis and implementation as FSL.," *NeuroImage,* vol. 23, no. S1, pp. 208-219, 2004.

[95] M. Jenkinson, P. Bannister, J. M. Brady and S. M. Smith, "Improved Optimisation for the Robust and Accurate Linear Registration and Motion Correction of Brain Images," *NeuroImage,* vol. 17, no. 2, pp. 825-841, 2002.

[96] D. Holland, J. M. Kuperman and A. M. Dale, "Efficient Correction of Inhomogeneous Static Magnetic Field-Induced Distortion in Echo Planar Imaging," *NeuroImage,* vol. 50, no. 1, pp. 175-183, 2010.

[97] B. A. Wandell and J. Winawer, "Imaging retinotopic maps in the human brain," *Vision Research,* vol. 51, no. 7, pp. 718-737, 2011.

[98] R. B. H. Tootell, N. Hadjikhani, E. K. Hall, S. Marrett, W. Vanduffel, J. T. Vaughan and A. M. Dale, "The Retinotopy of Visual Spatial Attention," *Neuron,* vol. 21, pp. 1409-1422, 1998.

[99] J. B. Mandeville, B. G. Jenkins, B. E. Kosofsky, M. A. Moskowitz, B. R. Rosen and J. J. A. Marota, "Regional Sensitivity and Coupling of BOLD and CBV Changes During Stimulation of Rat Brain," *Magnetic Resonance in Medicine,* vol. 45, pp. 443-447, 2001.

[100] L. Boorman, A. J. Kennerley, D. Johnston, M. Jones, Y. Zheng, P. Redgrave and J. Berwick, "Negative Blood Oxygen Level Dependence in the Rat: A Model for Investigating the Role of Suppression in Neurovascular Coupling," *The Journal of Neuroscience,* vol. 30, no. 12, pp. 4285-4294, 2010.

[101] R. P. Kennan, B. E. Scanley, R. B. Innis and J. C. Gore, "Physiological Basis for BOLD MR Signal Changes Due to Neuronal Stimulation: Separation of Blood Volume and Magnetic Susceptibility Effects," *Magnetic Resonance in Medicine,* vol. 40, pp. 840-848, 1998.

[102] S.-G. Kim and S. Ogawa, "Biophysical and physiological origins of blood oxygenation level-dependent fMRI signals," *Journal of Cerebral Blood Flow & Metabolism,* vol. 32, no. 7, pp. 1188-1206, 2012.

[103] F. Zhao, P. Wang, K. Hendrich and S.-G. Kim, "Spatial specificty of cerebral blood volume-weighted fMRI responses at columnar resolution," *NeuroImage,* vol. 27, pp. 416-

424, 2005.

[104] N. K. Logothetis, "The neural basis of the blood-oxygen-level-dependent functional magnetic resonance imaging signal," *Philosophical Transactions for the Royal Society of London,* vol. 357, pp. 1003-1037, 2002.

[105] C. Blakemore and E. A. Tobin, "Lateral Inhibition Between Orientation Detectors in the Cat's Visual Cortex," *Experimental Brain Research,* vol. 15, pp. 439-440, 1972.

[106] R. T. Born and R. B. H. Tootell, "Single-unit and 2-deoxyglucose studies of side inhibition in macaque striate cortex," *Proceedings of the National Academy of Sciences,* vol. 88, pp. 7066-7070, 1991.

[107] B. J. McCullough, O. Kolokythas, J. H. Maki and D. E. Green, "Ferumoxytol in clinical practice: implications for MRI," *Journal of Magnetic Resonance Imaging,* vol. 37, no. 6, pp. 1476-1479, 2013.

[108] P. A. Bandettini, E. C. Wong, R. S. Hunks, R. S. Tikofsky and J. S. Hyde, "Time Course EPI of Human Brain Function during Task Activation," *Magnetic Resonance in Medicine,* vol. 25, pp. 390-397, 1992.

[109] P. Meier and K. Zierler, "On the Theory of the Indicator-Dilution Method for Measurement of Blood Flow and Volume," *Journal of Applied Physiology,* vol. 6, no. 12, pp. 731-744, 1954.

[110] H. Kawamura, T. Sugiyama, D. M. Wu, M. Kobayashi, S. Yamanishi and K. Katsumura, "ATP: a vasoactive signal in the pericyte-containing microvasculature of the rat retina," *Journal of Physiology,* vol. 551, no. 3, pp. 787-799, 2003.

[111] D. M. Wu, H. Kawamura, K. Sakagami, M. Kobayashi and D. G. Puro, "Cholinergic regulation of pericyte-containing retinal microvessels," *American Journal of Physiology; Heart Circulation Physiology,* vol. 284, pp. H2083-H2090, 2003.

[112] Z. Cohen, G. Bonvento, P. Lacombe and E. Hamel, "Serotonin in the regulation of brain microcirculation," *Progress in Neurobiology,* vol. 50, pp. 335-362, 1996.

[113] K. K. Kwong, J. W. Belliveau, D. A. Chesler, I. E. Goldbero, R. M. Weisskoff, B. P. Poncelet, D. N. Kennedy, B. E. Hoppel, M. S. Cohen, R. Turner, H.-M. Cheng, T. J. Brady and B. R. Rosen, "Dynamic magnetic resonance imaging of human brain activity during primary sensory stimulation".

[114] X. Hu and E. Yacoub, "The Story of the Initial dip in fMRI," *NeuroImage,* vol. 62, no. 2, pp. 1103-1108, 2012.

[115] T. Q. Duong, D. S. Kim, K. Ugurbil and S. G. Kim, "Spatiotemporal dynamics of the BOLD fMRI signals: toward mapping submillimeter cortical columns using the early negative response.," *Magnetic Resonance in Medicine,* vol. 44, no. 2, pp. 231-242, 2000.

[116] F. Zhao, P. Wang, K. Hendrich, K. Ugurbil and S.-G. Kim, "Cortical layer-dependent BOLD and CBV responses measured by spin-echo and gradient-echo fMRI: Insights into hemodynamic regulation," *NeuroImage,* vol. 30, pp. 1149-1160, 2006.

[117] D. A. Yablonskiy and E. M. Haacke, "Theory of NMR signal behavior in magnetically inhomogeneous tissues: the static dephasing regime," *Magnetic Resonance in Medicine,* vol. 32, no. 6, pp. 749-763, 1994.

[118] M. A. Pinsk, T. Moore, M. C. Richter, C. G. Gross and S. Kastner, "Methods for functional magnetic resonance imaging in normal and lesioned behaving monkeys,"

Journal of Neuroscience Methods, vol. 143, pp. 179-195, 2005.

[119] A. L. Alexander, K. M. Hasan, M. Lazar, J. S. Tsuruda and D. L. Parker, "Analysis of Partial Volume Effects in Duffision-Tensor MRI," *Magnetic Resonance in Medicine,* vol. 45, pp. 770-780, 2001.

11 Appendix

11.1 Gaze Heat maps

This section contains the gaze heat maps for all experiments. They are all very similar, hence their exclusion from the main text. They are useful for demonstrating that the NHP's training was very effective, and that the stimulus affected the intended area of the visual field. Identically-titled plots are the results from the same experiments performed on separate days.

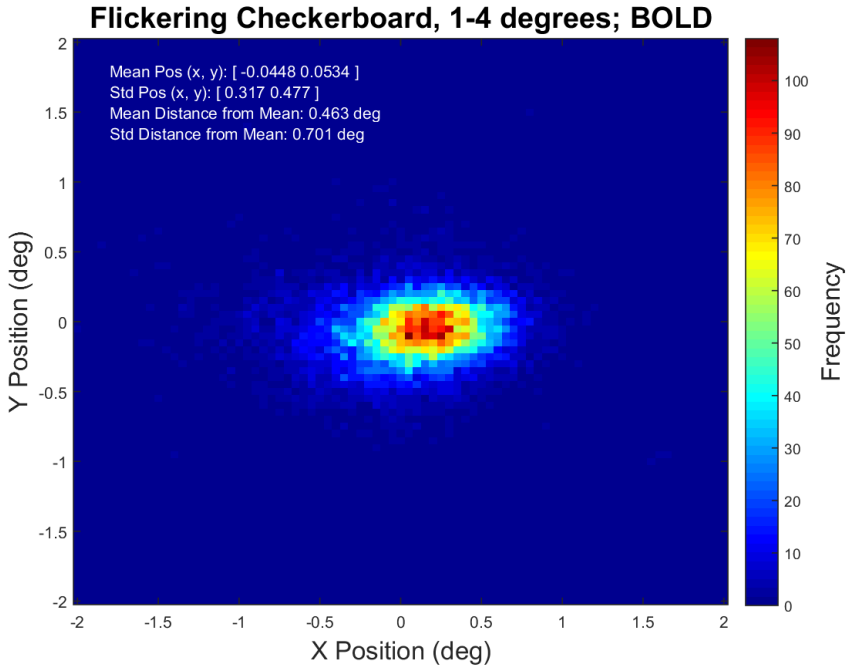

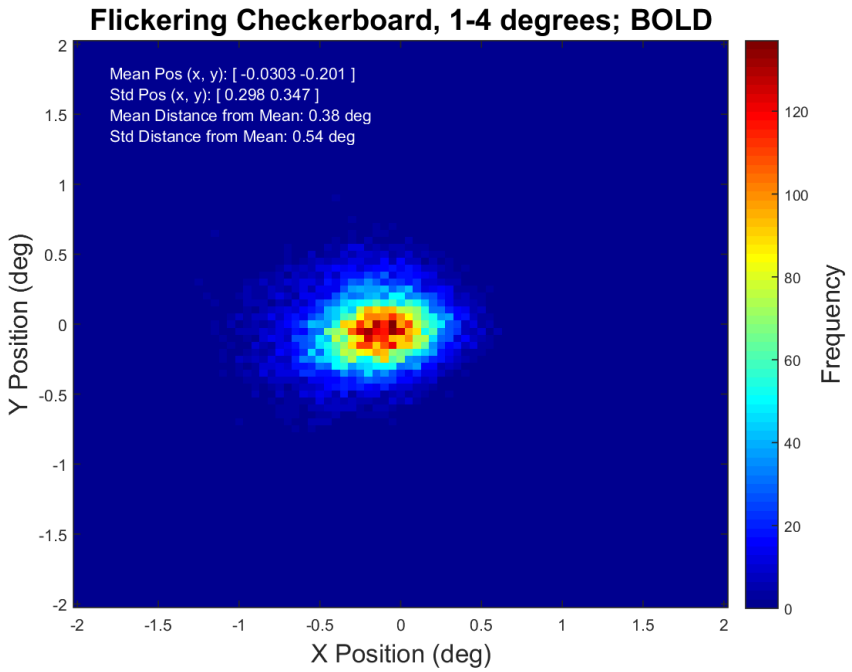
Flickering Checkerboard, 1-4 degrees; BOLD
Mean Pos (x, y): [-0.0303 -0.201]
Std Pos (x, y): [0.298 0.347]
Mean Distance from Mean: 0.38 deg
Std Distance from Mean: 0.54 deg
Y Position (deg)
X Position (deg)
Frequency

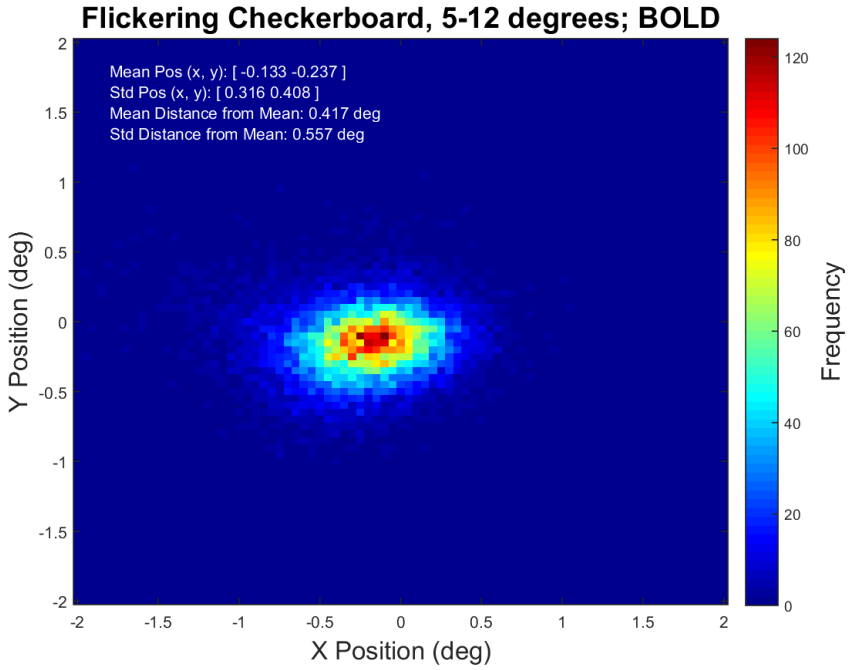
Flickering Checkerboard, 5-12 degrees; BOLD
Mean Pos (x, y): [-0.133 -0.237]
Std Pos (x, y): [0.316 0.408]
Mean Distance from Mean: 0.417 deg
Std Distance from Mean: 0.557 deg
Y Position (deg)
X Position (deg)
Frequency

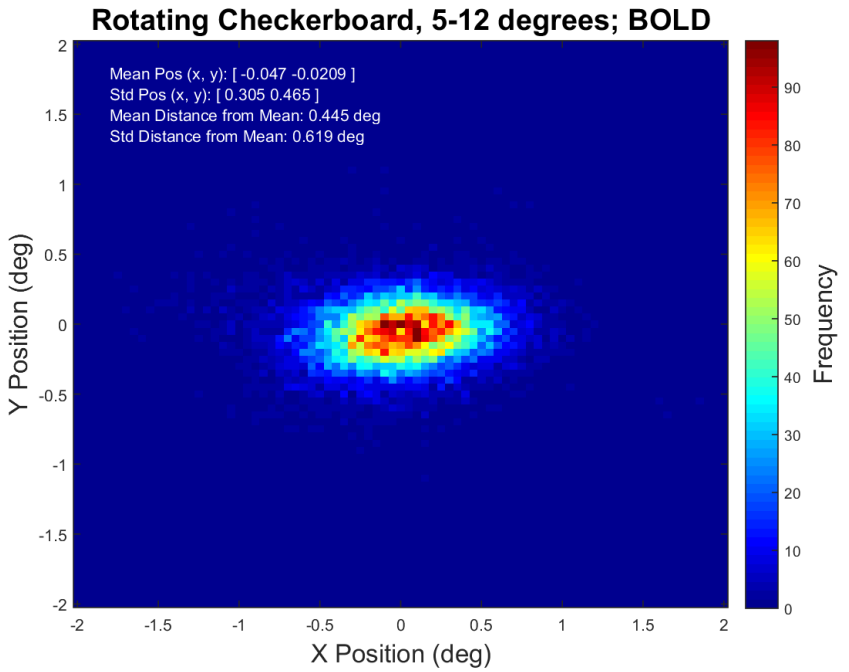
Rotating Checkerboard, 5-12 degrees; BOLD
Mean Pos (x, y): [-0.047 -0.0209]
Std Pos (x, y): [0.305 0.465]
Mean Distance from Mean: 0.445 deg
Std Distance from Mean: 0.619 deg
Y Position (deg)
X Position (deg)
Frequency

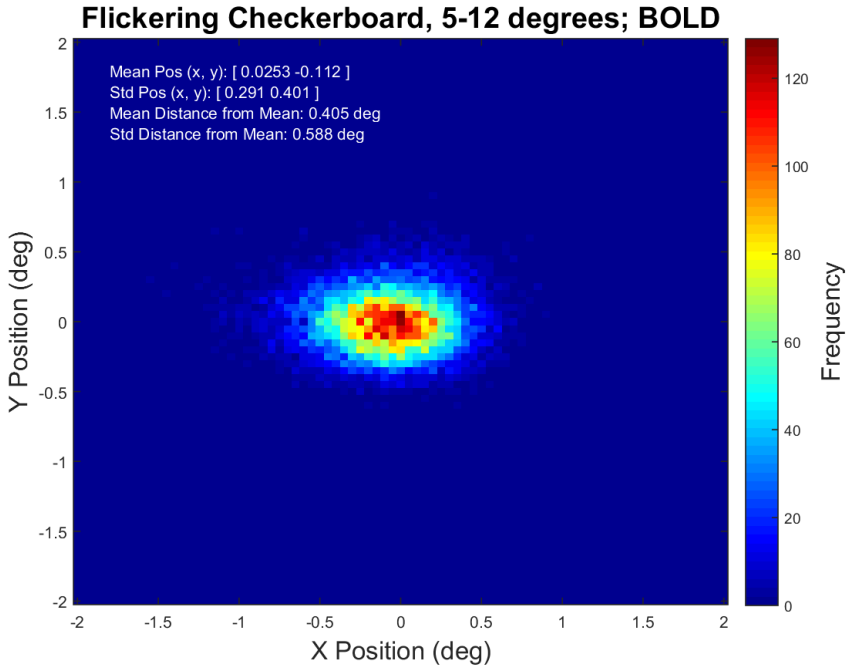
Flickering Checkerboard, 5-12 degrees; BOLD
Mean Pos (x, y): [0.0253 -0.112]
Std Pos (x, y): [0.291 0.401]
Mean Distance from Mean: 0.405 deg
Std Distance from Mean: 0.588 deg
Y Position (deg)
X Position (deg)
Frequency

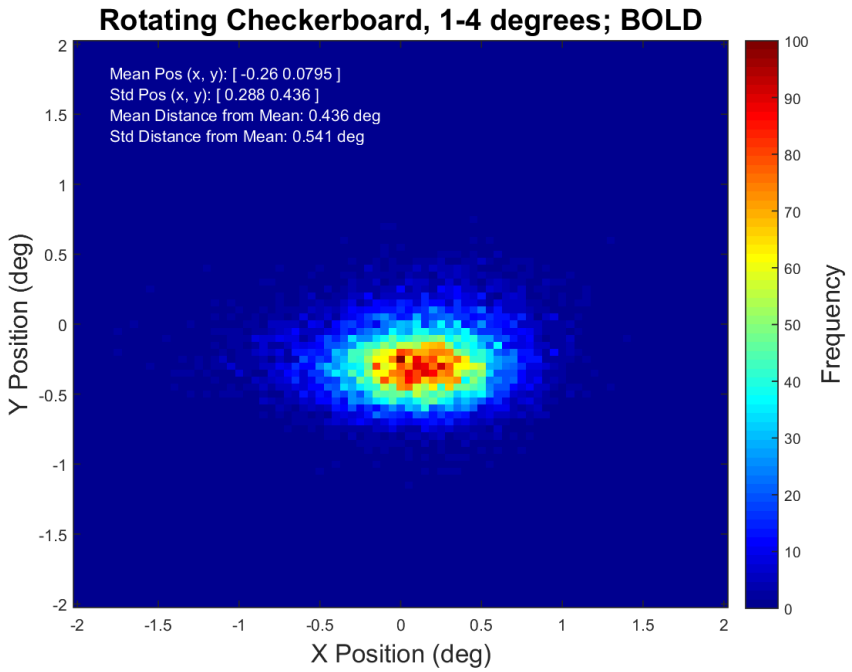
Rotating Checkerboard, 1-4 degrees; BOLD
Mean Pos (x, y): [-0.26 0.0795]
Std Pos (x, y): [0.288 0.436]
Mean Distance from Mean: 0.436 deg
Std Distance from Mean: 0.541 deg
Y Position (deg)
X Position (deg)
Frequency

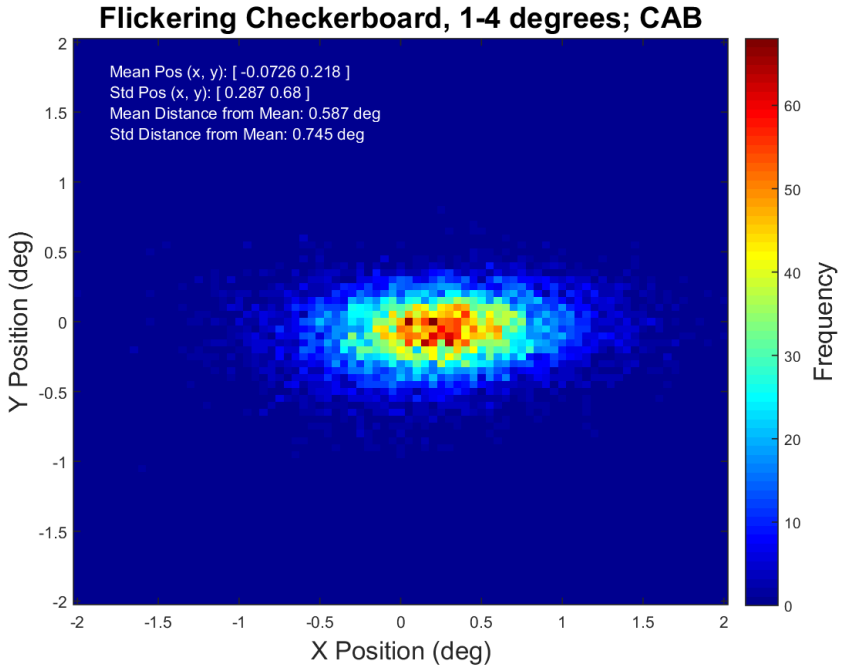
Flickering Checkerboard, 1-4 degrees; CAB
Mean Pos (x, y): [-0.0726 0.218]
Std Pos (x, y): [0.287 0.68]
Mean Distance from Mean: 0.587 deg
Std Distance from Mean: 0.745 deg
Y Position (deg)
X Position (deg)
Frequency

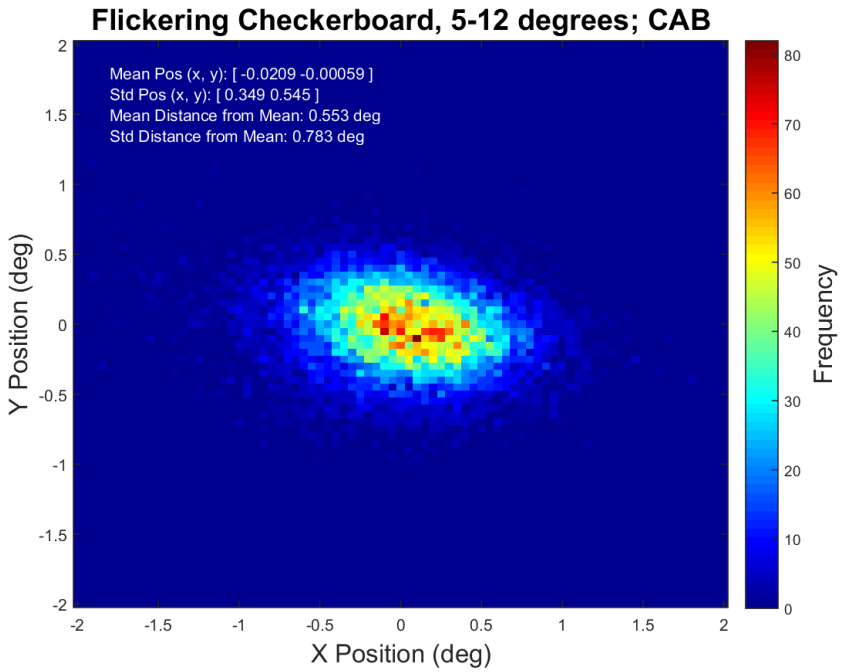
Flickering Checkerboard, 5-12 degrees; CAB
Mean Pos (x, y): [-0.0209 -0.00059]
Std Pos (x, y): [0.349 0.545]
Mean Distance from Mean: 0.553 deg
Std Distance from Mean: 0.783 deg
Y Position (deg)
X Position (deg)
Frequency

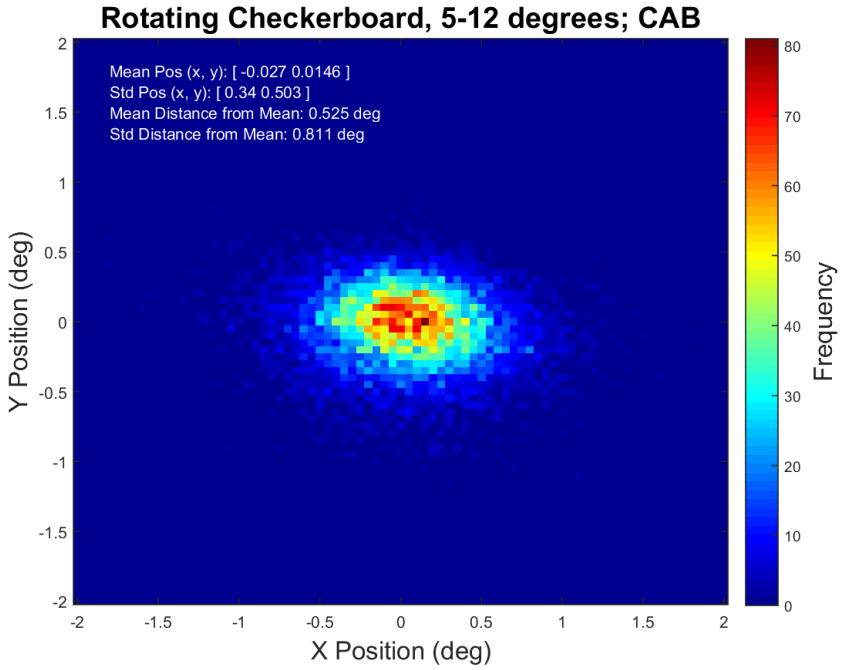
Rotating Checkerboard, 5-12 degrees; CAB
Mean Pos (x, y): [-0.027 0.0146]
Std Pos (x, y): [0.34 0.503]
Mean Distance from Mean: 0.525 deg
Std Distance from Mean: 0.811 deg
Y Position (deg)
X Position (deg)
Frequency

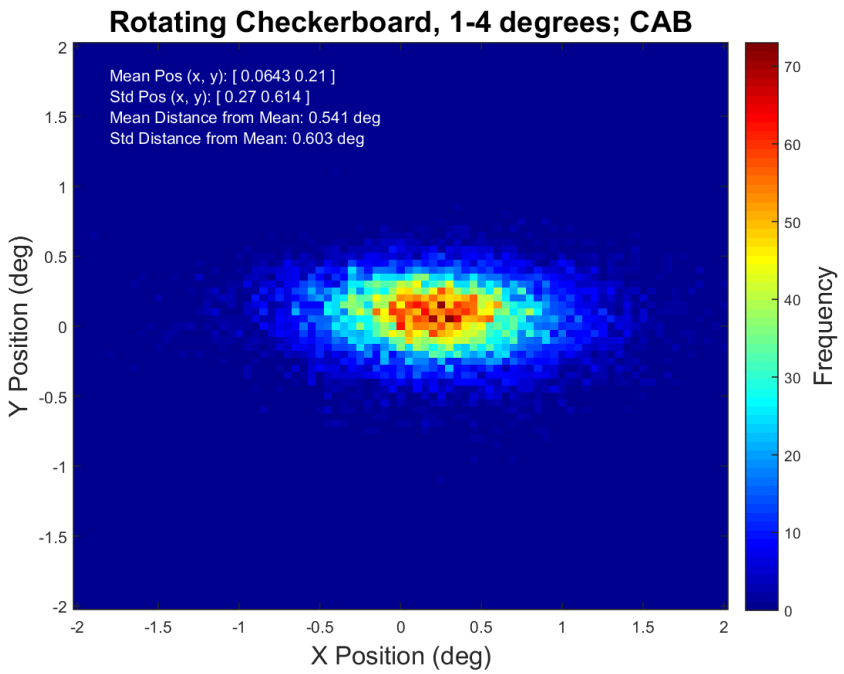
Rotating Checkerboard, 1-4 degrees; CAB
Mean Pos (x, y): [0.0643 0.21]
Std Pos (x, y): [0.27 0.614]
Mean Distance from Mean: 0.541 deg
Std Distance from Mean: 0.603 deg
Y Position (deg)
X Position (deg)
Frequency
2
1.5
1
0.5
0
-0.5
-1
-1.5
-2
70
60
50
40
30
20
10
0